DYNAMICS OF INTERPLANETARY DUST
IN THE F CORONA

By

EDWIN T. RUSK

A DISSERTATION PRESENTED TO THE GRADUATE SCHOOL OF
THE UNIVERSITY OF FLORIDA
IN PARTIAL FULFILLMENT OF THE REQUIREMENTS FOR THE
DEGREE OF DOCTOR OF PHILOSOPHY

UNIVERSITY OF FLORIDA

1986

Copyright 1986

by

Edwin T. Rusk

ACKNOWLEDGEMENTS

First and foremost I would like to thank my advisor, Dr. N.Y. Misconi, for having confidence in me and encouraging me to undertake this project. If not for his support and encouragement I would never have been able to continue in the field. His valuable advice extended far beyond the bounds of astronomy.

I would also like to thank Dr. H.K. Eichhorn who bravely professed confidence in me. He stood up for me and gained me the time necessary to complete this work. Thanks go also to Dean M.M. Lockhart for extending my deadline.

Dr. B.Å.S. Gustafson contributed many helpful suggestions in the preparation of this dissertation and much assistance in proofreading.

Dr. J.T. Hoeksema generously provided me with a model of the solar magnetic field and associated data upon which I based my numerical simulations.

I thank Mrs. Adele Koehler for her assistance in preparing my dissertation.

Last, but not least, I wish to thank my wife Nancy for her understanding and support at this stressful time.

TABLE OF CONTENTS

Page

ACKNOWLEDGEMENTS.. iii

ABSTRACT.. v

CHAPTER

I INTRODUCTION.. 1

II PLANETARY PERTURBATIONS AND THE STRUCTURE OF THE ZODIACAL CLOUD.. 7

A. Introduction.. 7
B. Method.. 8
C. Results... 14
D. Conclusion.. 28

III INITIAL PARTICLE DISTRIBUTION OF THE F CORONA.................. 32

IV PLANETARY INFLUENCE IN THE F CORONA............................. 39

V THE EFFECT OF THE SOLAR MAGNETIC FIELD............................ 52

A. An Overview... 52
B. The Dipole Component.. 55
C. The Quadrupole Terms.. 60
D. Octupole Terms.. 65
E. Numerical Simulations... 70
F. Analysis of Observational Evidence............................ 103

VI THE EFFECT OF THE SUN'S FINITE SIZE AND SOLAR ROTATION.... 108

VII CONCLUSION... 121

VIII SUGGESTIONS FOR FUTURE RESEARCH................................ 124

REFERENCES.. 126

APPENDIX

A MATHEMATICAL RELATIONS.. 130

B GRAPHIC DATA OF PARTICLE SIMULATIONS.............................. 134

BIOGRAPHICAL SKETCH... 329

Abstract of Dissertation Presented to the Graduate School of
the University of Florida in Partial Fulfillment of the Requirements
for the Degree of Doctor of Philosophy

DYNAMICS OF INTERPLANETARY DUST IN THE F CORONA

by

Edwin T. Rusk

May 1986

Chairman: Nebil Y. Misconi
Major Department: Astronomy

We studied the dynamical mechanisms in interplanetary space and in the F corona by numerical simulations. An expression for the radiation pressure force due to a rotating spherical source of radiation was derived. Also, expressions relating the variation in inclination and the longitude of the ascending node to the solar magnetic field were derived. These expressions are based on the spherical source surface model of the solar magnetic field.

Simulations of particles released during perihelion passages of comet Encke show that cometary particles have lifetimes *SHORTER* than the lifetime calculated by Wyatt and Whipple in 1950. These simulations also resulted in higher eccentricities and a definite alignment of the particles' aphelia toward a direction 20° east of the vernal equinox.

An expression relating the size of a planet's zone of influence to perturbations on particles in solar orbits based on the closest approach between the planet and the particle show that the expression for the size of a planet's zone of influence is not singular, but varies with the particular orbital element which is being studied.

Simulations of the interaction of the Lorentz force with dust in the F corona, based on observed solar magnetic field values, result in a *SPREADING OF THE INCLINATIONS* of particles in circumsolar orbits. This result, along with a reevaluation of recent observations of the F corona, leads us to the conclusion that the shape of the circumsolar dust cloud can not be a ring, but must be a wide band or a spherical shell.

CHAPTER I

INTRODUCTION

On a clear dark night just after astronomical twilight, one can observe a section of the sky in the west which appears brighter than the surrounding regions. This light comes from sunlight reflected by a myriad of small particles, less than .1 mm across, each following its own orbital path about the sun. Because the greatest concentration of these particles orbit in or near the plane of the earth's orbit, and thus among the constellations of the zodiac, this phenomenon is called the zodiacal light and the interplanetary particles as a group are called the zodiacal dust cloud.

The F corona is the innermost region of the zodiacal cloud, culminating in a "dust free" zone surrounding the sun. The light scattered by dust particles near the sun forms the F corona and is part of the zodiacal light. This region can be distinguished from the inner K corona by the spectra of the light emitted by these two regions, since the F corona displays the Fraunhofer spectrum of the sun while the spectrum of the K corona is characterized by the emission lines typical of a very high temperature plasma. The F corona is the final resting place of the dust grains which spiral slowly inward through the interplanetary medium due to the radiation induced Poynting-Robertson drag (henceforth P-R drag; Poynting, 1903;

Robertson, 1937). Upon reaching the F corona, the particles begin to sublimate, and the sublimation rate increases until, finally, much smaller remnants of the original dust particles, called beta-meteoroids, are blown out of the solar system by radiation pressure. Because the conditions in the F corona control the final fate of interplanetary dust, it becomes an important factor in determining the dust budget, the rate at which zodiacal dust is created and destroyed. Unfortunately, at the present time, little is known about the nature, size, composition, or dynamics of the dust particles in this region.

At this time, the source(s) of the interplanetary dust are not known. Several theories have been put forth; the most popular theories claim that the dust is released by either long or short period comets or from asteroid and/or meteoroid collisions (Grün et al., 1985). Whichever theory is true, it is fairly well established that the dust in the F corona originated farther out in the solar system (cf. Mukai, 1983) and reached the near solar regions due to the slow decrease in semimajor axis caused by the P-R drag.

Scattering measurements (Greenberg and Gustafson, 1981) indicate that those zodiacal dust particles which are the major source of the zodiacal light are "fluffy" silicates, irregular in shape with a density of less than 1 gm/cm^3 due to their porous nature. Silicates, and particularly SiO_2, are likely candidates for F coronal particles since they have high vaporization temperatures and thus can survive in the coronal regions. Others have used graphite in their models of F coronal dynamics because it also has a high vaporization temperature, although there is no evidence that graphite grains comprise a significant percentage of zodiacal particles.

There are many mechanisms which influence the motion of interplanetary grains as they orbit the sun. Solar radiation acts in two ways upon orbiting dust particles. First, because the sun's radiation field is radial and drops off as the inverse square of the distance from the sun, the force generated from the direct pressure of solar radiation forms a constant ratio to the solar gravitational force, and thus the combination of gravity and radiation pressure from the sun acts upon small particles exactly as if the sun were a non-radiating body of lesser mass. Secondly, the motion of each particle creates a second order (in v/c) force from the solar radiation due to both the Doppler shift of the radiation and an aberration effect. These two second order effects combine to form the P-R drag. This drag force opposes the motion of the dust particle, reducing the particle's orbital velocity and hence the kinetic energy of its orbit. Since the total energy of an orbiting body is directly related to its semimajor axis, one effect of P-R drag is to slowly decrease the semimajor axis of orbiting dust grains.

Gravitational effects of the planets cause significant perturbations upon dust particle orbits. Becuase the P-R drag continually reduces the semimajor axis, an orbiting particle will have its orbital path crossing those of each of the inner planets at some point during its lifetime. This increases the likelihood of one or more close planetary encounters. The nature of the effects of gravitational interactions with the planets is therefore different for dust particles as opposed to large bodies such as meteoroids or asteroids, which, if they are in orbits which to not intersect those of the planets, will not have these "catastrophic" planetary encounters.

The interplanetary magnetic field is an extension of the solar magnetic field into the planetary environment carried by the solar wind. It will alter the orbital path of small charged dust particles by the Lorentz force. The interplanetary magnetic field can be considered to be a combination of two components, a radial component directed inward to or outward from the sun and a tangential component perpendicular to both the radial direction and the direction of the solar rotation axis.

In the region of the F corona, the radial component of the interplanetary magnetic field is much stronger than the tangential component. Here, the magnetic field becomes an important factor in perturbing the particle's orbit because the usually stronger P-R drag is balanced by a loss of particle size due to sublimation which results from the high temperatures of this region. This balance allows the weaker Lorentz force to play a more significant role. Outside the F corona, the Lorentz force becomes negligible compared to P-R drag. Because the radial component of the magnetic field drops off as the square of the distance from the sun, as does P-R drag, the Lorentz force due to the radial component of the interplanetary field can be neglected everywhere except in the F corona. The tangential component of the interplanetary magnetic field only decreases as the heliocentric distance to the 1st power, so at large distances from the sun, the Lorentz force due to this tangential component is of the same order as the P-R drag for micron-sized particles. This is of significant importance in determining the influx of interstellar dust into the solar system (Gustafson and Misconi, 1979).

In the F corona, the radiation acceleration to gravitational acceleration ratio will no longer remain constant when the particles reach the region where they begin sublimation. The magnitude of the acceleration due to radiation pressure increases as the particle size decreases and results in the particle experiencing a continual decrease in the effective mass of the sun. This equates to an increase in the potential energy of the grain, which results in an increase in the semimajor axis of the particle's orbit (Lamy, 1974; Mukai, 1983). We will call this the sublimation effect. At some specific distance from the sun, the sublimation rate is such that it will balance the P-R drag and the semimajor axis of a particle's orbit will temporarily remain stable. This region should be observable as an enhancement in the brightness of zodiacal light due to the enhancement of particle number density.

Recent observations have detected such an enhancement in the density of orbiting dust particles at about 4 R_0(solar radii). Maihara et al. (1985) used photoelectric scans to detect thermal emission from dust in the F corona during the June 1983 total solar eclipse in Indonesia. They described their findings as dust rings around the sun at 3.5 R_0 and 4 R_0 near the solar equatorial plane. During the eclipse of November 1966 Peterson (1967, 1969) observed an emission peak in the infrared (λ = 2.2 μm) surrounding the sun at about 4 R_0. During the same eclipse, MacQueen (1968) observed brightness enhancements at 3.4 R_0 and 4.1 R_0 in a radial scan, also at 2.2 μm, and at 4 R_0 during a balloon flight on January 9, 1967. Finally, during the February 1979 eclipse Beavers et al. (1980) detected a radial velocity component of the dust in the F corona which matches that expected from Keplerian orbital motion.

Because the sun is not a point source, the radiation from different points of origin on the solar surface will appear at different frequencies due to the Doppler effect. The P-R drag and radiation pressure comprise the non-Doppler average of these source points, and when they are subtracted from the total radiation distribution, the residual radiant energy will add an additional drag term to the P-R drag (Guess, 1962). This is because the leading hemisphere of the solar disk appears bluer, and hence the particle intercepts photons of higher energy from the leading hemisphere as opposed to the trailing hemisphere.

Another effect of the sun's finite diameter is due to the Doppler shift of solar radiation caused by the sun's rotation. This effect, similar to the effect of a finite solar diameter, will generate a force in the solar equatorial plane normal to the line between the particle and the sun's center. Unless the dust particle is orbiting in the solar equatorial plane, this force will have a component perpendicular to the particle's orbital plane and can thus affect the inclination of the particle's orbit.

CHAPTER II

PLANETARY PERTURBATIONS AND THE STRUCTURE OF THE ZODIACAL CLOUD

A. Introduction

Cometary debris and particles released in asteroidal collisions are believed to be the two main sources of the zodiacal dust. Because the asteroids are, for the most part, in relatively circular orbits at low inclinations to the invariable plane of the solar system, it is expected that these particles would form a homogeneous, time invariant component of the zodiacal cloud. Much work has been done (cf. Gustafson, 1985) on the dynamics of dust grains in circular orbits under the influence of planetary perturbations combined with P-R drag. Although certain features, such as the Schuerman arcs (Schuerman, 1980) which result from orbital resonance with the planets, are expected to form regions of enhanced dust density, in general, asteroidal dust is expected to manifest itself as a fairly homogeneous dust cloud.

Comets, on the other hand, have highly eccentric orbits which frequently undergo drastic changes due to close interactions with the planets, especially Jupiter. Most of the dust from comets is released while the comet is near perihelion, where the higher temperature allows the ices which bind the refractory material to the comet to sublimate, thus releasing this material. A change in the comet's perihelion distance will therefore strongly affect the amount of dust released. If the zodiacal dust is mainly due to cometary debris, it may be possible to determine which comet released the dust and when it was released, if structures relating to specific perihelion passages of likely cometary suppliers of the interplanetary dust can be observed.

B. The Method

To determine the effect of gravitational perturbations on the cometary dust, 196 particles were released at differing perihelion passages of comet Encke. Because the orbital period of this comet has a seven to two commensurability with the orbital period of the planet Jupiter, particles were chosen in groups of seven consecutive perihelion passages in order to determine if the evolution of the cometary particle orbits depend on the Jupiter-sun-particle angle at release. Each of these seven release "phases" could then be studied separately.

Due to the commensurability in orbital period, comet Encke's orbital parameters are strongly influenced by the planet Jupiter. The result of this influence is a periodic variation in the comet's orbital elements with respect to Jupiter's orbital plane (Whipple, 1940). Figure 2.1 (Whipple, 1940, p. 730) demonstrates how these parameters vary with time. In our simulations, we used the periodic variation in inclination to determine the times at which our particles would be released. By studying particles released when the comet was

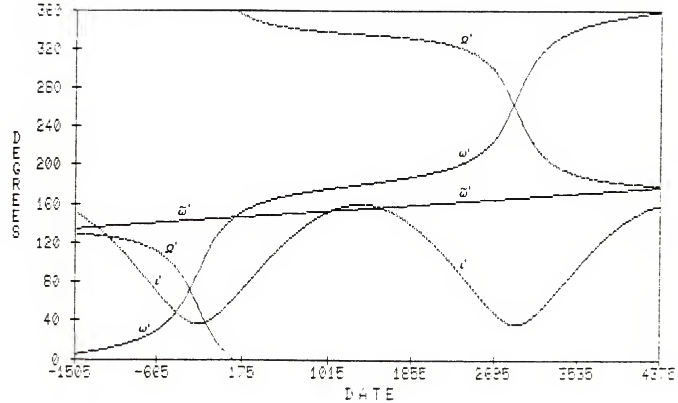

Figure 2.1. Variation of the orbital parameters of comet Encke. Here, the orbital parameters are measured with respect to the orbital plane of Jupiter.

at a minimum possible inclination, at a midpoint (10°) of inclination, and at a maximum inclination, we could see if there were any effects of initial inclination on the final fate of each cometary particle. Also, it was important to include a range of input values to get an accurate determination of the distribution of cometary dust at any given time.

At release, we assumed that the relative velocity between the comet and the particle was zero. Any micron-sized particle leaving a comet is suddenly subjected to a radiation pressure induced acceleration much greater than that on the comet, and its velocity (the comet's velocity) is too high to remain on the comet's orbital path. Because radiation pressure effectively decreases the central force, the dust particle's orbit increases in both semimajor axis and eccentricity. In fact, if the radiation acceleration to gravitational acceleration ratio, β, is such that

$$\beta > \frac{(1 - e_c)}{2} , \tag{2.1}$$

where e_c is the eccentricity of the comet, then the dust particle will be released in a hyperbolic orbit. This sets a lower limit to the size of cometary dust. In our simulations, we chose to use dust particles 30 microns in diameter ($\beta = 0.02$) to represent an intermediate value for zodiacal dust, which is believed to be between 1 and 100 microns (Giese and Grun, 1976) in size. The resulting particles' orbital paths had semimajor axes of 2.89 A.U. and eccentricities of .884, compared to comet Encke's values of 2.21 A.U. and .848, respectively. The other orbital parameters remain as those of the comet, except for the orbital period which increased by nearly 50%. The significance of the increase in semimajor axis is that the particle's orbit crosses that of Jupiter, so that close encounters with this massive planet become likely. This can greatly affect the subsequent evolution of the particle's orbit.

From the equations of Wyatt and Whipple (1950), the time it would take a particle to reach the inner solar system from the initial input semimajor axis and eccentricity can be determined. This has been tabulated for several values of the particle's semimajor axis (table 2.1). It can be seen that a particle requires between 15,000 and 20,000 years to reach the inner solar system, and so the times of particle release in our simulations were set between 26,000 BC and 6,000 BC (figure 2.2). The longer timespan of 20,000 years, as compared to the 5,000 years required to cover all possible release times for particles solely under the influence of P-R drag, was needed to compensate for the effect of planetary perturbations on the spiralling-in time of the cometary dust.

Table 2.1. The time required for a particle released from comet Encke to reach a particular semimajor axis under the influence of the Poynting-Robertson effect, and the resulting eccentricity.

Semimajor Axis (AU)	Eccentricity	Time from release (yr)
1.050000	0.705010	13082.38
0.950000	0.678761	14008.29
0.850000	0.647662	14968.27
0.750000	0.610368	15964.00
0.650000	0.565083	16994.10
0.550000	0.509462	18052.78
0.450000	0.440659	19124.28
0.350000	0.355914	20172.94

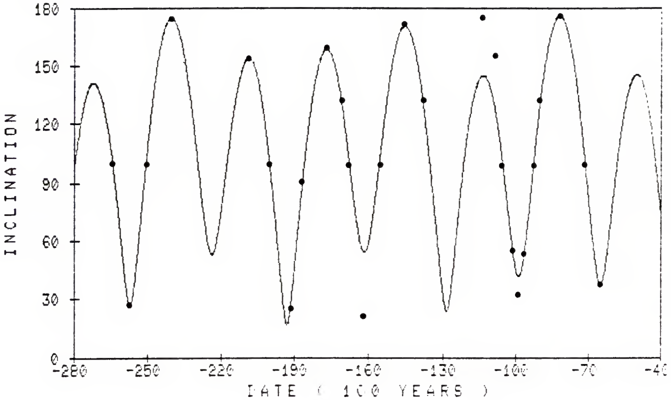

Figure 2.2. The initial dates and inclinations of particles at release. Each point corresponds to 7 particles released at 7 consecutive perihelion passages of the comet. Points not on the curve, resulting from an error in the input computations, will not apply to P. Encke, but their inclusion does not affect the conclusions drawn in this chapter. The curve represents the inclination of comet Encke during this period.

The evolution of the particle's path through the solar system was solved by using Encke's method. Here the osculating orbit of the particle was divided into two hundred equal time increments, and, at each of these times, the acceleration of the dust particle from P-R drag as well as that due to the planets from Venus through Jupiter was determined. The perturbations on the osculating orbit were computed using the Gaussian perturbation equations (Moulton, 1914). The changes in the orbital elements were then integrated over one orbit using Simpson's rule, and the osculating orbit was corrected at the end of each orbit. When tests were performed on the method using particles run without planetary encounters, the constant resulting from the effect of radiation pressure as determined by Wyatt and Whipple (1950),

$$C = a_p e_p^{-4/5} (1 - e_p^2) ,$$

remained constant to at least four decimal places (the extent of our printout) thoughout the 20,000 orbits of the test particle.

When the particle approached within the zone of influence of a planet (Chapter IV will contain more about the range of planetary influence) the integration was completed and the particle's path was computed by determining the change in position and velocity vectors in Cartesian coordinates (Cowell's method). The size of the time increment was decreased to 1/40,000th of an orbital period throughout the Cowell's method procedure. This method was continued until the particle was sufficiently far from the planet that Encke's method could once again be used.

Each particle was then run until either the semimajor axis fell below .3 astronomical units, the perihelion distance fell below two solar radii, or the particle's semimajor axis failed to fall below 2.5 A.U. after 10,000 orbits, which indicated that the particle's orbit became dominated by Jupiter. Most of the particles required between 10,000 and 20,000 orbits to reach one of these criteria and took approximately one hour of cpu time per 1000 orbits; therefore each particle run required about one day to complete on a VAX/750.

C. Results

The distribution of the particles was analyzed by generating histograms of several orbital elements as well as the time since release for values of the semimajor axis from 2.75 to .35 A.U. or for 20 different dates separated by 1500 year intervals. Also, the inclination of each particle was plotted as a function of its longitude of the ascending node. These figures can be found in Appendix B.

In the plots of inclination vs. longitude of the ascending node there appears to be no correlation between the two orbital elements. In fact, the orbital planes of the dust particles appear to be distributed randomly about the ecliptic ($i = 0°$) plane, with the number density of particles falling off at inclinations greater than about 20° (figure 2.3). However, a glance at the histograms of inclination show a marked decrease in the particle density for inclinations between 0° to 3°. This is due to the nature of measuring an angle such as inclination, which is restricted to the range from 0° to 180°.

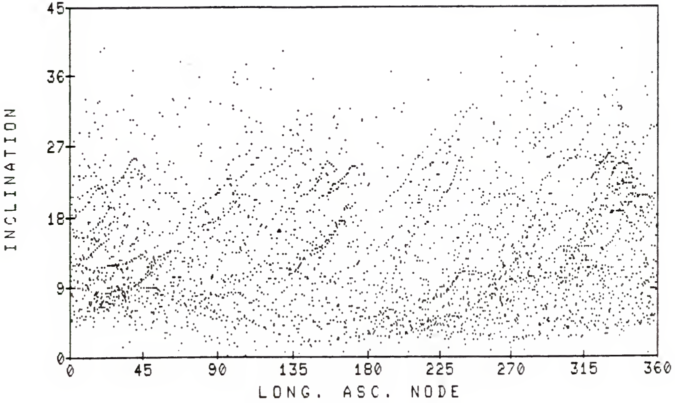

Figure 2.3. This figure represents the total of figures B.51 through B.75. Each particle is represented by up to 25 points corresponding to the 25 values of the semimajor axis studied.

A histogram across all semimajor axes (figure 2.4) strongly exhibits this effect.

Statistically, if a particle is placed in a random orbit, the angular momentum vector of a particle's orbit should be equally likely to point in any direction. Specifically, this means that the probability of the angular momentum unit vector ending in any surface element of a unit sphere is the area of that surface element divided by the area of the sphere (4π). If a sphere is sliced parallel to its equatorial plane such that the areas of the resulting surfaces are equal, the size of the angle subtended by the areas is not constant. In order to have a constant area on the sphere the slices must be made at equal increments of the cosine of the inclination. Histograms of the number density of particles at equal intervals of the cosine of the inclination for various values of the semimajor axis (Appendix B, figures B.26 to B.50) show that the particles are indeed driven toward lower inclinations.

The number densities of the particles found at the lowest inclinations (figure 2.5) imply that the particles are selectively removed from those ranges of inclination inhabited by the planets. This is to be expected since close encounters between the dust particles and the planets are much more likely to occur when the orbital planes of the two bodies nearly coincide. In figure 2.5, the three outermost planets in our study, Jupiter, Mars, and Earth, are found in the zones of the last two bars, and the cosine of the inclination of the planet Venus is .99824, which puts that planet squarely in the fourth bar from the right, a bar that is clearly low in particle number

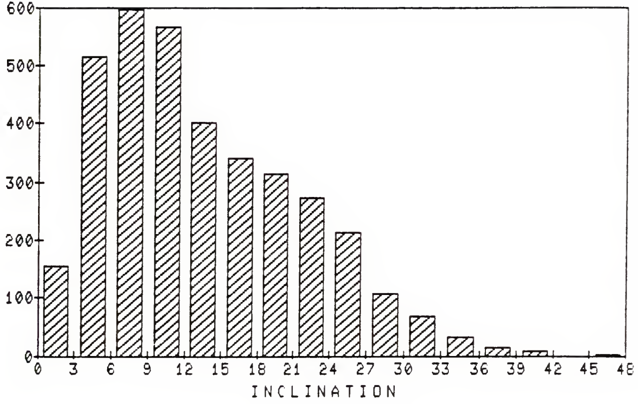

Figure 2.4. Number density of particles at various inclinations. This is the sum of figures B.1 through B.25.

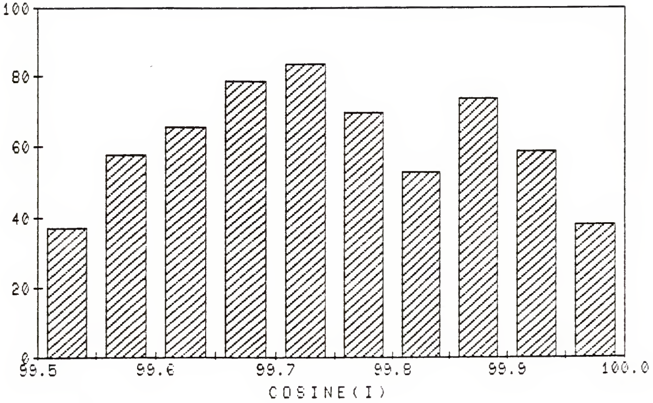

Figure 2.5. Number density of particles vs. the cosine of the inclination, for inclinations near the ecliptic.

density. This close-up study of the inclination does not detract from the fact that, overall, particle density increases toward lower values of the inclination. Unfortunately, there is not enough structure in the available data to determine whether the symmetry plane of the particles in the simulations is related to the orbital plane of any particular planet.

It has been frequently stated that particles in the inner solar system will be in nearly circular orbits due to the decrease in eccentricity resulting from the P-R drag, and Wyatt and Whipple (1950) have been referenced as the source of this belief. However, table 2.1 demonstrates that cometary particles will be found in eccentric orbits even when their semimajor axes are as small as 0.35 A.U. Figure 2.6 shows how P-R drag alone would affect the evolution of both the perihelion and aphelion distances of a particle released from comet Encke. Observe that the distance between the two values stays large for most of the particle's lifetime.

The eccentricity of the cometary simulation particles has been catalogued in Appendix B, for values of the semimajor axis from 2.75 A.U. to 0.35 A.U. in steps of .1 A.U. Figure 2.7 shows the median eccentricity as a function of semimajor axis for our 196 particles. The lower curve in this figure represents the single value which would result if the effect of the planets were excluded. *BY CONTRAST, IT CAN THUS BE SEEN THAT THE PLANETS INCREASE THE ECCENTRICITY OF THE MAJORITY OF THE DUST PARTICLES RELEASED FROM COMET ENCKE.*

The effect of the planets on the time the particles required to fall toward the sun can be seen in figure 2.8. The upper curve in

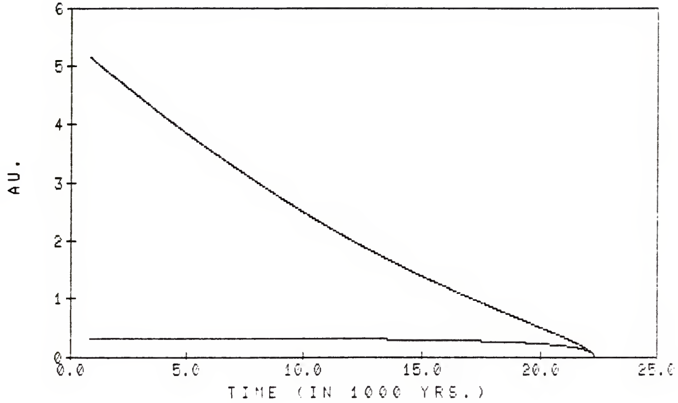

Figure 2.6. The effect of P-R drag on the perihelion and aphelion distances of a cometary particle.

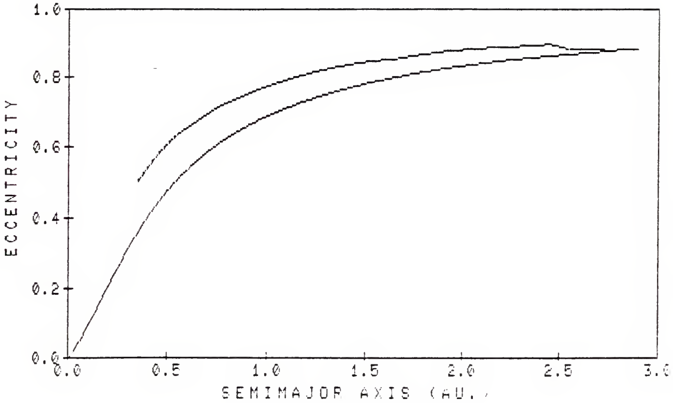

Figure 2.7. The median eccentricity of the simulation particles as a function of semimajor axis. The lower curve represents the effect of P-R drag alone.

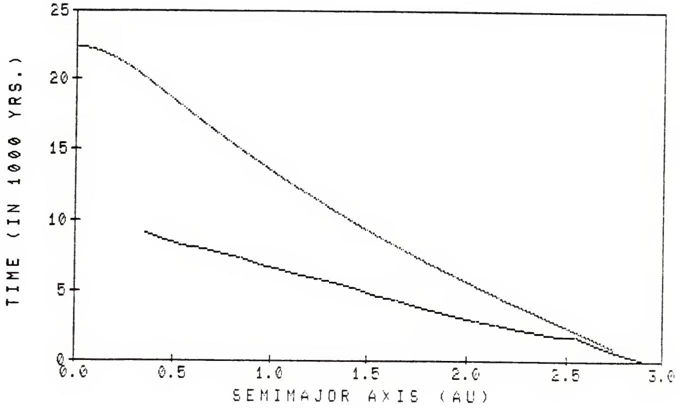

Figure 2.8. The median time from release for various values of the semimajor axis. The upper curve represents the effect of P-R drag alone.

this figure represents the infall time derived from P-R drag. *IT IS CLEAR THEN THAT THE MAJORITY OF THE PARTICLES HAVE THEIR LIFETIMES SIGNIFICANTLY SHORTENED BY INTERACTIONS WITH THE PLANETS.* This result does not show whether planetary encounters, as well as slow secular changes due to more distant planets, affect the particle's semimajor axes directly to cause this reduction in lifetime or indirectly through a strengthening of the P-R drag due to the increase in eccentricity discussed above.

The P-R lifetime of a particle in an eccentric orbit is smaller than the lifetime of a particle with the same semimajor axis in a circular orbit (Wyatt and Whipple, 1950), because the increase in the P-R drag near perihelion more than compensates for the decrease when the particle is at distances greater than its semimajor axis. A particle that has had its eccentricity increased by planetary encounters will have its P-R lifetime correspondingly decreased; thus the effect of the planets on the eccentricities of the particles can, at least partly, explain the reduction in P-R lifetime.

To determine whether this effect is the sole cause of the decrease in the lifetime of the simulation particles, the eccentricity and "age" of the particles were compared with the P-R values based on the median eccentricity of a particle at 2.45 A.U. (figures 2.9 and 2.10) and at 1.55 A.U. (figures 2.11 and 2.12). The semimajor axis 2.45 A.U. was chosen as the largest value of semimajor axis that guaranteed that the particles would not cross Jupiter's orbital path. The other value, 1.55 A.U., was chosen since a small deviation in the smoothness of the upper curve in figures 2.7 and 2.9 occurred

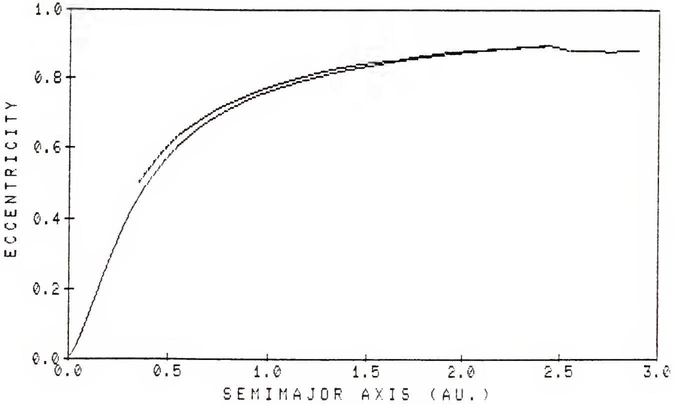

Figure 2.9. Same as figure 2.7 except the lower curve was calculated from the value of the upper curve of 2.45 A.U.

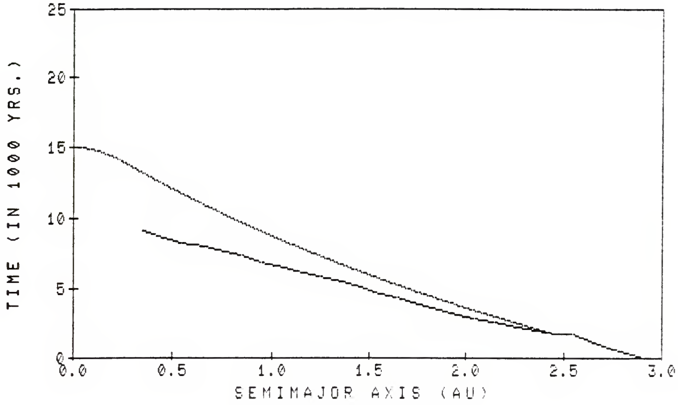

Figure 2.10. Same as figure 2.8 with the exception noted in figure 2.9.

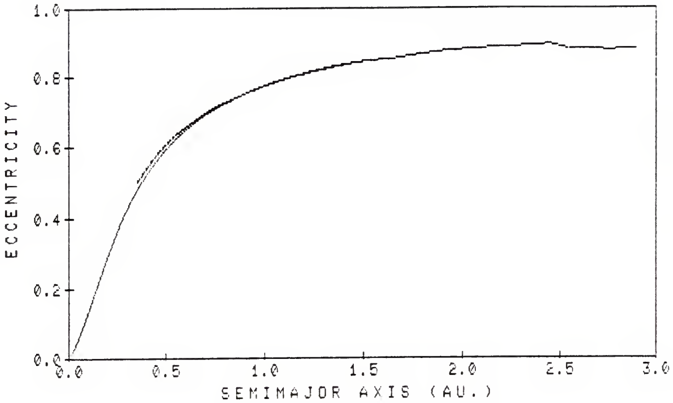

Figure 2.11. Same as figure 2.9 except the lower curve starts at 1.55 A.U.

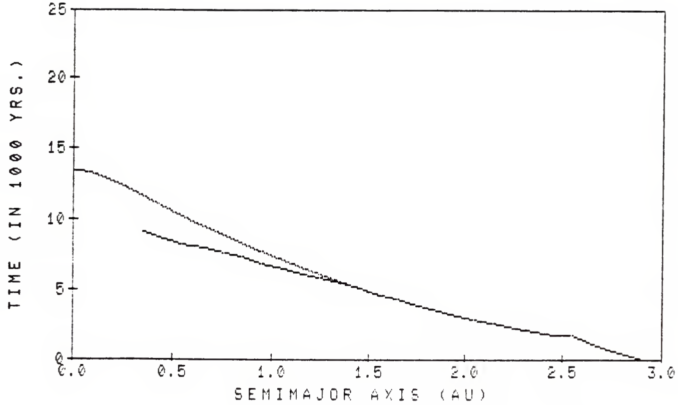

Figure 2.12. Same as figure 2.10 with the lower curve starting at 1.55 A.U., as in figure 2.11.

between 1.55 and 1.65 A.U. The resulting figures (2.10, 2.12) show that even after the higher eccentricity is compensated for, the particles still show a tendency to reduce their semimajor axes more rapidly than P-R drag would predict. *THIS IMPLIES THAT THE EFFECT OF GRAVITATIONAL INTERACTIONS WITH THE PLANETS MOST OFTEN TEND TO REDUCE A PARTICLE'S SEMIMAJOR AXIS.*

The longitudes of the perihelia of the particles in our simulations are preferentially aligned away from the direction $\tilde{\omega} = 240°$, measured in a prograde sense from the direction of the vernal equinox. This can be seen in the histograms of Appendix B (figures B.101 through B.125) and has been summed over all semimajor axes in figure 2.13. *THIS ALIGNMENT IS NOT RELATED TO THAT OF THE COMET, WHICH HAS ITS VALUE OF THE LONGITUDE OF PERIHELION VARYING THROUGH AN ENTIRE CYCLE OF 360° DURING THE 20,000 YEAR RELEASE PERIOD.* Also, the perihelion directions appear to be more strongly ordered for a constant value of the semimajor axis rather than across all semimajor axes at any given time, implying that such an alignment would be a stable feature in three dimensions.

D. Conclusion

Any results based on the dust released from comet Encke should apply to any prograde comet of low inclination, since it is apparent from the simulations that the planet Jupiter causes a catastrophic realignment of the dust when the dust is in Jupiter crossing orbits. Even those dust particles with high inclinations have a good chance

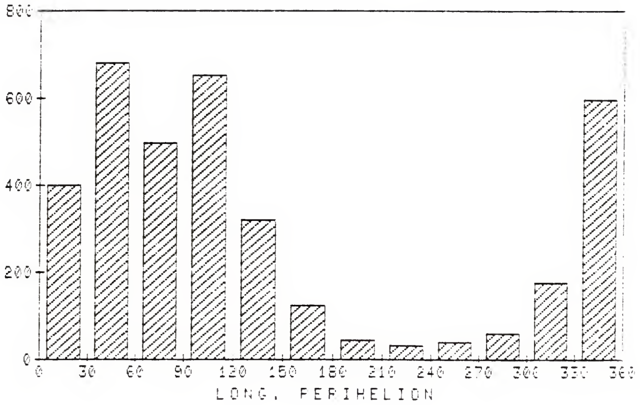

Figure 2.13. Number density of particles vs. the longitude of perihelion. This is the sum of figures B.101 through B.125.

of a close encounter with Jupiter, since P-R drag will eventually bring the particles' orbital paths to intersection with Jupiter's orbit.

One effect of planetary perturbations is to slowly draw the dust particles toward the planets' orbital planes. This is in line with observations (Leinert et al., 1981) which show the very well known fact that zodiacal light brightness increases toward the ecliptic.

A surprising result is the determination that the eccentricities of the particle orbits remain high throughout much the particles' lifetimes. Observations have not yet been made which can distinguish between particles in circular orbits and those in eccentric orbits. The most recent results (East and Reay, 1984) confirm that at least 50% of the dust particles are in closed prograde orbits about the sun. Theoretical studies of the dynamics of particles near the sun (Lamy, 1974; Mukai et al., 1974) imply that most interplanetary grains eventually lose enough mass through sublimation to evolve into particles with hyperbolic orbits (β-meteoroids), thus explaining the percentage which are not in closed orbits.

The asymmetry in the longitude of perihelion of the cometary dust is apparently a feature of the solar system in general and not specific to comet Encke, since the orientation of the comet appears to have no effect on the direction of the feature. That there has been no observation of such a feature would imply that the majority of interplanetary dust particles are in orbits of low eccentricity.

It appears that dust from comet Encke does not meet all the criteria required of a source of the zodiacal cloud. The median lifetime of particles released from the comet is shortened, so that the total particle mass required to supply the zodiacal dust would be even more than previous estimates based solely on the P-R lifetime (Mukai et al., 1983), which conclude that cometary dust is an insufficient source. Radiation pressure eliminates cometary dust below the lower limit set by equation 2.1, thus much of the mass of a periodic comet will be ejected from the solar system, further reducing the initial supply of interplanetary dust. Finally, the lack of asymmetry in the distribution of interplanetary dust implies that the dust orbits are predominantly of low eccentricity, a result we have shown to be inconsistent with a cometary origin.

CHAPTER III

INITIAL PARTICLE DISTRIBUTION OF THE F CORONA

In order to study particle dynamics in the F corona, the first order of business is to determine the size, charge, chemical composition, and orbital elements of particles as they enter the region. We can consider the F corona and the rest of the zodiacal cloud as two separate regions if our criterion for dividing the two is to consider the rest of the zodiacal cloud as that region where radiation pressure (including P-R drag) and gravitational interactions are the only significant forces affecting the dynamics of interplanetary dust.

The Lorentz force from the interplanetary magnetic field cannot be entirely neglected anywhere in the solar system, but for 10-100 μm particles it is small compared to the perturbations from the planets. In particular, in the outer regions of the solar system where the tangential component of the interplanetary field generates forces comparable to the P-R drag, the effect of the planets is significantly enhanced due to their large masses and the weakening of the sun's gravitational field.

The size of dust particles in the F corona depends on several factors which can reduce the size of particles as they approach the sun, as well as, of course, the initial sizes of the interplanetary particles. Particle collection studies in the Earth's upper atmosphere

(Brownlee et al., 1980) as well as interplanetary space probes (Pailer and Grün, 1980) and the study of lunar microcraters (LeSargent and Lamy, 1978) point to there being two populations of particles responsible for the zodiacal light. Population I particles are dark fluffy conglomerates of silica and silicates with most of the particles being between 10 and 100 microns in diameter. These particles are in prograde, low eccentricity orbits about the sun. The particles which comprise population II are less than 1 micron in diameter and appear to be streaming outward from the sun in hyperbolic orbits. It is believed that the number density of particles in the two populations are approximately equal (Giese and Grün, 1976).

Apparently, the population II particles are the remnants of the larger particles after the dust has undergone sublimation in the F corona. This would seem to be the most reasonable explanation, although this has not been discussed in the literature. It is based on this conjecture that we intend to study only those particles larger than 1 micron. In any case, it has been shown that population I particles are responsible for 90% of the zodiacal light (East and Reay, 1984).

The reduction in size of the interplanetary particles can result from four effects:

1. Sublimation of the particle,
2. Sputtering, which is an eroding of the particle caused by bombardment of solar wind ions,
3. Rotational bursting, and
4. Collisions.

Of these four mechanisms, sublimation can be ignored since this mechanism is confined (by definition) to the F corona. In the case of rotational bursting, there are many mechanisms known which result in the rotation of dust particles (Radzievskii, 1954; Misconi, 1975; Paddack and Rhee, 1975). Because the particles appear to be fluffy conglomerates and not solid crystals, their tensile strength is relatively low and thus the particles are apparently easy to burst. Misconi (1975) has shown that random changes in rotation due to solar wind ion impacts may cause rotational bursting of particles during solar flares, although mechanisms which slow the particle spin rate could not be included in the analysis. Other rotation mechanisms are capable of spinning the particles up to bursting speed much more rapidly than random ion impacts, but these depend on the existence of specific types of structure on the surfaces of the dust particles, as well as a stable alignment of the particle spin axis. Such mechanisms are not well understood at the present time.

In our present work, we will not include rotational bursting as a significant factor in determining the size of the dust grains as they reach the F corona. There are three main reasons for excluding rotational bursting:

1. A search for enhancement of the zodiacal light from solar flares failed to discover any evidence of such an occurrence.
2. A particle breaking up will experience a sudden change in the central force field due to an enhancement in radiation pressure, thus many such particles will be driven from the solar system (see equation 2.1).
3. Misconi's (1975) analysis implies that bursting will occur only in particles less than 1 micron in diameter based on a tensile strength for solid materials (for interplanetary grains the value may be much lower). Applicability of this mechanism to the larger grains in our study is unclear.

Sputtering, like sublimation, causes a slow degradation in the sizes of interplanetary dust particles. Unlike sublimation, sputtering can affect particles outside the F corona. The sputtering rate of interplanetary dust particles measured in Å/year (Bandermann, 1968) is

$$ds = 3.2 \frac{dt}{\rho a^2} \qquad 3.1$$

where dt is measured in years, ρ is measured in grams/cm^3, and a is measured in A.U. Here we have taken a value intermediate to Bandermann's maximum and minimum values for the sputtering rate of iron particles and adjusted for the lower density of fluffy particles. An adjustment was also made in the sputtering yield per ion as being a factor of the density of iron. We can then calculate the size of a particle in a *CIRCULAR* orbit by substituting for dt from the equation

$$da = \left(\frac{\alpha}{a}\right) dt \qquad 3.2$$

(Wyatt and Whipple, 1950), where $\alpha = \frac{3.6}{s\rho}$. Here ρ is measured in grams per cm^3, and s is in Ångströms, as was ds. Combining equations 3.1 and 3.2 we get

$$\frac{ds}{s} = \frac{8}{9} \frac{da}{a} ,$$

which, when integrated gives

$$s = s_0 \left(\frac{a}{a_0}\right)^{8/9} . \qquad 3.3$$

If, for example, s_0 = 30 μ at 1 A.U., then it will have been reduced to 2.1 μ at .05 A.U. (approximately 10 R_0).

Collisions will certainly reduce the size of interplanetary particles. In our study of the F corona we will ignore the effect of collisional reduction since particles broken up by collision will most likely become β-meteoroids and never reach the F corona.

The end result of the question of the size of dust particles entering the F corona is that sputtering is the main reducing factor of particle size in the inner solar system. Based on equation 3.3, we expect the interplanetary dust, which is mainly between 10 and 100 microns in size at 1 A.U., to be between .7 and 7 microns in size upon reaching the F corona.

There is much disagreement as to the charge of particles in the F corona. Burke and Silk (1974) suggest a negative charge for graphite particles at temperatures less than 8000 K. The applicability of this result must be questioned because of the low photoelectric yield in the environment under study (HI regions) as compared to the near solar environment. Millet et al. (1980) derive a value of ~ +3 volts for the potential of spherical graphite particles near the sun, after reaching a negative value of -40 volts at about 10 R_o. Mukai (1981) states that the particle will remain positively charged throughout the inner solar system, with the potential gradually increasing above +10 volts in the minimum solar wind while reaching only +4.8 volts if the solar wind is at maximum. All of these results are for graphite, although Burke and Silk state that the behavior of silicates is closely related. Lacking a definitive value of the charge of dust grains in the F corona, we will assign an arbitrary value of +10 volts. The implications of an error in our chosen value of the charge will be discussed in the next chapter.

Since the chemical composition of the dust particles has been determined (Brownlee et al.,1980), at least for those particles in the neighborhood of the Earth, as being silica and silicates, there remains only to determine the orbital elements of the particles as they enter the F corona.

In the previous chapter, the orientation of the particles' orbital planes with respect to the ecliptic plane was determined to vary, with somewhat more particles having low inclination orbits, rather than high inclination orbits. There appears to be no preferential value for the longitude of the ascending node of the particles studied. We will adopt Leinert et al.'s (1976) fan model for the particle density since it fits our results rather nicely.

The semimajor axis of F coronal dust will be adopted as being between 3.5 R_0 and 4.5 R_0, from the observations discussed in Chapter I and from theoretical considerations (Lamy, 1974).

The eccentricities of dust particle orbits will be reduced by P-R drag as given by Wyatt and Whipple (1950). Planetary effects on the eccentricity of the orbits are small compared to that of P-R drag inside the orbit of Mercury. Table 3.1 is an extension of table 2.1 and shows the eccentricity of an average cometary particle as it approaches the F corona. It can be seen from table 3.1 that the eccentricity of a particle in the F corona is less than 0.04, even for our cometary particle with a high eccentricity at release. In our study, we will assume that our particles are initially in circular orbits, and so there is no need to consider the asymmetry in the direction of perihelion.

Table 3.1. The effect of P-R drag on the eccentricity and the P-R lifetime of a cometary particle near the sun.

Semimajor Axis (A.U.)	Eccentricity	Time from Release (yrs.)
0.350000	0.355914	20172.94
0.350000	0.307176	20667.81
0.250000	0.254588	21127.42
0.200000	0.199120	21535.42
0.150000	0.142485	21874.59
0.100000	0.087226	22128.76
0.080000	0.066262	22203.70
0.060000	0.046378	22262.47
0.040000	0.027986	22304.68
0.030000	0.019543	22319.50
0.025000	0.015563	22325.32
0.020000	0.011776	22330.09

CHAPTER IV

PLANETARY INFLUENCE IN THE F CORONA

Besides determining the distribution of dust particles at the beginning of their "lifetime" in the F corona, we need to know just what effect planetary perturbations have on particles oribiting in the F corona. Since planets are in nearly circular orbits and the region of the F corona is within 10 solar radii (.05 A.U.) of the center of the sun, a planet's semimajor axis is the approximate distance between the planet and the particle at all times. Thus by determining the size of the region in which a planet can have a significant influence on an orbiting particle, we will determine if any such planet has a zone of influence as large as its semimajor axis.

Tisserand's (1889) definition of the "sphere of action" of a planet is based on the equality of tidal vs. gravitational acceleration ratios of the sun and planet. Öpik (1951) and others based their relation on equating the differential solar and planetary forces on the particle. Neither expression was formulated to describe the zone of influence surrounding a planet when considering the small, but significant, perturbative effects of the planets on a particle's orbital elements. For the purpose of determining these effects on interplanetary dust we derive a zone of influence based on equating the gravitational forces of the sun and planet and demonstrate its applicability.

In the process of computing the orbital evolution of dust particles in interplanetary space, it was necessary to determine whether or not a particle was close enough to a planet that integrating the perturbing forces using Encke's method was no longer valid. Both expressions for the "sphere" of influence of a planet proved to be inadequate when the geometries of subsequent interactions were considered. In particular, when each relation was scaled to one planet, it could not be generalized to the other planets. Consequently, the formula for the zone of influence must depend strongly on the specific subject to be studied. We have pursued this problem from several different viewpoints and expect that, besides being useful in studies of interplanetary dust, our findings may apply to studies of asteroids, comets, and the stability of asteroidal satellites.

The general expression for the radial distance to the boundary of the planetary zone of influence on small particles can be written as

$$s = k \cdot f(a_p) \cdot g(m_p, \text{ other planetary parameters}) \qquad 4.1$$

where k is a constant which depends on the nature of the problem under study, f and g are functions which may also have the same dependence as k, a_p is the planet's semimajor axis, and m_p is the planet's mass. The other parameters may include the eccentricity of the planet, as well as the other orbital parameters and such factors as oblateness and axial tilt. Functions f and g are generally not separable but we have found that the effect of semimajor axis can be separated from the other parameters. The equations of Tisserand (1889) and Öpik (1951) can be written as

$$s = \left(\frac{1}{M_o}\right)^{2/5} a_p m_p^{2/5}, \text{ and} \tag{4.2}$$

$$s = \frac{1}{2}\left(\frac{1}{2M_o}\right)^{1/3} a_p m_p^{1/3}, \text{ respectively.} \tag{4.3}$$

If we equate the gravitational and radiation forces of the sun and planet, a different relationship is obtained. Consider a particle of mass m at a distance s from a planet of mass m_p and semimajor axis a_p, and at a distance r from the sun. The magnitude of the force on the particle due to the planet is

$$F = \frac{Gm_p m}{s^2}, \tag{4.4}$$

while the magnitude of the force on the particle due to the sun is

$$F = GM_o m \frac{(1 - \beta)}{r^2}, \tag{4.5}$$

where β is the ratio of radiation pressure to the sun's gravitational force. Since $a_p - s < r < a_p + s$, we can write r as $r = a_p + \delta s$ where δ is a number between -1 and +1 which depends on the planet-particle-sun angle. Substituting $M_o' = M_o(1 - \beta)$ we can set the ratio of the solar force to the planetary gravitational force equal to some constant k^2, where

$$\frac{k^2 Gm_p m}{s^2} = \frac{GM_o' m}{(a_p + \delta s)^2}, \text{ which reduces to} \tag{4.6}$$

$$s = ka_p\left(\frac{m_p}{M_o'}\right)^{1/2}\left[1 - k\delta\left(\frac{m_p}{M_o'}\right)^{1/2}\right]^{-1}. \tag{4.7}$$

Equation 4.7 can be approximated by a simple power law when the mass of the planet and k are small (compared to the sun), giving

$$s = (\frac{k}{M_o'^{\,1/2}})a_p m_p^{\,1/2} \; . \qquad 4.8$$

Compare this with the results of Tisserand and Öpik, equations 4.2 and 4.3.

A computer simulation technique was used to find the most applicable expression for our study. Each encounter was run using a 10,000 step Cowell's method computation over one synodic period of the orbit. For a particle in circular orbit at 10 A.U., the errors in eccentricity and semimajor axis incurred over one orbit were less than 1×10^{-5}, and 5×10^{-9} A.U., respectively, and there was no observable error in inclination. The particle was initially in a circular orbit and the planet was given a fixed orbital eccentricity. The encounter occurred at perihelion or aphelion, depending on whether the particle's orbit was inside or outside the planet's orbit. The particle's orbital plane coincided with that of the planet except when the change in inclination of the particle was under study. In this case, the particle's initial inclination was determined by the distance of closest approach, so that encounters above and below the planet's orbital plane could be studied. A comparison was made between the minimum encounter distance and a_p or m_p under the condition of constant Δe, Δi, or $\frac{\Delta a}{a}$.

Figure 4.1a shows the effect of a_p on the zone size for a constant Δe and verifies the linear relation, common to all derivations, between the zone boundary and the semimajor axis. This result also shows that the uncoupling of the functional forms of a_p and m_p in equation 4.1 is valid. The constant change $\Delta e = 0.0014$ chosen in deriving figures 4.1a and 4.1b (and later 4.3) is the minimum value that guarantees that the zones of influence of the inner five planets do not overlap. Similar linear relationships (not shown) were found when Δi and $\frac{\Delta a}{a}$ were held constant.

The encounters were computed with the gravitational interactions of the sun and planet affecting the particle continuously throughout one synchronous orbit and not just at the point of closest approach to the planet. Equations 4.2, 4.3, 4.7, and 4.8 were derived by considering only one point in the particle-planet-sun system. So far, we have assumed a relation between the distance of closest approach in our simulation results and the distance s in these equations. The linear relationship between a_p and the distance of closest approach in figure 4.1a demonstrates that our assumption is useful. Some effects of the difference between the derived equations and the numerical simulations of the complete encounters will be discussed later.

Figure 4.1b shows the effect of the planet's mass on the zone boundary when Δe is held constant. The general trend follows the power law of equation 4.8 and diverges from the power law in the same manner as equation 4.7. Figure 4.2 is a graphic representation of equation 4.7. While this and the previous figure show a striking similarity, the spread due to

$$[1 - k\delta(\frac{m_p}{M'_o})^{1/2}]^{-1}$$

is greater than the spread observed in the simulations. This is a

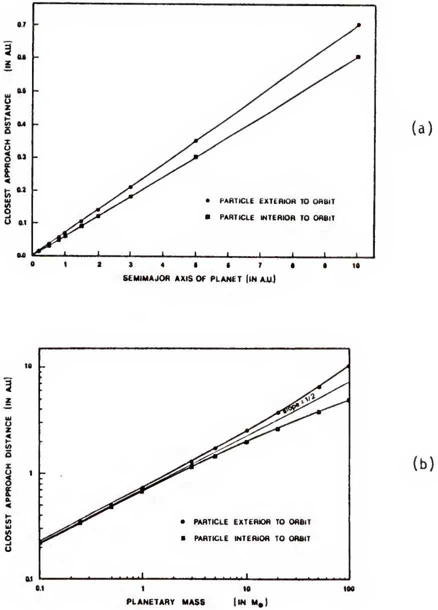

Figure 4.1. Relation between closest approach distance and planetary characteristics for a constant change in a particle's orbital eccentricity. a) Relation between closest approach distance and the semimajor axis of a planet of 1 earth mass. b) Relation between closest approach distance and the mass of a planet orbiting at 10 A.U.

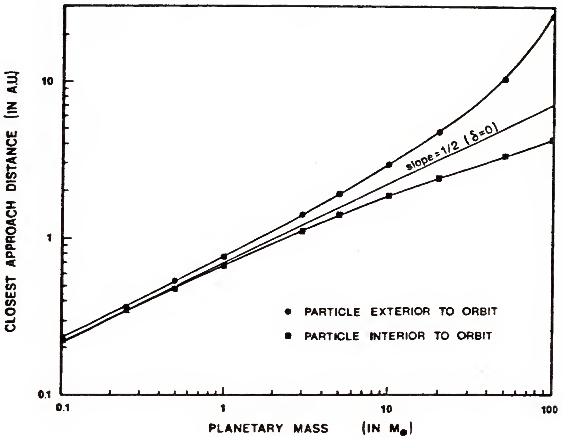

Figure 4.2. A graphic representation of equation 4.7 for a planet orbiting at 10 A.U.

consequence of the difference mentioned above, due to the fact that, during an encounter, δ assumes values other than +1 or -1. However, the power law relation, found by averaging the two curves, is not affected by this consideration and demonstrates the applicability of equations 4.7 and 4.8.

Figure 4.3 shows the effect of planetary eccentricity (e_p) on the zone boundary. As implied in equation 4.1, this effect cannot be separated from the functional dependence on planetary mass. This is evidenced by the fact that these results match those for high mass planets but diverge from those of low mass. This is evidently caused by a difference in the velocity relationship between the particle and the planet. When the particle encounters an exterior planet at perihelion, the particle will usually have the greater velocity. However, if the encounter distance

$$s < \frac{2a_p e_p}{(1 + e_p)} ,$$

the planet will have the greater velocity and will overtake the particle. In figure 4.3, the inequality is true when s is less than .95 A.U. A similar effect applies when the particle's position is outside that of a planet at aphelion. The resulting increase in the encounter time thus causes the downward curvature at the low mass end of the curves in figure 4.3.

Figures 4.4a and 4.4b show the relationship between planetary mass and the distance of closest approach under the condition that $\frac{\Delta a}{a} = 5 \times 10^{-5}$ (figure 4.4a) or $\Delta i = 0.0011$ (figure 4.4b). Unlike the result for a constant Δe in figure 4.2, the boundary follows the form

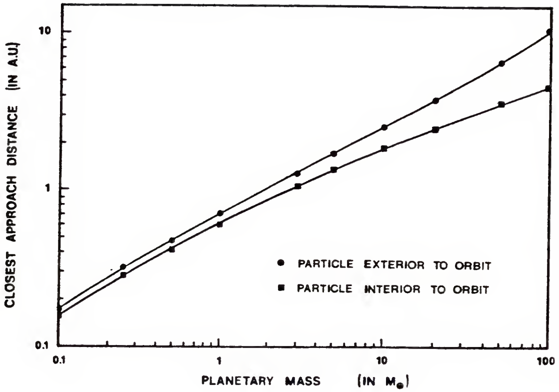

Figure 4.3. This is the same as figure 4.1b except the planet's orbit has an eccentricity of 0.05.

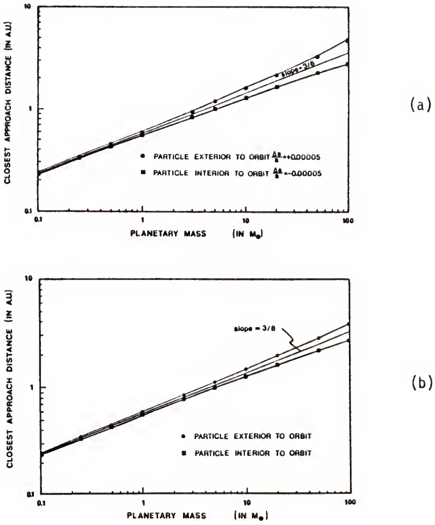

Figure 4.4. Relation between the mass of a planet and the closest approach distance for a constant change in a particle's a) semimajor axis, b) inclination.

$$s \propto \left(\frac{m_p}{M_o'}\right)^{3/8} , \qquad 4.9$$

a result which matches no theoretical formula yet derived. Note, also, the divergence from the power law for planets of high mass, similar to the form in equation 4.7.

THE FORM OF THE RELATION DETERMINING THE ZONE OF INFLUENCE IS HIGHLY DEPENDENT ON THE NATURE OF THE PERTURBING EFFECT TO BE OBSERVED. Note that the expressions most applicable to interactions with orbiting particles involve powers of the planetary mass not formerly considered, and the size of the zone boundary depends upon the planet's eccentricity. The importance of the 3/8 exponent in the power law relation, discovered for constant Δi and $\frac{\Delta a}{a}$ suggests a need for further analytical study.

We can gain insight into the significance of planetary perturbation on the orbital elements of the particles by considering the "k" factor in the expression for the size of the zone boundary as a measure of the inverse magnitude of the perturbations. Substituting the semimajor axis in place of the size of the zone boundary in equation 4.7, and replacing the exponent (1/2) by the more generalized E,

$$\text{Perturbations} = \frac{1}{k} = \left(\frac{m_p}{M_o'}\right)^{E} (1 + \delta) ; \qquad 4.10$$

which implies that, in the F corona, the relative influence of the planets depends solely on the mass of each planet. There is the factor of 1 + δ to be considered, since δ is always very close to -1. In the F corona, 1 + δ is equal to the angular distance between the sun and the particle, as seen from the planet. If we consider the maximum angular distance in radians between the sun and the particle, then that angle is the radius of the particle's orbit divided by the semimajor axis of the planet's orbit. Entering the value $\frac{4R_o}{a_p}$ for $1 + \delta$, we arrive at

$$\frac{1}{k} = \frac{4R_o \left(\frac{m_p}{M_o'}\right)^E}{a_p} . \qquad 4.11$$

The significance of this result is that perturbations due to the nearest planet, Mercury, are less than those of Venus, Earth, and Jupiter, in spite of the fact that these planets are much farther from the F corona. In fact, *JUPITER IS THE STRONGEST PERTURBER OF ORBITING DUST IN THE F CORONA, REGARDLESS OF THE EXPONENT OF THE MASS.* From the simulations above, we know that, for a constant change in inclination, the exponent E in equation 4.11 is 3/8. In this case, Mercury, Venus, and Earth all contribute at least half of the inclination change caused by Jupiter. Table 4.1 displays the relative effects of the planets (Jupiter = 1) at the maximum angular distance between the sun and a particle orbiting at 4 solar radii, for several values of the exponent of the mass, E, in equation 4.11.

Table 4.1. The relative magnitudes (Jupiter = 1) of planetary perturbations in the F corona, for various values of the dependence on planetary mass.

Planet	a_p	Mass	1-delta	K(1/3)	K(3/8)	K(0.4)	K(1/2)
Mercury	0.387	0.055	0.0481	0.7489	0.5220	0.4204	0.1768
Venus	0.723	0.820	0.0257	0.9865	0.7696	0.6630	0.3653
Earth	1.000	1.000	0.0186	0.7623	0.5996	0.5192	0.2918
Mars	1.524	0.107	0.0122	0.2375	0.1702	0.1394	0.0626
Jupiter	5.203	317.900	0.0036	1.0000	1.0000	1.0000	1.0000
Saturn	9.539	95.200	0.0020	0.3649	0.3470	0.3367	0.2985
Uranus	19.182	14.600	0.0010	0.0971	0.0854	0.0791	0.0581
Neptune	30.058	17.200	0.0006	0.0655	0.0580	0.0539	0.0403
Pluto	39.440	0.002	0.0005	0.0024	0.0015	0.0011	0.0003

CHAPTER V

THE EFFECT OF THE SOLAR MAGNETIC FIELD

A. An Overview

The solar magnetic field, carried by the solar wind, is expected to interact with orbiting particles through the Lorentz force. The most recent models of the solar magnetic field (Schulz et al., 1978; Hoeksema, 1984) assume that there exists a surface above the solar photosphere where all the magnetic field lines are radial, and that beyond this surface the magnetic field streams outward at the velocity of the solar wind, describing an Archemedian spiral (Parker, 1963). Inside this "source surface" the field increases in complexity until, at the photosphere, it can be described by a series of multipole components. The source surface gives accurate fits when it is modelled between 2 and 2.85 solar radii. Although ellipsoidal shapes have been used for the source surface (Schulz et al., 1978), the spherical model of Hoeksema (1984) used in this analysis is equally accurate in reproducing the observations and can be used to derive analytical expressions.

Since we will be dealing with the magnetic field outside the source surface, we must apply the equations for the Parker spiral pattern. The radial component of the magnetic field at a distance r from the center of the sun is

$$B_r(r) = B_o\left(\frac{R_s}{r}\right)^2 \qquad 5.1$$

where R_s is the radius of the source surface and B_o is the magnetic field strength at the source surface, taking the finite velocity of the field into account when determining the position on the source surface where the field originated. The tangential component of the field at the heliocentric distance r is

$$B_\phi(r) = -B_o\left(\frac{R_s}{r}\right)^2 \frac{\omega_o R_s}{v_{sw}} \left(\frac{r}{R_s} - 1\right) \sin\theta \qquad 5.2$$

or

$$B_\phi(r) = -B_r(r) \frac{\omega_o R_s}{v_{sw}} \left(\frac{r}{R_s} - 1\right) \sin\theta \qquad 5.3$$

where θ is the colatitude of the position of field measurement. The factor $\frac{\omega_o R_s}{v_{sw}}$ can be calculated as follows. Approximately, the sun rotates once each month and there are about $\pi \times 10^7$ seconds in a year, so that the angular rotation rate of the sun

$$\omega_o = \frac{2\pi \times 12}{\pi \times 10^7} = 2.4 \times 10^{-6} \text{ rad/sec}$$

and $R_s = 2.5\ R_o$ where R_o is about 7.5×10^5 km. The quiet solar wind velocity is 400 km/sec (Gustafson and Misconi, 1979) so

$$\frac{\omega_o R_s}{v_{sw}} = \frac{2.4 \times 10^{-6} \times 7.5 \times 10^5}{4 \times 10^2} = 4.5 \times 10^{-3}\ .$$

The maximum value of the tangential component for any given radial distance to the sun occurs in the solar equatorial plane where $\sin\theta = 1$.

In the F corona, the distance to the sun is less than 10 solar radii, so the maximum value of the tangential component of the interplanetary magnetic field is

$$B_\phi(r) < B_r(r) \times 4.5 \times 10^{-3} \times 9 \times 1$$

which is $< 5 \times 10^{-2}$ times the field strength of the radial component and therefore will be ignored in the analytical analyses that follow in this chapter.

All of the previous expressions require knowing the field strength at the source surface. Although I have ascribed no functional dependence to B_0, it is in fact a function of time and the position angles θ and ϕ. The magnetic field at the source surface, can be found from the multipole components by substituting $r = R_s$ into the expression for the radial component of the solar magnetic field used by Hoeksema (1984, p. 44, equation 3.1) in determining these components. The resulting expression

$$B_0 = (2l+1)\left(\frac{R_0}{R_s}\right)^{l+2} P_l^m (\cos\theta)\,(g_{lm}\cos m\phi + h_{lm}\sin m\phi) \qquad 5.4$$

is time dependent because the multipole components, g_{lm} and h_{lm} are themselves time dependent. The P_l^m functions are the second order Legendre functions, the first three terms of which can be found in Appendix A.

The Lorentz force acting on the orbiting dust grains due to the solar magnetic field will perturb the orbits of the coronal dust. In general, this force will act on any orbiting body and the force acting on that body for a given position, velocity, and time is

$$\vec{F} = \frac{q}{c} (\vec{v}_g - \vec{v}_{sw}) \times \vec{B} \qquad 5.5$$

where $\vec{v}_g$ is the velocity of the body (grain) with respect to the inertial coordinate system, $\vec{v}_{sw}$ is the solar wind velocity with respect to that system, q is the net charge of the orbiting body, $\vec{B}$ is the magnetic field vector for the given position and time, and c is the velocity of light. Note that $\vec{v}_{sw}$ also represents the velocity of the magnetic field since the field is "frozen" in the plasma.

The dust particles in this region are expected to be in nearly circular orbits due to the decrease in eccentricity from the P-R drag (discussed in Chapter III), and therefore their velocity vectors are nearly perpendicular to the magnetic field lines. The Lorentz force is then mainly due to the velocity of the particle, since the solar wind velocity is nearly parallel to the magnetic field in this region. The skewing of the field lines (i.e., the Archemedian spiral; Parker, 1963), as shown from the above analysis, takes place at further heliocentric distances than those under consideration. The resulting force is normal to the particle's orbital plane, so only those orbital elements which can be affected by a force perpendicular to the particle's orbit will display significant changes.

B. The Dipole Component

During sunspot minimum, the solar magnetic field can be characterized by a polar dipole field. The higher order multipole components are very weak compared to the dipole terms, and the magnitude of the equatorial dipole component of the field is low enough so that the total dipole field, which is a sum of the polar and equatorial dipole components, is inclined less than 5° to the solar rotation axis.

For approximately half of a solar cycle, there is a strong equatorial dipole term, especially during those times around sunspot maximum. The equatorial dipole is usually accompanied by relatively strong components in the higher order multipoles.

The radial field at the source surface due only to these dipole terms can be written (from equation 5.4) as

$$B_o = 3\left(\frac{R_o}{R_s}\right)^3 \sum_{m=0}^{1} P_1^m(\cos\theta)(g_{1m}\cos m\phi + h_{1m}\sin m\phi) \ , \qquad 5.6$$

where θ is the polar angle and ϕ is the azimuthal angle as measured from the direction of zero solar longitude. Expanding this gives only three terms, since $\sin(0\phi) = \sin(0) = 0$. Substituting $P_l^m(\cos\theta)$ from Appendix A, equations A.9, we then get

$$B_o = 3\left(\frac{R_o}{R_s}\right)^3 [g_{10}\cos\theta + g_{11}\sin\theta\cos\phi$$

$$+ h_{11}\sin\theta\sin\phi] \ . \qquad 5.7$$

Since the tangential component of the interplanetary magnetic field can be neglected, we can write the expression for the magnetic field at the particle's position by substituting equation 5.7 into equation 5.1

$$B_r(r) = k(r)\,[g_{10}\cos\theta + g_{11}\sin\theta\cos\phi$$

$$+ h_{11}\sin\theta\sin\phi] \ , \qquad 5.8$$

where $k(r) = 3(\frac{R_o}{R_s})(\frac{R_o}{r})^2$. Using the transformations of Appendix A (equations A.13), we can write the expression for the magnetic field in terms of the particle's orbital inclination i, the longitude of the ascending node Ω, and u, the position angle of the particle from its ascending node. Note that the orbital elements of the particle used here and in future expressions are based on the solar equatorial coordinate system. The expression for the magnetic field at the particle becomes

$$B_r(r) = k(r)[g_{10}\sin\Omega\sin i - g_{11}(\cos\Omega\cos u - \sin\Omega\sin u\cos i) - h_{11}(\sin\Omega\cos u + \cos\Omega\sin u\cos i)] . \qquad 5.9$$

The force on the particle due to the magnetic field can be found by substituting equation 5.9 into the Lorentz force equation (5.5). Because the magnetic field is assumed to be radial, expression 5.5 can be rewritten as

$$\bar{W} = -\frac{qv_g}{c} B_r(r) \qquad 5.10$$

where $\bar{W}$ is the component of the force perpendicular to the particle's orbital plane. The other components of the force ($\bar{S}$ and $\bar{T}$) are, in this case, 0.

To determine the effect of this force on the particle's orbital elements, we examine the Gaussian perturbation equations (Moulton, 1914; see Appendix A, equations A.14-A.19). It is apparent that only the inclination, ascending node, and the longitude of perihelion can be affected by the Lorentz force. Since the eccentricity is assumed to be zero, there is no perihelion direction and we need only concern ourselves with changes in i and Ω.

In order to better understand the role each component of the magnetic field plays in altering the orbital elements of a dust particle in the F corona, the expressions for the change in the orbital elements due to components g_{10}, g_{11}, and h_{11} will be written separately. The effect of g_{10} on the inclination is

$$\frac{di}{dt} = -\left(\frac{qv_g}{nacm}\right)k(r)\ g_{10}\sin u\cos u\sin i\ , \tag{5.11a}$$

and the effect of g_{10} on the ascending node is

$$\frac{d\Omega}{dt} = -\left(\frac{qv_g}{nacm}\right)k(r)\ g_{10}\sin^2 u\ . \tag{5.11b}$$

If we substitute for dt in terms of u and du (Appendix A, equation A.13) and integrate both sides over one orbit, with the assumption that the variations in i and Ω are small over the course of one orbit, we get

$$\oint di = -C(r)\ g_{10} \oint \sin u\cos u\ du\ ,$$

and

$$\oint d\Omega = -C(r)\ g_{10} \oint \sin^2 u\ du\ ,$$

where $C(r) = \left(\frac{qv_g}{n^2acm}\right)k(r)$, which can be integrated to give

$$\Delta i(g_{10}) = 0 \tag{5.12a}$$

$$\Delta\Omega(g_{10}) = -\pi C(r)\ g_{10}\ . \tag{5.12b}$$

The effect of the g_{11} dipole component of the solar magnetic field on a particle's orbital alignment

$$\frac{di}{dt} = (\frac{qv_g}{nacm})k(r)\ (\cos\Omega\cos^2 u - \sin\Omega\sin u\cos u\cos i)g_{11} \qquad 5.11c$$

and

$$\frac{d\Omega}{dt} = (\frac{qv_g}{nacm})k(r)\ (\cos\Omega\sin u\cos u\csc i - \sin\Omega\sin^2 u\cot i)g_{11} \qquad 5.11d$$

results in the integral equations

$$\oint di = C(r)\ g_{11}\ [\cos\Omega \oint \cos^2 u\ du - \sin\Omega\cos i \oint \sin u\cos u\ du]$$

and

$$\oint d\Omega = C(r)\ g_{11}\ [\cos\Omega\csc i \oint \sin u\cos u\ du - \sin\Omega\cot i \oint \sin^2 u\ du]$$

which, after performing the required integrations, give

$$\Delta i(g_{11}) = \pi C(r)\ g_{11}\ \cos\Omega \qquad 5.12c$$

and

$$\Delta\Omega(g_{11}) = -\pi C(r)\ g_{11}\ \sin\Omega\cot i\ . \qquad 5.12d$$

Finally, we take the expressions for the change in the orbital elements due to the h_{11} component,

$$\frac{di}{dt} = (\frac{qv_g}{nacm})k(r)\ h_{11}\ (\sin\Omega\cos^2 u + \cos\Omega\sin u\cos u\cos i) \qquad 5.11e$$

and

$$\frac{d\Omega}{dt} = (\frac{qv_g}{nacm})k(r)\ h_{11}\ (\sin\Omega\sin u\cos u\csc i + \cos\Omega\sin^2 u\cot i) \qquad 5.11f$$

which we can integrate as before to get

$$\Delta i(h_{11}) = \pi C(r)\, h_{11} \sin\Omega \qquad 5.12e$$

and

$$\Delta\Omega(h_{11}) = \pi C(r)\, h_{11} \cos\Omega \cot i\ . \qquad 5.12f$$

From equation 5.12a, it is evident that the polar dipole component (g_{10}) has no effect on the inclination of a particle's orbital plane and from equation 5.12b, it is seen that there is a constant monotonic change in Ω due to the polar dipole component. Because the elements i and Ω are based on a chosen coordinate system, the results for the effect of the polar dipole component can be extrapolated to show that the effect of any solar dipole field is to precess the particle's orbital plane about the dipole axis. When one or both of the equatorial dipole terms are strong, the precession results in a significant change in the inclination. Keep in mind that this is the effect of a radial field which originates from a solar dipole field and not just the effect of a magnetic dipole.

C. The Quadrupole Terms

An examination of the relative strengths of the dipole and quadrupole components of the solar magnetic field over more than half a solar cycle from 1976 through 1983 (Hoeksema, 1984) reveals only two instances in 1980 when the magnitude of the quadrupole component was greater than that of the dipole component, and in each case it was the low strength of the dipole which enabled the quadrupole components to dominate. Nonetheless, the magnitude of the quadrupole field was, except at sunspot minimum, at least 30% of the dipole field strength, and any analysis which does not include the effects of the quadrupole terms would be incomplete.

That part of the double sum in equation 5.4 which involves only the quadrupole terms can be written

$$B_0 = 5\left(\frac{R_0}{R_s}\right)^4 \sum_{m=0}^{2} P_2^m(\cos\theta)[g_{2m}\cos m\phi + h_{2m}\sin m\phi] \ . \tag{5.13}$$

This can be expanded out to the five g and h coefficients (h_{20} is meaningless) by substituting for $P_2^m(\cos\theta)$ from equation A.9 to get

$$B_0 = 5\left(\frac{R_0}{R_s}\right)^4 \left[\frac{1}{2}(3\cos^2\theta - 1)g_{20} - 3\sin\theta\cos\theta(g_{21}\cos\phi + h_{21}\sin\phi) + 3\sin^2\theta(g_{22}\cos 2\phi + h_{22}\sin 2\phi)\right] ,$$

and, since the radial field drops off as $\left(\frac{R_s}{r}\right)^2$,

$$B_r(r) = 5\left(\frac{R_0}{R_s}\right)^2 \left(\frac{R_0}{r}\right)^2 \left[\frac{1}{2}\ (3\cos\theta - 1)g_{20} - 3\sin\theta\cos\theta(g_{21}\cos\phi + h_{21}\sin\phi) + 3\sin^2\theta(g_{22}\cos 2\phi + h_{22}\sin 2\phi)\right] \ . \tag{5.14}$$

Substituting for θ and ϕ the orbital parameters relative to the solar equatorial coordinate system, i, Ω, and u, we get

$$B_r(r) = 5(\frac{R_o}{R_s})^2 (\frac{R_o}{r})^2 \{\frac{1}{2} (3\sin^2 u \sin^2 i - 1) g_{20}$$

$$- 3\sin u \sin i[(\sin\Omega\cos u + \cos\Omega\sin u\cos i) h_{21}$$

$$+ (\cos\Omega\cos u - \sin\Omega\sin u\cos i) g_{21}]$$

$$- 3[(\sin\Omega\cos u + \cos\Omega\sin u\cos i)^2$$

$$- (\cos\Omega\cos u - \sin\Omega\sin u\cos i)^2] g_{22}$$

$$+ 6(\cos\Omega\cos u - \sin\Omega\sin u\cos i)$$

$$\times (\sin\Omega\cos u + \cos\Omega\sin u\cos i) h_{22}\} .$$

The Lorentz force on the particle due to the magnetic field generated by a solar quadrupole component is then

$$\bar{W} = - \frac{5qv_g}{c} (\frac{R_o}{R_s})^2 (\frac{R_o}{r})^2 \{\frac{1}{2} (3\sin^2 u \sin^2 i - 1) g_{20}$$

$$- 3\sin u \sin i(\sin\Omega\cos u + \cos\Omega\sin u\cos i) h_{21}$$

$$- 3\sin u \sin i(\cos\Omega\cos u - \sin\Omega\sin u\cos i) g_{21}$$

$$- 3[(\sin\Omega\cos u + \cos\Omega\sin u\cos i)^2$$

$$- (\cos\Omega\cos u - \sin\Omega\sin u\cos i)^2] g_{22}$$

$$+ 6(\cos\Omega\cos u - \sin\Omega\sin u\cos i)$$

$$\times (\sin\Omega\cos u + \cos\Omega\sin u\cos i) h_{22}\} ,$$

which affects only the inclination and ascending node as was discussed in the case of the dipole field. These changes are

$$\begin{aligned}
\frac{di}{dt} = \frac{5qv_g \cos u}{nacm} \left(\frac{R_o}{R_s}\right)^2 \left(\frac{R_o}{r}\right)^2 \{ \frac{1}{2} (1 - 3\sin^2 u \sin^2 i) g_{20} \\
&+ 3\sin u \sin i (\sin\Omega \cos u + \cos\Omega \sin u \cos i) h_{21} \\
&+ 3\sin u \sin i (\cos\Omega \cos u - \sin\Omega \sin u \cos i) g_{21} \\
&+ 3[(\sin\Omega \cos u + \cos\Omega \sin u \cos i)^2 \\
&- (\cos\Omega \cos u - \sin\Omega \sin u \cos i)] g_{22} \\
&- 6(\cos\Omega \cos u - \sin\Omega \sin u \cos i) \\
&\times (\sin\Omega \cos u + \cos\Omega \sin u \cos i) h_{22} \} ,
\end{aligned}$$

and

$$\begin{aligned}
\frac{d\Omega}{dt} = \frac{5qv_g \sin u}{nacm} \sin i \left(\frac{R_o}{R_s}\right)^2 \left(\frac{R_o}{r}\right)^2 \{ \frac{1}{2} (1 - 3\sin^2 u \sin^2 i) g_{20} \\
&+ 3\sin u \sin i (\sin\Omega \cos u + \cos\Omega \sin u \cos i) h_{21} \\
&+ 3\sin u \sin i (\cos\Omega \cos u - \sin\Omega \sin u \cos i) g_{21} \\
&+ 3[(\sin\Omega \cos u + \cos\Omega \sin u \cos i) \\
&- (\cos\Omega \cos u - \sin\Omega \sin u \cos i)] g_{22} \\
&- 6(\cos\Omega \cos u - \sin\Omega \sin u \cos i) \\
&\times (\sin\Omega \cos u + \cos\Omega \sin u \cos i) h_{22} \} ,
\end{aligned}$$

respectively. By substituting $dt = \frac{T}{(2\pi)} du$ the integral equations

$$\begin{aligned}\oint di = \frac{5qv_g}{(n^2acm)} \{g_{20}.5 \oint \cos u \, du - 1.5 \sin^2 i \oint \sin^2 u \cos u \, du]\\
+ 3\cos i[(h_{21}\cos\Omega - g_{21}\sin\Omega)\sin i + (g_{22}\cos 2\Omega\\
- h_{22}\sin 2\Omega)\cos i] \oint \sin^2 u \cos u \, du\\
+3[(h_{21}\sin\Omega + g_{21}\cos\Omega)\sin i + 2(g_{22}\sin 2\Omega\\
- h_{22}\cos 2\Omega)\cos i] \oint \sin u \cos^2 u \, du\\
- 3[g_{22}\cos 2\Omega + h_{22}\sin 2\Omega] \oint \cos^3 u \, du\}\end{aligned}$$

and

$$\begin{aligned}\oint d\Omega = \frac{5qv_g}{(n^2acm \sin i)} \{g_{20}[.5 \oint \sin u \, du - 1.5\sin i \oint \sin^3 u \, du]\\
+ 3\cos i[(h_{21}\cos\Omega - g_{21}\sin\Omega)\sin i + (g_{22}\cos 2\Omega\\
- h_{22}\sin 2\Omega)\cos i] \oint \sin^3 u \, du\\
+3[(h_{21}\sin\Omega + g_{21}\cos\Omega)\sin i + 2(g_{22}\sin 2\Omega\\
- h_{22}\cos 2\Omega)\cos i] \oint \sin^2 u \cos u \, du\\
- 3[g_{22}\cos 2\Omega + h_{22}\sin 2\Omega] \oint \sin u \cos^2 u \, du\}\end{aligned}$$

are reached. On examining each equation, and comparing the imbedded integrals to equations A.1-A.5 in Appendix A, it can be seen that

$$\Delta i(\text{quadrupole}) = 0$$

and

$$\Delta\Omega(\text{quadrupole}) = 0 .$$

THE SURPRISING RESULT IS THAT THE QUADRUPOLE MOMENT OF THE SOLAR

MAGNETIC FIELD HAS NO EFFECT ON THE ORIENTATION OF AN ORBITING PARTICLE'S ORBITAL PLANE.

D. Octupole Components

The octupole terms in the solar magnetic field can usually be neglected since there are only a few instances (in the nine years of observational record, 1976-1984) when the octupole field strength came within 25% of the dipole or quadrupole terms. Because a multipole term is less by a factor of $\frac{R_o}{R_s}$ at the source surface than the next lower order when the two multipole orders are of comparable strength at the photosphere, the higher order terms will contribute very little to the interplanetary magnetic field. The octupole term is of interest because the lack of influence of the quadrupole field on the orientation of the particle's orbit prevents the effects of the octupole field from becoming overshadowed.

The expanded expression for the octupole component of the magnetic field at the source surface is

$$\begin{aligned} B_o = 7 \left(\frac{R_o}{R_s}\right)^5 & [P_3^0(\cos\theta)g_{30} + P_3^1(\cos\theta)(g_{31}\cos\phi + h_{31}\sin\phi) \\ & + P_3^2(\cos\theta)(g_{32}\cos 2\phi + h_{32}\sin 2\phi) \\ & + P_3^3(\cos\theta)(g_{33}\cos 3\phi + h_{33}\sin 3\phi) \ . \end{aligned}$$

We can multiply this expression by $\left(\frac{R_s}{r}\right)^2$ to represent the field at the distance of the particle and then multiply the result by $\frac{qv_g}{c}$ to get the expression for the force on the particle due to the octupole component of the magnetic field. When we then substitute the expressions for the Legendre polynomials (equations A.9) we get

$$\begin{aligned}\bar{W} = - F_0(r)[&g_{30}\cos\theta(5\cos^2\theta - 3)\\ &- 3g_{31}\sin\theta(5\cos^2\theta - 1)\cos\phi - 3h_{31}\sin\theta(5\cos^2\theta - 1)\sin\phi\\ &+ 30g_{32}\cos\theta\sin^2\theta(\cos^2\phi - \sin^2\phi) + 60h_{32}\cos\theta\sin^2\theta\sin\phi\cos\phi\\ &- 15g_{33}\sin^3\theta\cos\phi(\cos^2\phi - 3\sin^2\phi)\\ &- 15h_{33}\sin^3\theta\sin\phi(3\cos^2\phi - \sin^2\phi)] \qquad 5.15\end{aligned}$$

where

$$F_0(r) = \frac{3.5qv_g}{c} \left(\frac{R_o}{R_s}\right)^3 \left(\frac{R_o}{r}\right)^2 .$$

It is easiest to see the effects of the individual component g's and h's by deriving the effect of each term separately on i and Ω. For g_{30}, after replacing those functions of θ and ϕ with expressions based on the orbital elements i, Ω, and u, and then substituting the first term of equation 5.15 into the Gaussian perturbation equations (A.16 and A.18), the change in inclination after one orbit becomes

$$\begin{aligned}\Delta i(g_{30}) = - F_1(r)[&5\sin^3 i \oint \sin^3 u\cos u\, du\\ &- 3\sin i \oint \sin u\cos u\, du]g_{30}\end{aligned}$$

where

$$F_1(r) = \frac{F_0(r)}{(n^2am)} = \frac{3.5qv_g}{(n^2ac)} \left(\frac{R_o}{R_s}\right)^3 \left(\frac{R_o}{r}\right)^2 ,$$

or

$$\Delta i(g_{30}) = 0$$

and the change in the longitude of the ascending node is

$$\Delta\Omega(g_{30}) = -\ F_1(r)[5\sin^2 i \oint \sin^4 u\ du - 3 \oint \sin^2 u\ du]g_{30}\ ,$$

or

$$\Delta\Omega(g_{30}) = 3\pi\ F_1(r)[1 - 1.25\ \sin^2 i]g_{30}\ .$$

The g_{30} term has no effect on the inclination, but does precess the orbit. It should be noted here that if $\sin^2 i = \frac{4}{5}$, the orbit will no longer precess.

A similar analysis can be applied to the g_{31} term. The expression for Δi is

$$\begin{aligned}\Delta i(g_{31}) = 3F_1(r)[&5\sin^2 i\cos\Omega \oint \sin^2 u\cos^2 u\ du \\ &- \cos\Omega \oint \cos^2 u\ du - 5\sin^2 i\cos i\sin\Omega \oint \sin^3 u\cos u\ du \\ &+ \cos i\sin\Omega \oint \sin u\cos u\ du]g_{31}\ .\end{aligned}$$

When the values for the integrals (equations A.6-A.8) are substituted and the terms collected, the resulting expression becomes

$$\Delta i(g_{31}) = 3\pi\ F_1(r)\cos\Omega[1.25\ \sin^2 i - 1]g_{31}\ .$$

When $\sin^2 i = \frac{4}{5}$ and $\cos\Omega$ is negative, any increase in i which causes a corresponding increase in the absolute value of $\sin i$ will cause a corresponding decrease in Δi, so that a stable resonance is reached. This occurs when i is about 63.4 degrees.

The expression for the change in the longitude of the ascending node due to the g_{31} component of the solar magnetic field is

$$\Delta\Omega(g_{31}) = \frac{3F_1(r)}{\sin i}\,[5\sin^2 i\cos\Omega \oint \sin^3 u\cos u\;du$$

$$- \cos\Omega \oint \sin u\cos u\;du - 5\sin^2 i\cos i\sin\Omega \oint \sin^4 u\;du$$

$$+ \cos i\sin\Omega \oint \sin^2 u\;du]g_{31}\ ,$$

which becomes

$$\Delta\Omega(g_{31}) = 3\pi\ F_1(r)\ \cot i\sin\Omega\ [1 - 3.75\ \sin^2 i]g_{31}\ .$$

There is also a resonance here, for when

$$\cot i[1 - 3.75\ \sin^2 i] \qquad 5.16$$

is positive, Ω will proceed toward 180 degrees, at which point it will become stable. This independent analysis of the equilibrium points of i and Ω does not tell the entire picture, since the stable point of inclination results in expression 5.16 becoming negative which causes Ω to move toward 0°. Then when cosΩ becomes positive (when Ω reaches the first or fourth quadrants), the expression for Δi becomes positive and any small difference in i from the equilibrium position will cause it to move farther away from equilibrium. We expect the result of this coupling of i and Ω to be a constant oscillation between the equilibrium values of i and Ω.

The g_{32} term in the solar magnetic field generates a change

$$\Delta i(g_{32}) = -\ 30F_1(r)\ \sin i\ [(\cos 2\Omega - \sin 2\Omega) \oint \sin u\cos^3 u\;du$$

$$- (\cos 2\Omega - \sin 2\Omega)\cos^2 i \oint \sin^3 u\cos u\;du$$

$$- 2\cos i\sin 2\Omega \oint \sin^2 u\cos^2 u\;du]g_{32}\ ,$$

which reduces to

$$\Delta i(g_{32}) = -\ 7.5\pi\ F_1(r)\ \sin 2i \sin 2\Omega\ .$$

The corresponding change in the longitude of the ascending node is

$$\Delta\Omega(g_{32}) = -\ 30F_1(r)[\cos 2\Omega \oint \cos^2 u \sin^2 u\ du$$
$$-\cos 2\Omega \oint \sin^4 u\ du - 2\cos i \sin 2\Omega \oint \sin^3 u \cos u\ du]g_{32}$$

or

$$\Delta\Omega(g_{32}) = -\ 7.5\pi\ F_1(r)\ \cos 2\Omega(1 - 3\cos^2 i)\ .$$

Because both expressions (for Δi and $\Delta\Omega$) have an Ω dependence which goes as 2Ω, any results for a given Ω will also apply to an Ω 180 degrees greater (or smaller). There should be a stable equilibrium at $2\Omega = 270°$ and $2i = 360°$.

Finally, the integral expressions for g_{33} are

$$\Delta i(g_{33}) = 30F_1(r)\ \{\cos\Omega(1 - 4\sin^2\Omega)\ [\oint \cos^2 u\ du$$
$$-\ 3\cos^2 i \oint \cos^2 u \sin^2 u\ du]$$
$$-\ \sin\Omega(1 - 4\cos^2\Omega)\ [\cos^3 i \oint \sin^3 u \cos u\ du$$
$$-\ 3\cos i \oint \sin u \cos^3 u\ du]\}g_{33}\ ,$$

and

$$\Delta\Omega(g_{33}) = 30F_1(r)\ \{\cos\Omega(1 - 4\sin^2\Omega)\ [\oint \cos^3 u \sin u\ du$$
$$-\ 3\cos^2 i \oint \cos u \sin^2 u\ du]$$
$$-\ \sin\Omega(1 - 4\cos^2\Omega)\ [\cos^3 i \oint \sin^4 u\ du$$
$$-\ 3\cos i \oint \sin^2 u \cos^2 u\ du]\}\ \frac{g_{33}}{\sin i}\ ,$$

which reduce to

$$\Delta i(g_{33}) = 22.5\pi \sin^2 i \cos 3\Omega \; g_{33} , \qquad 5.17$$

and

$$\Delta\Omega(g_{33}) = 11.25\pi \sin 2i \sin 3\Omega \; g_{33} . \qquad 5.18$$

This set of equations also display equilibrium positions for i and Ω. The inclination should reach a metastable equilibrium when $i = 0°$ or $180°$ due to the $\sin^2 i$ term in the expression for Δi. The equilibrium is not stable since $\sin^2 i$ is positive on both sides of its zero point. Ω should be stable when it reaches these same values because of the $\sin 3\Omega$ factor in the expression for $\Delta\Omega$.

The corresponding expressions involving the h_{3m} terms will not be derived since their only difference from the g_{3m} terms is that each is rotated $\frac{90°}{m}$ in the ϕ direction with respect to the corresponding g term.

E. Numerical Simulations

In order to simulate the orbital evolution of a particle influenced by the solar magnetic field, the equations of motion were solved using Cowell's Method, where the particle's position and velocity were recomputed one thousand steps per orbit. Table 5.1 shows the errors in computation after 1000 orbits for a particle without charge, initially in a circular orbit at 3.5 R_0 and not undergoing P-R drag. The large error in the argument of perihelion is meaningless, since there is no perihelion in a circular orbit.

Table 5.1. Numerical errors in the computational method.

element	a (cm)	e	i (deg)	Ω (deg)	ω (deg)
error	.06	4×10^{-7}	6×10^{-14}	2×10^{-13}	184.5

It has been shown by Lamy (1976) that the semimajor axis remains nearly constant over more than 100 orbits. This is caused by a balancing of P-R drag and the sublimation effects and results in an enhancement in particle density at the outer edge of the dust-free zone surrounding the sun. We have used this balance in order to improve the speed of computation by setting the radiation pressure coefficient equal to zero, which eliminates both the P-R drag and the outward pseudo-force mentioned in the introduction. This approximation will accurately portray the behavior of the circumsolar dust when the interaction of the effects of sublimation and the magnetic field can be neglected. This is true to first order since the magnetic field does not significantly affect the particle-sun distance, which determines the sublimation rate.

The charge of the particle, q, admittedly a subject of much speculation, for purposes of this study was set at 10 volts (6.7×10^{-6} e.s.u.; cf. Consolmagno, 1980). It is standard practice to describe the charge of a dust grain in volts, since, at least for spherical particles, the grain potential is independent of the size of the particle. Since we include particles of different ascending nodes equally spaced through 360 degrees, the sign of the charge was determined to be irrelevant to the final results. This is because a decrease in the (low) initial inclinations of the test particles causes the reversal of the ascending and descending nodes and thus a particle with a negative charge will experience the same perturbations as the positively charged particle with the opposing Ω. Also, the magnitude of the charge can affect only the timescale of the variations of the orbital elements so an error in the estimate of the charge on the particle should not affect our conclusions.

In the first set of simulations, particles were initially placed in circular orbits, at an initial inclination of 2 degrees and given six different longitudes of the ascending node spaced 60 degrees apart. The orbital radius was set to be on or near the source surface, in order to simplify our understanding of the results, since the simulation program was designed to take into account the finite speed of the solar wind and thus determine the strength of the magnetic field based not on the particle's angular coordinates, but on the position where it would have had to leave the source surface in order to arrive at the particle's position.

Each such particle was then given 100 or more orbits in a magnetic field consisting of every single multipole component studied above. Thus for each g_{lm} or h_{lm}, we have 100 orbits of each of six particles starting at various values of the longitude of the ascending node. These results were then compared to the analytical results. We expect some differences in the two methods since

a. the analytical expressions assume that the non-radial component of the interplanetary field in the F corona can be ignored.

b. the integration of the expressions for Δi and $\Delta\Omega$ hold i and Ω constant over one orbit.

c. the substitution of i, Ω, and u for θ and ϕ, which was used in the derivations, does not take into account the finite travel time of the magnetic field from the source surface to the particle's position.

d. the linear step-by-step nature of the integrations used in the simulations will introduce some error into the computer results.

The results of these simulations are shown in figures 5.1 through 5.10. The first three figures are the results for the dipole terms of the solar magnetic field. Figures 5.4 through 5.6 comprise the simulation results for the g terms of the quadrupole field, and the last four sets of figures show the variations in i and Ω for the g terms of the octupole field. These computer simulations were especially useful in studying the equilibrium points of i and Ω generated by the octupole field terms. The corresponding h terms have been suppressed since there exists only a rotation equivalence between each g term and its corresponding h term.

Figure 5.1a demonstrates that the inclination did not change for any of the six (superimposed) starting values of the longitude of the ascending node when a polar dipole field was modelled. The linear form of the variations of the longitudes of the ascending nodes vs. time in figure 5.1b corresponds to the relation in equation 5.12b. Rather than calculate the rate of change of the longitude of the ascending node from equation 5.12b, we can determine it directly from figure 5.1b, as -1.1 degrees per orbit.

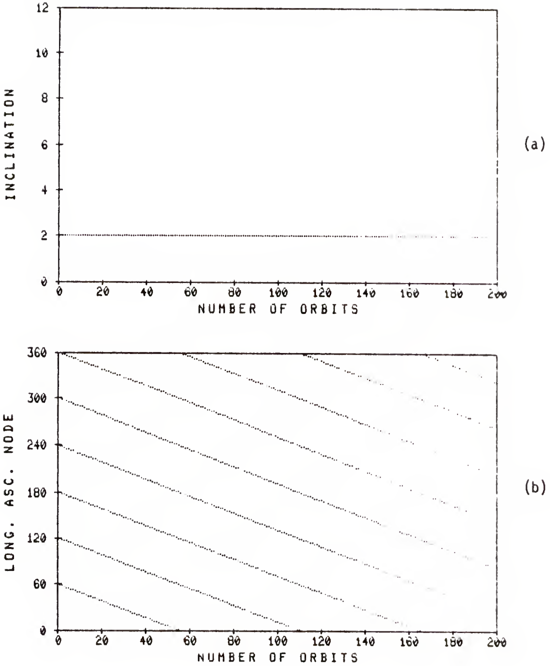

Figure 5.1. The effect of a g_{10} (polar) dipole field on a) inclinations and b) the longitudes of the ascending nodes of dust orbiting near the sun.

The inclination change due to the g_{11} component of the solar magnetic field is constant with respect to both the inclination and the longitude of the ascending node, as seen in figure 5.2a. Observe that the ascending nodes of the six particles in figure 5.2b all quickly align themselves to $\Omega = 0°$, until the inclination reaches 180° after approximately 170 orbits, at which point the ascending and descending nodes flip, and the longitude of the ascending node becomes 180°. The rate of change of inclination is then slightly less than 1° per orbit.

As has been stated above, the h_{11} components of the solar magnetic field have the same form as the corresponding g_{11} components, and the only difference in their influence is a rotation in the θ direction; hence, there will be a difference in any alignment of the ascending nodes. Figures 5.3a and 5.3b demonstrate this fact. Here the effect on inclination is the same as that for figure 5.2a, but the curves of Ω in figure 5.3b are displaced 90° from those in figure 5.2b.

Figures 5.4, 5.5, and 5.6 come as no surprise since we have already shown that the quadrupole components have no effect on the orientation of the particle's orbit. It is gratifying to have a null result in the simulations, but more importantly, these results verify that the approximations used in deriving the analytical expressions are valid.

Once again the difference between the simulations and the analytical derivations must be emphasized. The computer simulations were performed by calculating the acceleration due to the magnetic field (and the sun) at a time interval of one thousandth of an "orbital period," and, by using these accelerations, computing the new position

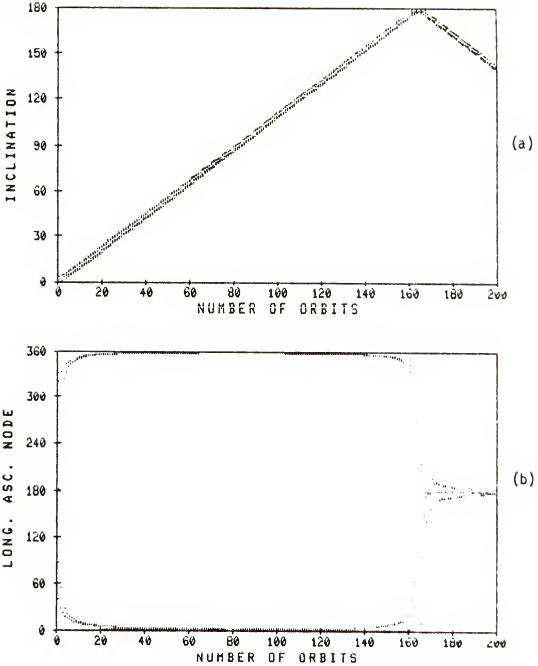

Figure 5.2. The effect of a g_{11} dipole field on a) inclinations and b) the longitudes of the ascending nodes of dust orbiting hear the sun.

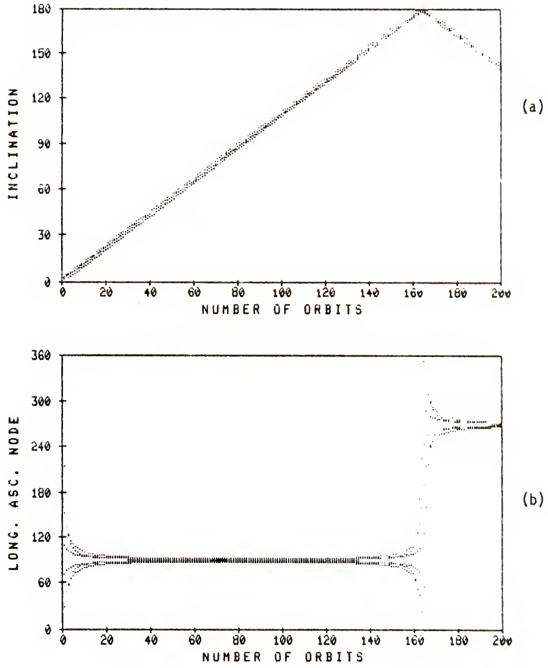

Figure 5.3. The effect of an h_{11} dipole field on a) inclinations and b) the longitudes of the ascending nodes of dust orbiting near the sun.

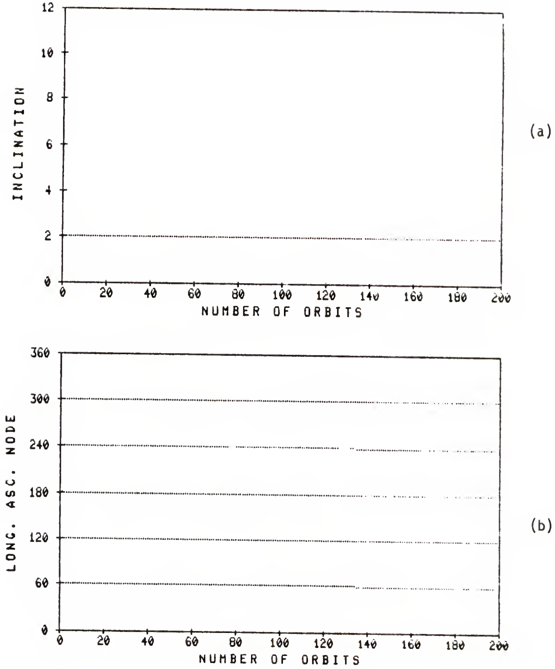

Figure 5.4. The effect of a g_{20} quadrupole field on a) inclinations and b) the longitudes of the ascending nodes of dust orbiting near the sun.

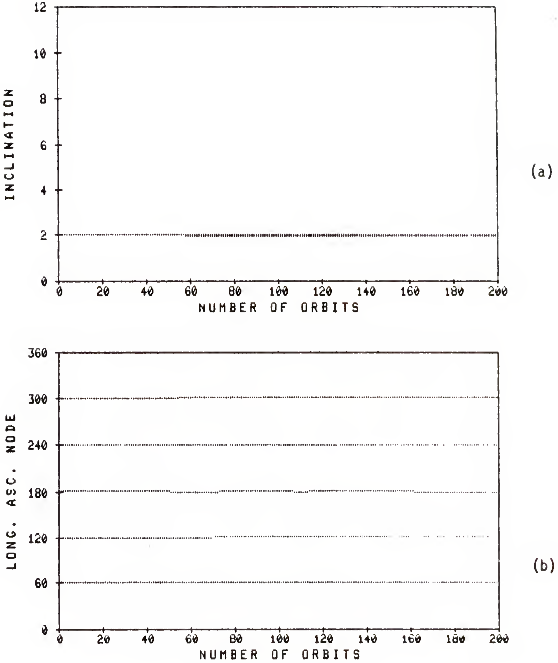

Figure 5.5. The effect of a g_{21} quadrupole field on a) inclinations and b) the longitudes of the ascending nodes of dust orbiting near the sun.

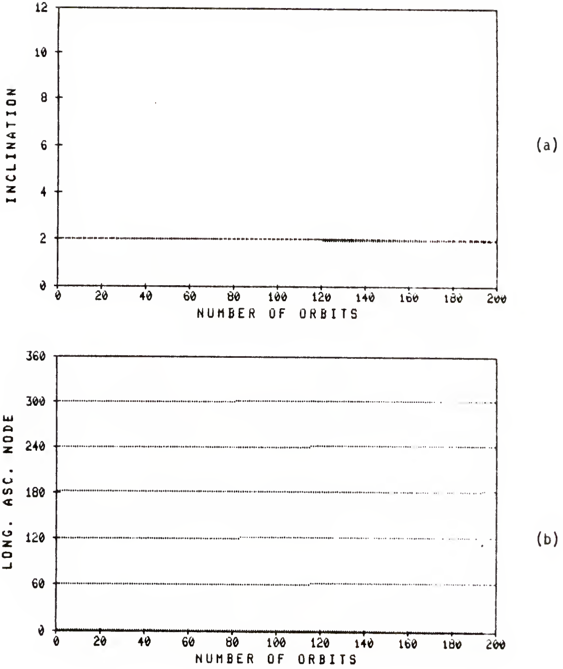

Figure 5.6. The effect of a g_{22} quadrupole field on a) inclinations and b) the longitudes of the ascending nodes of dust orbiting near the sun.

and velocity vectors of the particle at that time. This method neither uses the particle's orbital elements (except to redetermine the time interval between subsequent calculations after every printout) nor does it integrate the effects over one orbit. Indeed, the computations do not presuppose the existence of an osculating orbit, although such orbital elements are generated for the output, since x, y, z values are not useful for diagnostic purposes.

The results for the effect of the octupole field components on the orientation of orbiting dust particles are by far the most exciting. Because the octupole components are relatively weak throughout most of a solar cycle, it is not expected that these results will influence the structure of the F coronal dust cloud to a great extent. However, due to the fact that most of the expressions derived in section D indicate that each octupole term creates stable or metastable orbital alignments, it is possible that, at times of a strong octupole term, there would be a stable structure created temporarily in this region which could be observed. This suggests conversely that such an observation would confirm the presence of a relatively strong octupole field, which should be of interest to solar physicists.

Figure 5.7a demonstrates the lack of effect of the g_{30} component on the inclinations of orbiting particles. The straight line across the bottom of the graph represents the inclinations for all six of the initial values of the longitude of the ascending node. Since Ω varied with time (figure 5.7b) in all six cases, while i did not, there appears to be no relation between Δi and Ω. In fact, this result is identical with that in section D. From figure 5.7b, we can determine that the

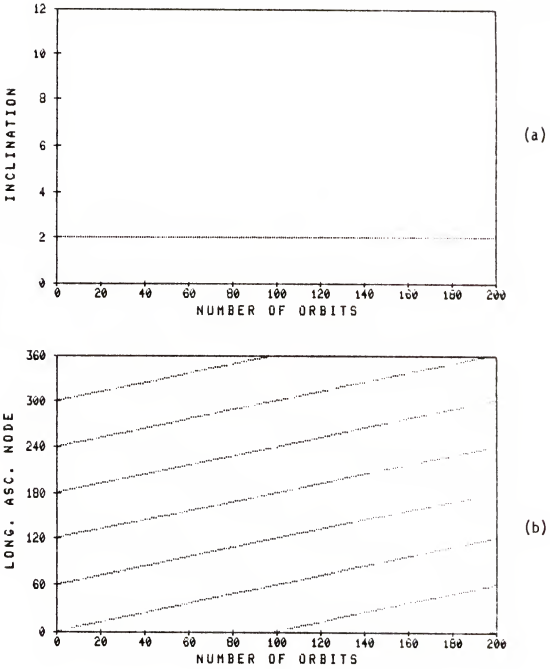

Figure 5.7. The effect of a g_{30} octupole field on a) inclinations and b) the longitudes of the ascending nodes of dust orbiting near the sun.

change in the longitude of the ascending node is about 120° for 200 orbits or 0.6° per orbit.

As described in section D, the g_{31} octupole component drives the inclination toward about 63°, which can be seen in figure 5.8a. The longitude of the ascending node quickly reaches an equilibrium value of 180° in the case of all six particles starting at differing values for Ω. The reason for the rapid change in Ω compared to i is due to the $\cot i$ term in the expression for $\Delta\Omega$, since at the beginning of these simulations the inclination is 2°, which makes $\cot i$ very large. Notice also how Ω diverges from 180° when i becomes greater than about 31°, the point where $\sin^2 i$ becomes $\frac{4}{15}$.

The stable equilibrium value for Ω due to the g_{32} term is at $2\Omega = 90°$ or $\Omega = 45°$ or 225°, as can be seen in figure 5.9b. This causes i to proceed toward 90°, where $\sin 2i$ becomes 0 (figure 5.9a). Once $\cos^2 i$ becomes less than $\frac{1}{3}$, the expression for the change in the longitude of the ascending node becomes negative, and the value of Ω diverges from the equilibrium positions.

In figures 5.10a and 5.10b, we can see the effect of the g_{33} term on the orientation of the particle's orbit. As expected, the $\sin 3\Omega$ term in the expression for $\Delta\Omega$ (equation 5.18) causes the change in Ω to become small when Ω is near an integral multiple of 60 degrees. The reason the values which give $3\Omega = 180°$ have larger variations is that the sign of $\sin 3\Omega$ drives 3Ω away from 180° and toward 0° or 360°. The variation in inclination also displays the threefold symmetry in the longitude of the ascending node, so that only two curves of i vs. time are visible. The inclination change is small due to the $\sin i$ term in

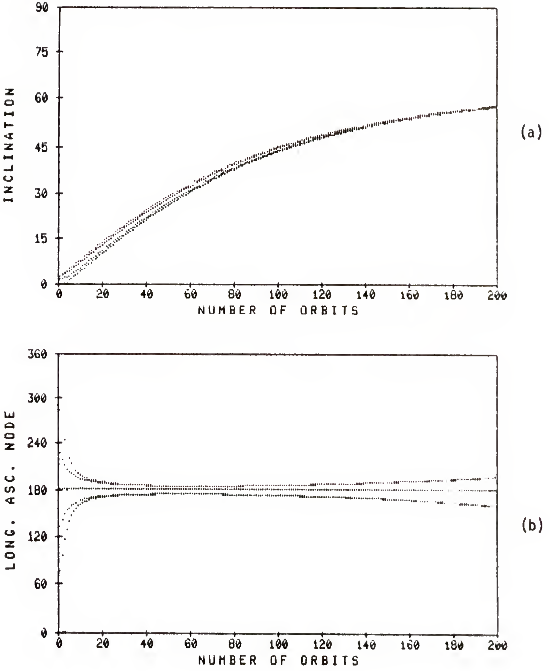

Figure 5.8. The effect of a g_{31} octupole field on a) inclinations and b) the longitudes of the ascending nodes of dust orbiting near the sun.

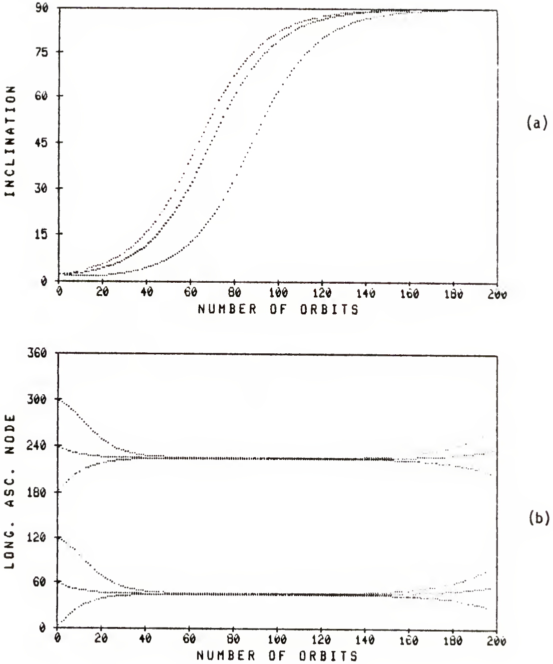

Figure 5.9. The effect of a g_{32} octupole field on a) inclinations and b) the longitudes of the ascending nodes of dust orbiting near the sun.

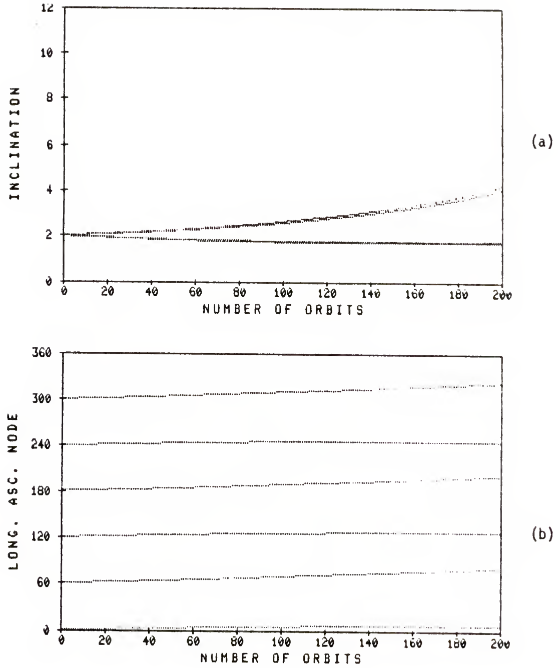

Figure 5.10. The effect of a g_{33} octupole field on a) inclinations and b) the longitudes of the ascending nodes of dust orbiting near the sun.

the numerator of the expression for i (equation 5.17). Notice also that the change in i accelerates when i becomes larger, due to the same $\sin i$ term.

A second type of simulation was run based on the observed solar magnetic field. We believe it is important to determine the effect of the solar magnetic field when the entire field structure is taken into account. This type of modelling allows any interactions between the multipole components to be observed, as well as determining what sort of structure in the solar dust cloud can be generated in the F coronal region. These results can (and will) be compared with those infrared observations of the F corona which were briefly mentioned in the introduction.

The model of the solar magnetic field used in this section is based on actual observations of the solar surface and the interplanetary magnetic field. We have used the numerical representation of the field developed by Hoeksema (1984) in which the field is generated from the various multipole components of coefficients g_{lm} and h_{lm}. These coefficients were determined from observations, with the assumption of a spherical source surface. In our calculation of the solar field, we used only terms up to and including the second order (quadruopole) coefficients. Since our particle orbits are beyond the source surface, determination of the field at any position involves calculating the field at that position on the source surface where it originated and projecting it outward, taking into account the finite velocity of the field and the effects of solar rotation.

Particles were run at initial inclinations of 2°, 5°, 10°, and 30°, and at 20 different ascending nodes from 18° to 360° inclusive. Each case was run at various starting times so that, at the date under study, particles would have been in the region from 0 to 90 orbits. Each particle thus was represented by a set of orbital elements. The x, y, z coordinates of up to twenty points (based on the fan model of Leinert, 1976, although our results are not model dependent) along each orbit were computed. These points were equally spaced in the mean anomaly with a random starting position of the first point in order to avoid particle alignments due to the choice of positions. The points were then projected onto a viewing plane and plotted. Figure 5.11 shows the initial particle positions, including all inclinations and ascending nodes, for one starting time. We made three runs at different dates to represent different configurations of the solar magnetic field. 1976.6 represents the field at sunspot minimum, where the polar dipole component strongly dominates the higher orders, 1980.6 (sunspot maximum) is a time when the dipole field is weak and the quadrupole terms dominate, and, around 1982.9, the contributions from the dipole and quadrupole components are comparable. Figures 5.12, 5.13, and 5.14 show the direction and magnitude of the field in solar equatorial coordinates, for 1976.6, 1980.6, and 1982.9, respectively. Figures 5.15, 5.16, and 5.17 show the equatorial dipole components of these fields.

Figures 5.18 and 5.19 show the structure of the solar dust cloud during sunspot minimum. The particles have spread from their initial concentrations (figure 5.11) to create a nearly homogeneous band of

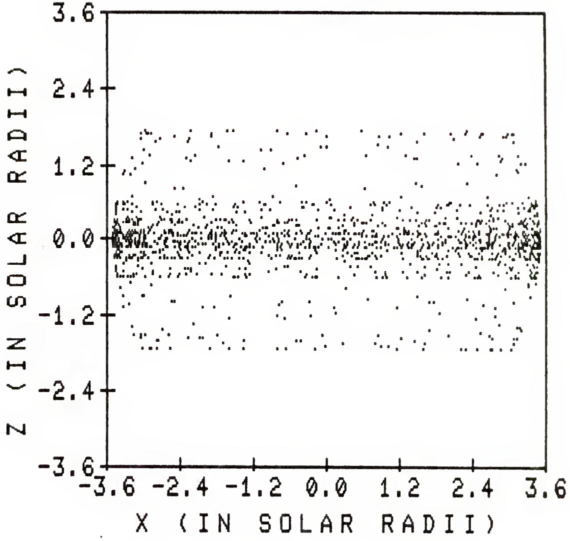

Figure 5.11. Input particle distribution for the simulations of F coronal dust distribution under the effect of a solar magnetic field.

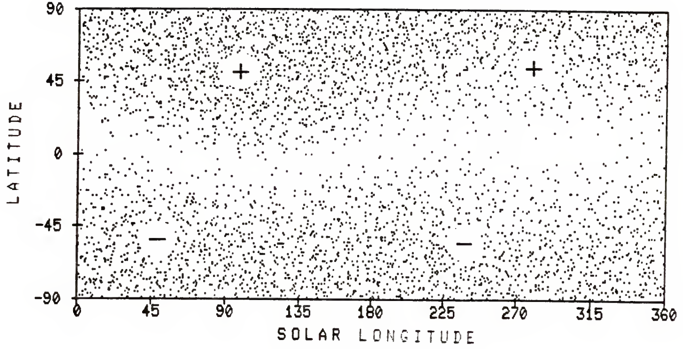

Figure 5.12. Magnetic field strength at the source surface for the date 1976.6. The field strength is proportional to the density of the points. The direction of the field is indicated by the + and - signs.

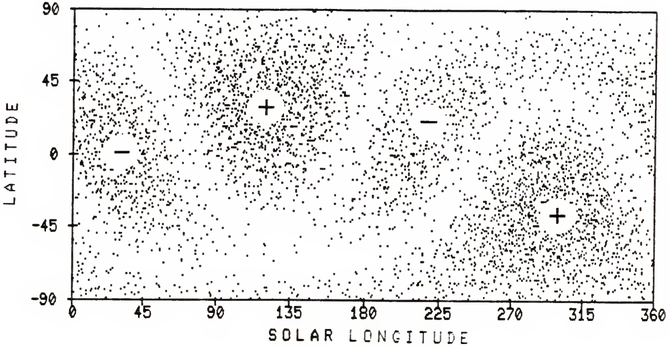

Figure 5.13. Magnetic field strength at the source surface for the date 1980.6.

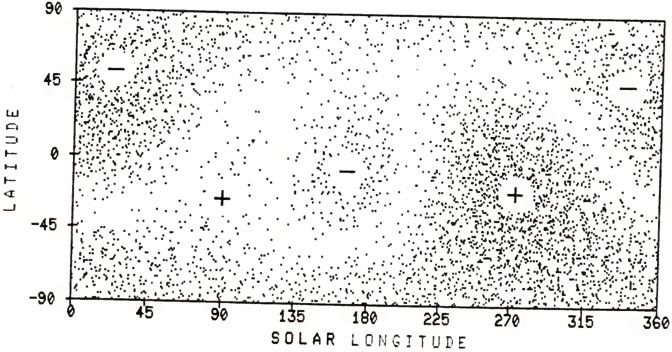

Figure 5.14. Magnetic field strength at the source surface for the date 1982.9.

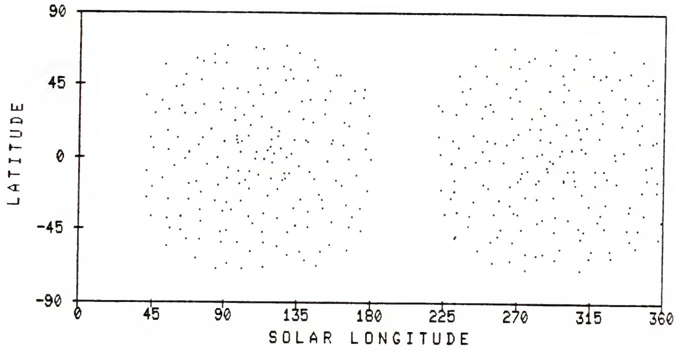

Figure 5.15. Magnetic field strength at the source surface of the Equatorial Dipole component of the field for the date 1976.6. The density scale is the same as in figures 5.12-5.17.

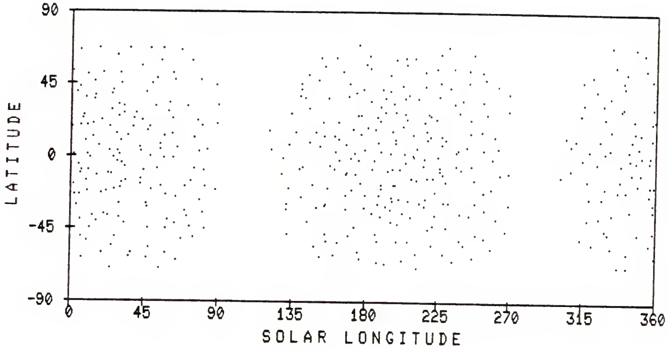

Figure 5.16. Magnetic field strength at the source surface of the Equatorial Dipole component of the field for the date 1980.6.

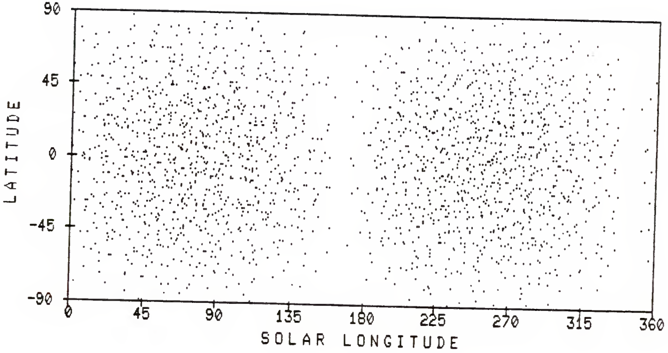

Figure 5.17. Magnetic field strength at the source surface of the Equatorial Dipole component of the field for the date 1982.9.

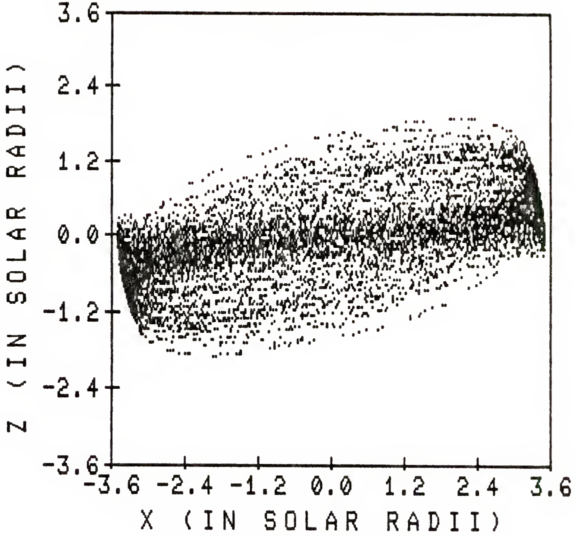

Figure 5.18. Particle distribution in the F corona for the date 1976.6, as viewed from the -y direction. The x direction is the direction of 0° solar longitude at the beginning of a Carrington Rotation. The distribution combines particles released at times from 0 to 90 orbits before 1976.6

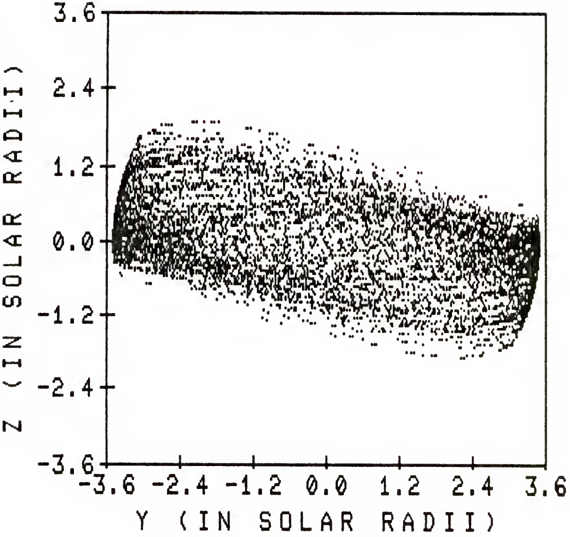

Figure 5.19. Particle distribution in the F corona for the date 1976.6, as viewed from the +x direction.

material up to 25 degrees above and below its symmetry plane, which is no longer aligned with the solar equatorial plane, with particle orbits up to 40° from the symmetry plane. Since the solar magnetic field at sunspot minimum approximates a polar dipole, this field was not expected to cause the radical increases in inclination displayed at other times.

In figures 5.20 and 5.21, the solar dust zone has been under the influence of the quadrupole dominated solar magnetic field of 1980.6. Once again, the particles have been moved from their original orbits so that the plane of symmetry is no longer the solar equatorial plane. The structure in figure 5.11 is evidence of an aligning of the lines of nodes of the particle orbits preferentially in the direction of the x-axis. Comparing this with the dipole component of the field in 1980.6 (figure 5.16), it appears, as expected, that the orbital planes have precessed about the line of the maximum dipole component.

Figures 5.22 and 5.23 demonstrate that the solar magnetic field can, at times, completely scatter the particles from the solar equatorial plane. The inclinations of the particle orbits go from 0° to 120°, where inclinations of greater than 90° apply to particles in retrograde orbits (Shcheglov et al., 1985, observed a retrograde component in their radial velocity measurements). There is no evidence of ring or band structure; the distribution of the solar dust cloud appears as a spherical shell from the direction of the x-axis and covers about $\frac{2}{3}$ of this region when viewed along the y-axis. Once again the equatorial dipole field is the dominant factor in the spread of particle inclinations, as can be seen by comparing the axis of

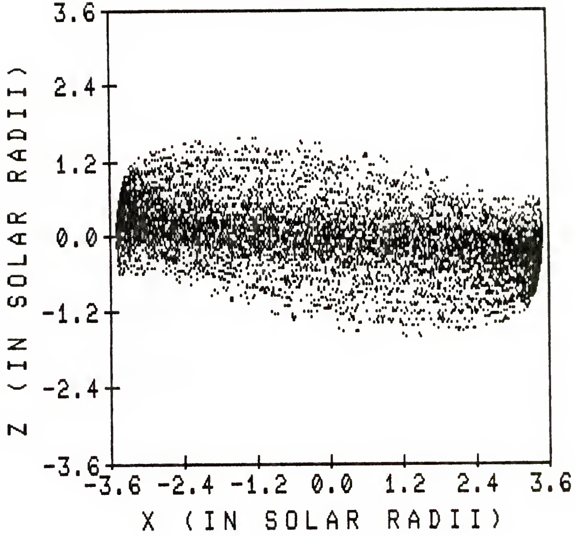

Figure 5.20. Particle distribution in the F corona for the date 1980.6, as viewed from the -y direction.

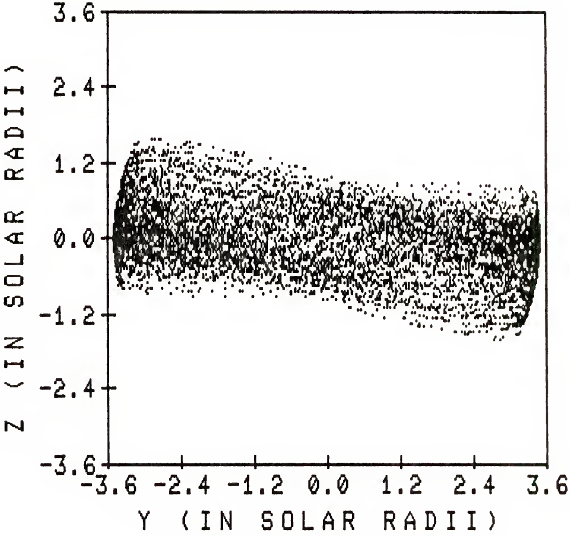

Figure 5.21. Particle distribution in the F corona for the date 1980.6, as viewed from the +x direction.

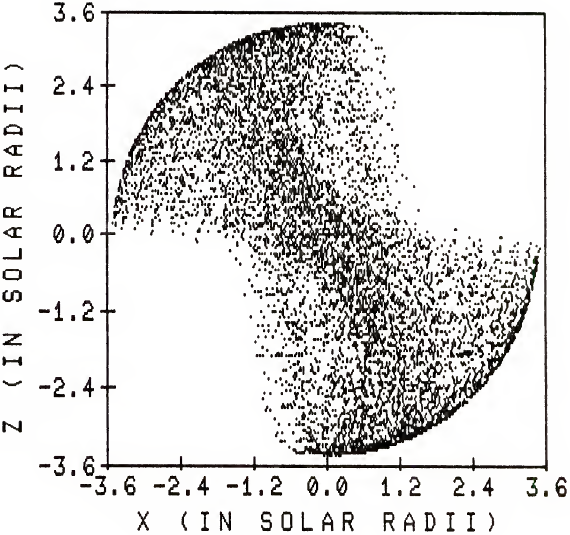

Figure 5.22. Particle distribution in the F corona for the date 1982.9, as viewed from the -y direction.

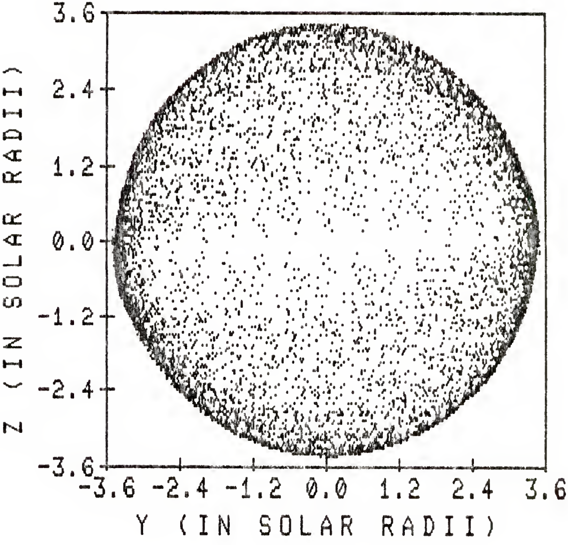

Figure 5.23. Particle distribution in the F corona for the date 1982.9, as viewed from the +x direction.

intersection of the orbital planes with the equatorial dipole field in figure 5.17. The results of Hoeksema (1984) indicate that, for the period 1976 to 1984, the equatorial dipole component was as strong or stronger than that of 1982.9 about half of the time.

Figure 5.24 and 5.25 show the distribution of just those particles with initial inclinations of 2°. The band structure of each group of particles with the same starting time remains nearly intact, but each such band has been reoriented in space. A study done on the change in the particles' orbital planes to resolve the variation in the precession axis determined that the axis did not change more than 5° in orientation over the course of ninety orbits.

F. Analysis of Observational Evidence

The observations mentioned in the introduction, which have shown an enhancement at approximately $4R_0$, are all within 30° of the ecliptic plane. Unfortunately, those observations attempted by MacQueen et al. that would have scanned perpendicular to the ecliptic were lost due to equipment failure, so that there is no solid evidence as to the maximum extent of the enhancement, although there appears to be no limit in the latitude at which the dust appears. Previous theoreticians have described the enhancement in density as a ring (Mukai, 1983). They based their belief on the observation that the interplanetary zodiacal cloud indicates a much higher dust density within 10° of the invariable plane. However, a dust ring aligned with any plane not normal to the ecliptic will appear from the Earth as an ellipse, a thin ellipse if the viewer is within a few degrees of the

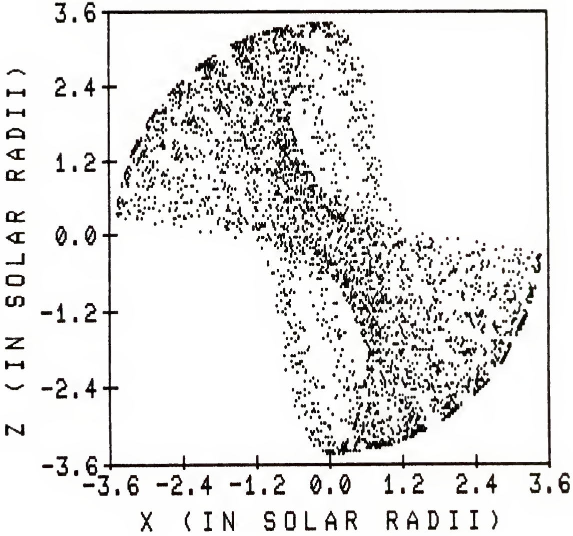

Figure 5.24. Particle distribution in the F corona for the date 1982.9, as viewed from the -y direction. Only particles with initial inclinations of 2° are included.

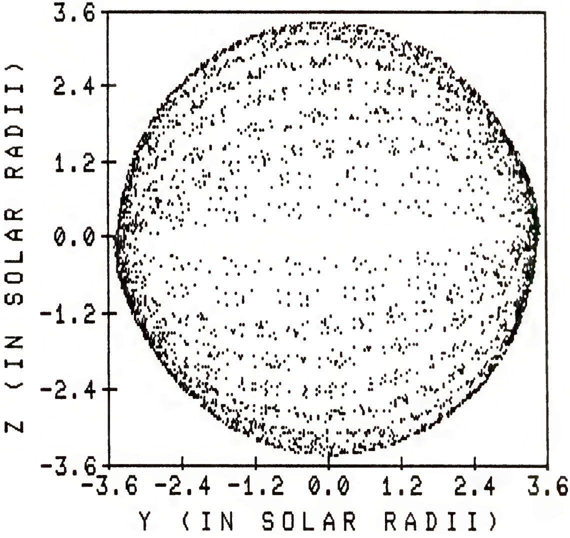

Figure 5.25. Particle distribution in the F corona for the date 1982.9, as viewed from the +x direction. Only particles with initial inclinations of 2° are included.

ring plane, for the maximum length of the minor axis of such an ellipse as viewed from Earth is .5 R_0 when the Earth is 90° or 270° from the direction of the line of nodes of the solar equatorial plane.

Table 5.2 shows a summary of the observations. Here, λ_0-Ω_0 is the angle between the Earth and the ascending node of the solar equatorial plane at the time of observation. Scan angle I is the angle between the line of observation and the ecliptic, and scan angle II (calculated by the author) is the angle between the line of observation and the solar equatorial plane, assuming spherical symmetry. While there are no observations at high solar latitudes, there is enough latitude variation in the available observations to show that there cannot be a structure in the solar dust cloud which does not cover 22° north or south of the solar equatorial plane, and this is a minimum.

Numerical simulations of the effect of the solar magnetic field on the distribution of the coronal dust particles show that the magnetic field tends to scatter particles toward the polar regions, with a significant effect arising when the equatorial dipole components become strong. According to the observational evidence (Hoeksema, 1984, p. 177), this is at least 50% of the time. Observations appear to support the conclusion that the dust cloud exists as a wide band or spherical shell surrounding the sun. Further observational studies of infrared emission in the F corona, especially at high solar latitudes, are needed to verify these conclusions.

Table 5.2. A summary of observations of the enhancement in the infrared emission at 4 R_0. Scan angles I and II are measured from the line of observation to the ecliptic plane and the solar equatorial plane, respectively. Scan angles II were calculated by this author.

Observer(s)	Date	$\lambda_0-\omega_0$	Scan Angle I	Observed Feature r/R_0	Scan Angle II
Beavers et al.	6/26/79	98°	n/a	4.3	21°
MacQueen	11/12/66	203°	0°	3.9	7°
MacQueen	1/ 9/67	146°	20°	4.2	14°
MacQueen	1/ 9/67	146°	-40°	4.2	46°
Maihara et al.	6/11/83	355°	7°	4.	14°
Peterson	9/ 3/66	272°	?	∿4.	-
Peterson	11/12/66	203°	29°	4.2	22°
Peterson	3/ 7/70	89°	var.	4.	-

CHAPTER VI

THE EFFECT OF THE SUN'S FINITE SIZE AND SOLAR ROTATION

In the region of the F corona, solar radiation reaches an orbiting particle from a wide range of directions due to the fact that the sun is not a point source. Indeed, a point just above the solar photosphere receives radiation as if the source were an infinite plane. Because both the differential source surfaces and the orbiting particle are moving with respect to the center of the sun, radiation from different directions will impinge upon the particle with different average energies. An anisotropy in the radiation field is thus created, which one must take into account when the effect of solar radiation on the dynamics of an orbiting particle is to be determined.

In 1962, Guess derived an expression for the force generated by radiation from a non-rotating spherical source using the physics of special relativity. His derivation did not utilize Robertson's 1937 expression for the radiation-induced force from a radiating point source, and in fact, Guess followed the lines of Robertson's derivation, essentially rederiving the P-R drag formula in the process. As a by-product of our derivation, we will show that his expression can be derived without using a relativistic approach. Here I also wish to note that although Robertson's formula was determined from relativistic considerations, it too can be derived classically (see Burns, Lamy, and Soter, 1979). In fact, all of the radiation pressure effects on orbiting bodies can be treated as classical forces, since the velocities in question are much much smaller than the speed of light.

The forces on a particle due to the finite size of the sun and due to solar rotation can be derived jointly, since both involve an integration of the incremental forces of radiation across the solar surface. In this section we intend to determine the radiation force from each source point by determining the relative velocity of the source and particle and apply Robertson's (1937) expression for the force due to a point source sun at each such source point.

We will set up our primary coordinate system such that the particle is on the x-axis at a distance r from the sun's center, the y-axis is perpendicular to the solar rotation axis and positive in the direction of motion of the particle's subsolar point, and the z-axis is such that x-y-z form the usual right-handed coordinate system.

Because the velocity of a point on the solar surface depends on its position with respect to the solar equatorial plane, we will need to define a solar coordinate system x_0, y_0, z_0, such that the z_0-axis is in the direction of the sun's rotation vector and the y_0-axis is parallel to the y-axis. The transformation between the x-y-z coordinates and the x_0-y_0-z_0 coordinates can be written as a function of the angle θ, the angle between the solar north pole and the x-axis. They are

$$x_0 = x \sin\theta - z \cos\theta$$

$$y_0 = y$$

$$z_0 = x \cos\theta + z \sin\theta \ .$$

If we consider a point S on the solar surface, with solar coordinates x_0, y_0, z_0, the velocity vector of that point is

$$\vec{v}_s = \omega_0(z_0) \cdot (-y_0, x_0, 0) = -\omega_0 y_0 \hat{x}_0 + \omega_0 x_0 \hat{y}_0 \ ,$$

or, in our base coordinates,

$$\vec{v}_s = -\omega_0 y \sin\theta \ \hat{x} + \omega_0 (x \sin\theta - z \cos\theta) \ \hat{y} + \omega_0 y \cos\theta \ \hat{z} \ .$$

The velocity of the particle in this system does not depend on the source position and will be denoted

$$\vec{v}_p = (\dot{x}, \dot{y}, \dot{z}) = \dot{x} \ \hat{x} + \dot{y} \ \hat{y} + \dot{z} \ \hat{z} \ .$$

The relative velocity of the particle with respect to the source point is

$$\vec{v}_p - \vec{v}_s \ .$$

For the purpose of determining the contribution of each source area, it is simplest to make another transformation to a circular disk, i.e., the apparent solar disk as viewed from the particle. This is done by projecting each source point S onto the disk (see figure 6.1) at a point S'. The point S' has coordinates denoted by X,Y,Z. From the geometry of figure 6.1, we can determine the radius of the disk R_D, and X, which is the distance from the disk to the center of the sun. The distance from the particle to the edge of the sun along a tangent (distance PQ in figure 6.1) is

$$\sqrt{r^2 - R_0^2}$$

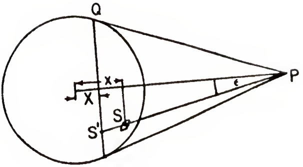

Figure 6.1. The geometry of radiation from the solar surface. P is the particle position, the source of the surface is S, and the projection of S onto the apparent solar disk is S'.

and so the radius of the disk is given by

$$R_D^2 = r^2 - R_o^2 - (r - X)^2$$

which also equals

$$R_D^2 = R_o^2 - X^2 \; .$$

This gives $X = \frac{R_o^2}{r}$, and so $R_D^2 = R_o^2(1 - \frac{R_o^2}{r^2})$.

Now, the relation between the coordinates x,y,z of S and the coordinates X,Y,Z of S' is such that, if we define an angle ε between the line PS and the x-axis,

$$\tan\varepsilon = \frac{\sqrt{y^2 + z^2}}{(r - x)} = \frac{\sqrt{Y^2 + Z^2}}{(r - X)}$$

or

$$\frac{(r - x)}{(r - X)} = \frac{\sqrt{y^2 + z^2}}{\sqrt{Y^2 + Z^2}} ,$$

and, because of rotational symmetry,

$$\frac{Y}{y} = \frac{Z}{z} = \frac{(r - X)}{(r - x)} . \tag{6.1}$$

Using the fact that $x^2 + y^2 + z^2 = R_0^{\,2}$, we can write equation 6.1 as

$$r - \sqrt{R_0^{\,2} - y^2 - z^2} = \frac{(r - X)y}{Y} . \tag{6.2}$$

Since r and X are constants, we will define $r - X \equiv \rho$. Substituting $z = \frac{yZ}{Y}$ into equation 6.2, we get

$$r - \frac{\rho y}{Y} = \sqrt{R_0^{\,2} - y^2(1 + \frac{Z^2}{Y^2})} .$$

By squaring both sides, we can solve for $\frac{y}{Y}$ using the quadratic formula. We get

$$\frac{y}{Y} = \frac{[2r\rho - \sqrt{4r^2\rho^2 - 4r\rho(\rho^2 + R^2)}]}{2(\rho^2 + R^2)} , \tag{6.3}$$

where $R^2 = X^2 + Y^2$. R is in fact the radial distance from the center of the disk to the point S', and it will be convenient in later integrations to use the transformation $Y = R \cos\phi$, and $Z = R \sin\phi$, which in no way invalidates our previous definition of R.

After defining $\rho^2 + R^2 \equiv D^2$, which equals the distance from the source point to the particle, and collecting terms, equation 6.3 becomes

$$y = \frac{Y[r\rho - \sqrt{r\rho(R_D{}^2 - R^2)}]}{D^2} .$$

We will call

$$\frac{[r\rho - \sqrt{r\rho(R_D{}^2 - R^2)}]}{D} \equiv f .$$

Remember that f and D are functions of R. The expressions for x, y, and z in terms of X, Y, and Z are

$$x = r - f\rho$$

$$y = fY$$

$$z = fZ .$$

The coordinates of the source point in our disk coordinate system are (X,Y,Z), and the coordinates of the particle are (r,0,0). The radius vector from the source to the particle is

$$\vec{r} = (r - \frac{R_o{}^2}{r},-Y,-Z) = (\rho,-Y,-Z)$$

and the relative velocity vector, in terms of the disk coordinates, is

$$\vec{v}_{rel} = (\dot{x} + \omega_o Yf\sin\theta,\ \dot{y} - \omega_o r\sin\theta + \omega_o \rho f\sin\theta + \omega_o Zf\cos\theta,$$
$$\dot{z} - \omega_o Yf\cos\theta) .$$

The radial velocity, $\dot{r}$, can be found from $\dot{r} = (\frac{\vec{r}}{D})\cdot\vec{v}_{rel}$, which gives

$$\dot{r} = \frac{1}{D}\,(\rho\dot{x} - Y\dot{y} - Z\dot{z} + \omega_o rY\sin\theta) .$$

Now, with $\vec{r}$, $\dot{r}$, and $\vec{v}$ in terms of the disk coordinates of the source point, we can substitute these values into Robertson's (1937) formula

$$\vec{F} = \frac{E_o}{D^2}\left(\hat{r} - \frac{\dot{r}\hat{r}}{c} - \frac{\vec{v}}{c}\right)$$

using E_o here as the momentum flux per unit surface area of the visible solar disk impinging on a particle of unit size. We then get

$$\begin{aligned}\frac{\vec{F}}{E_o} = {} & \hat{x}\left[\frac{\rho}{D^3} - \frac{\rho}{cD^4}(\rho\dot{x} - Y\dot{y} - Z\dot{z} + \omega_o rY\sin\theta) - \frac{\dot{x}}{cD^2}\right] \\ & + \hat{y}\left[\frac{-Y}{D^3} + \frac{Y}{cD^4}(\rho\dot{x} - Y\dot{y} - Z\dot{z} + \omega_o rY\sin\theta) - \frac{\dot{y}}{cD^2}\right] \\ & + \hat{z}\left[\frac{-Z}{D^3} + \frac{Z}{cD^4}(\rho\dot{x} - Y\dot{y} - Z\dot{z} + \omega_o rY\sin\theta) - \frac{\dot{z}}{cD^2}\right] .\end{aligned}$$

By holding ω_o constant, this expression can be integrated over the visible solar disk. ω_o does, in fact, vary with latitude, but the main contribution to the solar rotation induced perturbations of a dust particle's orbit is from the equatorial regions of the sun, where the rotation rate is nearly constant. If we substitute R and ϕ for Y and Z, we can eliminate those terms which include a functional dependence on ϕ of $\sin\phi$, $\cos\phi$, or $\sin\phi\cos\phi$, since the integral (from 0 to 2π) of these functions is zero. This leaves

$$\begin{aligned}\frac{\vec{F}}{E_o} = {} & \hat{x}\left[\frac{\rho}{D^3} - \frac{\dot{x}}{c}\left(\frac{\rho^2}{D^4} + \frac{1}{D^2}\right)\right] \\ & + \hat{y}\left[\left(\frac{R^2}{D^4}\right)\cos^2\phi\left(\frac{\omega_o r}{c}\sin\theta - \frac{\dot{y}}{c}\right) - \frac{\dot{y}}{cD^2}\right] \\ & - \hat{z}\left(\frac{\dot{z}}{c}\right)\left[\left(\frac{R^2}{D^4}\right)\sin^2\phi + \frac{1}{D^2}\right] .\end{aligned}$$

The increment of surface area on the disk as "seen" by the particle is $(\frac{\rho R}{D})d\phi dR$, where $\frac{\rho}{D}$ is the cosine of the angle between the particle-source line and the normal to the disk. Integrating then over the entire disk, we get, for the directions x, y, and z,

$$F_x = \pi E_o \{\frac{R_o^2}{r^2} - \frac{2\dot{x}}{c}[\frac{4}{3} - \frac{1}{3}(1 - \frac{R_o^2}{r^2})^{3/2} - (1 - \frac{R_o^2}{r^2})^{1/2}]\} , \qquad 6.4a$$

$$F_y = \pi E_o \{\frac{-\dot{y}}{c}[\frac{8}{3} - 3(1 - \frac{R_o^2}{r^2})^{1/2} + \frac{1}{3}(1 - \frac{R_o^2}{r^2})^{3/2}] + \frac{\omega_o r}{c\sin\theta}[\frac{2}{3} - (1 - \frac{R_o^2}{r^2})^{1/2} + \frac{1}{3}(1 - \frac{R_o^2}{r^2})^{3/2}]\} , \qquad 6.4b$$

$$F_z = \pi E_o \{\frac{-\dot{z}}{c}[\frac{8}{3} - 3(1 - \frac{R_o^2}{r^2})^{1/2} + \frac{1}{3}(1 - \frac{R_o^2}{r^2})^{3/2}]\} , \qquad 6.4c$$

respectively. These expressions can best be understood by expanding them in terms of $\frac{R_o}{r}$. These then become

$$F_x = \pi R_o^2 \frac{E_o}{r^2} \{1 - \frac{2\dot{x}}{c} [1 + \frac{1}{24} \frac{R_o^4}{r^4} + \frac{1}{32} \frac{R_o^6}{r^6} + \ldots]\} , \tag*{6.5a}$$

$$F_y = \pi R_o^2 \frac{E_o}{r^2} \{\frac{-\dot{y}}{c} [1 + \frac{1}{2} \frac{R_o^2}{r^2} + \frac{5}{24} \frac{R_o^4}{r^4} + \frac{1}{32} \frac{R_o^6}{r^6}] + \frac{1}{4} (\frac{\omega_o R_o}{c})(\frac{R_o}{r}) \sin\theta \ [1 + \frac{1}{3} \frac{R_o^2}{r^2} + \frac{3}{16} \frac{R_o^4}{r^4} + \frac{1}{8} \frac{R_o^6}{r^6}]\} , \tag*{6.5b}$$

$$F_z = \pi R_o^2 \frac{E_o}{r^2} \{\frac{-\dot{z}}{c} [1 + \frac{1}{2} \frac{R_o^2}{r^2} + \frac{5}{24} \frac{R_o^4}{r^4} + \frac{1}{32} \frac{R_o^6}{r^6}]\} . \tag*{6.5c}$$

The expression πR_o^2 in equations 6.5a, b, and c is the area of the visible solar disk when viewed from a large distance, so $\pi c R_o^2 E_o$ is the total energy emitted from a solar hemisphere at unit distance impinging on a particle of unit size. If the solar rotation is neglected, the expressions in the y and z directions become equivalent and equal to the result of Guess (1962). The ratio of the force due to solar rotation to that of P-R drag at large distances from the sun is

$$\frac{F_{sr}}{F_{pr}} = \frac{1}{4} (\frac{\omega_o R_o^2}{r}) \frac{\sin\theta}{\sqrt{\dot{y}^2 + \dot{z}^2}} .$$

If we enter the values for ω_0 and R_0, and assume the particle is orbiting in the solar equatorial plane, so that $\sin\theta = 1$ and $z = \dot{z} = 0$, we can derive the ratio at several different distances from the sun. This result has been tabulated in table 6.1.

Table 6.1. The ratio of the force due to solar rotation compared to the P-R drag for many values of the particle's orbital radius.

Radius	$\frac{F_{sr}}{F_{pr}}$	Radius	$\frac{F_{sr}}{F_{pr}}$
10.0000 AU	0.0000257	0.1000 AU	0.0002574
8.0000 AU	0.0000288	16.0000 R_0	0.0002982
6.0000 AU	0.0000332	12.0000 R_0	0.0003442
4.0000 AU	0.0000407	10.0000 R_0	0.0003769
2.0000 AU	0.0000576	8.0000 R_0	0.0004210
1.0000 AU	0.0000814	6.0000 R_0	0.0004851
0.8000 AU	0.0000910	4.0000 R_0	0.0005908
0.6000 AU	0.0001051	3.5000 R_0	0.0006297
0.4000 AU	0.0001287	3.0000 R_0	0.0006771
0.2000 AU	0.0001821	1.0000 R_0	0.0011294

Notice that the ratio decreases as the distance from the sun increases and is never large, even very close to the sun. In the F corona, although the ratio is small, the P-R force is balanced by the sublimation effect and the force due to solar rotation is not overpowered. This is true only in the direction perpendicular to the orbital plane of the particle, since the coplanar component of the force due to solar rotation also becomes part of the P-R, sublimation balance. The perpendicular component of the solar rotation force affects the inclination and the longitude of the ascending node of orbiting particles. We can find the magnitude of the acceleration from this component by taking the dot product of the force vector due to solar rotation with the unit vector in the direction of the particle's orbital angular momentum and dividing by the mass of the particle, m_g. In the solar equatorial coordinate system, and using the approximation that $\frac{R_o}{r}$ is small ($\frac{1}{4}$ at the evaporation zone), this gives

$$W_{sr} = \frac{-F_{sr} \sin i \cos u}{m_g} , \qquad 6.6$$

where

$$F_{sr} = (\pi R_o^2 \frac{E_o}{r^2}) (\frac{\omega_o R_o}{c}) (\frac{R_o}{4r}) \sin\theta . \qquad 6.7$$

From Appendix A, equation A.16, the expression for $\frac{di}{dt}$, is

$$\frac{di}{dt} = W r \frac{\cos u}{n a^2 (1 - e^2)^{1/2}} ,$$

or, when we assume a circular orbit where $e = 0$, $r = a$, and $du = (\frac{2\pi}{P}) dt$, we can substitute for W from equation 6.6 to get

$$di = - F_{sr} \sin i (\frac{r^2}{GM_o' m_g}) \cos^2 u \, du . \qquad 6.8$$

Substituting the expression for F_{sr} (equation 6.7) into equation 6.8, we get an expression for di,

$$di = -\frac{1}{4}\left[\frac{\pi R_0^2}{GM_0(1-\beta)}\right]\left(\frac{\omega_0 R_0}{c}\right)\left(\frac{E_0}{m_g}\right)\left(\frac{R_0}{r}\right)$$

$$\times \sin\theta \sin i \cos^2 u \, du \; . \qquad 6.9$$

Since i will be nearly constant over one orbit, we can integrate equation 6.9 by holding $\sin i$ constant. Also, for $\sin\theta$ we must substitute in terms of u and i. The change in inclination after one orbit is then

$$\Delta i = -\Delta i_0 \oint \cos^2 u \sqrt{1 - \sin^2 i \sin^2 u}\, du \; ,$$

where

$$\Delta i_0 = \frac{3}{16}\left[\frac{\pi R_0^2}{GM_0(1-\beta)}\right]\left(\frac{\omega_0 R_0}{c}\right)\left(\frac{F_0}{sd}\right)\left(\frac{R_0}{r}\right) \; , \qquad 6.10$$

s being the radius of the particle and d its density. Also, F_0 is the energy flux of solar radiation at the sun's surface, so that

$$E_0 = \pi \frac{s^2 F_0}{c} \; .$$

Now the integral in u is not immediately solvable, but, by expanding the term under the square root into a power series and integrating, we arrive at

$$\Delta i = -\pi \, \Delta i_0 \left(1 - \frac{1}{8}\sin^2 i + \frac{1}{64}\sin^4 i - \ldots\right) .$$

Here we can ignore all but the first term unless i is nearly 90° (even then, our approximation will be accurate to within 12%). The value for Δi_0 can be found by substituting the appropriate values for the constants in equation 6.10. Notice that due to the minus sign *THIS EFFECT ALWAYS DECREASES THE INCLINATION.* For example, the decrease in inclination over one orbit, for $s = 1$ μm, $d = 1 \frac{g}{cm^3}$, and $\sin i = \frac{1}{4}$ is 0.28 seconds of arc per orbit, or about $\frac{1}{2}$ minute of arc for the 100 orbits a particle is expected to survive at the edge of the evaporation zone. Obviously, this mechanism cannot significantly affect the inclination of dust particles once they reach the F corona.

We can compare the acceleration on the particle due to solar rotation with the acceleration on a particle near the sun due to the strongest perturber, Jupiter (see Chapter IV, table 4.3). The ratio of these accelerations, at the F corona, is

$$\frac{a_{sr}}{a_J} = \frac{\sin i}{8sd} ,$$

with d in grams/cm^3 and s in microns. A glance at table 4.1 shows that this effect is even less than that of the planets. This effect could not create a density enhancement of the coronal dust in the solar equatorial plane. This result supports our conclusion in the analysis of the observations, performed in Chapter V, that no such enhancement has been discovered or could be created by any dynamical mechanism in the F corona.

CHAPTER VII

CONCLUSION

The F corona is a region of rapidly varying characteristics in which interplanetary dust is subjected to numerous dynamical forces. We have attempted to clarify the effect of some of these forces on the orbital evolution of F coronal dust, using both theory and numerical simulations.

In Chapter II we discovered how interplanetary dust distribution depends on solar distance through interactions with the inner planets. Chapter III extended the distribution of interplanetary dust into the F corona as a basis for the initial conditions of subsequent simulations. In Chapter IV we derived a method for determining the relative extent of each planet's zone of influence when perturbations on the orbits of particles are to be determined and used this to show that the effect of planetary perturbations on circumsolar dust is negligible. Chapter V was an in-depth study of the effect of the solar magnetic field on the orbital elements of dust in the F corona. Here, we have also correlated observations of the F corona by previous authors with our findings. Finally in Chapter VI we developed an expression for the radiation pressure force of a rotating spherical source.

Among our findings are the following:

1. Planetary perturbations increase the eccentricity of dust particle orbits and decrease the P-R lifetime of the particles.

The orbits of particles which do not experience close encounters with the planet Jupiter are, on the average, slowly reduced in inclination.

2. There is a strong tendency of the particles to align their perihelia. The preferred direction is toward $\tilde{\omega} = 20°$.
3. Particles enter the F corona in nearly circular orbits. Although they tend toward low inclinations due to planetary perturbations, there is still a large spread in inclination as they reach the F corona. We found no preferred direction for the longitudes of the ascending nodes of these particles.
4. Planetary perturbations upon F coronal particles' orbits are not a significant source of variation in the orbital elements. The planet Jupiter is the strongest perturber in the F corona.
5. Interaction with the solar magnetic field does not affect the semimajor axis or eccentricity of dust in the F corona. It will increase the inclinations of orbiting dust during those times when the equatorial dipole component is strong. This effect generates a preferential direction along the dipole axis in the line of nodes of the orbiting dust.
6. The quadrupole components of the solar magnetic field have no effect on the orbital elements of circumsolar dust.
7. Octupole components of the solar magnetic field can create equilibrium positions in the inclinations and the longitudes of the ascending nodes of dust particle orbits. The most stable of these is an inclination of 63° from the g_{31} and h_{31} terms. Only the g_{32} and h_{32} octupole terms of the solar magnetic field

can cause an alignment of the interplanetary dust in the solar equatorial plane, and this effect is not expected to play a significant role in generating features in the solar dust cloud, since the magnitudes of the octupole components rarely exceed that of the equatorial dipole.

8. The effect of solar rotation generates a secular decrease in the inclination of F coronal dust, but this change is very small and can not align the dust into a ring structure.
9. Observations of the F corona imply that the solar dust cloud extends to at least 20° above and below the solar equatorial plane. The authors who contend that the structure is a thin ring have yet to suggest a mechanism for aligning the particle inclinations into a single plane.

CHAPTER VIII

SUGGESTIONS FOR FUTURE RESEARCH

Further study of the dynamical mechanisms of the F corona may lead to a final resolution of the question of the shape of the solar dust cloud. Other effects to study include the following:

1. Alignment of particle orbits due to collisions which may explain the reduction of inclinations. Collisions also play an important role in the ultimate lifetime of particles in the F corona. The lack of knowledge of the exact nature of these particles makes a meaningful study of collision processes difficult at the present time.
2. The effect of sputtering on the balance between P-R drag and the sublimation effect. While small radial and tangential forces such as those due to the magnetic field become absorbed in this balance, forces due to sputtering can dominate the other mechanisms as the particle passes through high speed streams.
3. Coulomb drag due to interaction between a charged dust grain and the solar wind. Like the previous mechanism, this force depends on the solar wind parameters which are not yet well understood in this region.
4. Anisotropies in radiation pressure, P-R drag, and sputtering due to particle rotation or surface irregularities. A study of the

effects of radiation pressure on cylindrical particles (Voshchinnikov and Il'in, 1983) concluded that the force due to the non-spherical nature of the particles was greater than P-R drag. A similar result is obtained from the Yarkovsky effect (the anisotropic re-radiation of a rotating particle; Radzievskii, 1952). These mechanisms are significant even outside the F corona.

The ultimate answer to understanding the dynamics of dust particles in the F corona requires long period observations of the region to determine how changes in the structure of the solar dust cloud relate to the characteristics of the solar environment.

REFERENCES

Bandermann, L.W., 1968, Physical Properties and Dynamics of Interplanetary Dust, Ph.D. thesis, University of Maryland.

Beavers, W.I., J.J. Eitter, P.H. Carr, and B.C. Cook, 1980, Radial Velocity Measurements in the F Corona, *Ap. J.*, 238, 349-356.

Brownlee, D.E., L. Pilachowski, E. Olszewski, and P.W. Hodge, 1980, Analysis of Interplanetary Dust Collections, *I.A.U. Symp. No.* 90: *Solid Particles in the Solar System* (I. Halliday and B. McIntosh, Eds.), D. Reidel, Dordrecht, Netherlands, 333-342.

Burke, J.R., and J. Silk, 1974, Dust Grains in a Hot Gas. I. Basic Physics, *Ap. J.*, 190, 1-10.

Burns, J.A., Ph.L. Lamy, and S. Soter, 1979, Radiation Forces on Small Particles in the Solar System, *Icarus*, 40, 1-48.

Consolmagno, G.J., 1980, Influence of the Interplanetary Magnetic Field on Cometary and Primordial Dust Orbits: Applications of Lorentz Scattering, *Icarus*, 43, 203-214.

East, I.R., and N.K. Reay, 1984, The Motion of Interplanetary Dust Particles. I. Radial Velocity Measurements on Faunhofer Line Profiles in the Zodiacal Light Spectrum, *Astron. Astrophys.*, 139, 512-516.

Giese, R.H., and E. Grün, 1976, The Compatability of Recent Micrometeoroid Flux Curves with Observations and Models of the Zodiacal Light, *Lecture Notes in Physics*, 48, 135-139.

Greenberg, J.M., and B.Å.S. Gustafson, 1981, A Comet Fragment Model for Zodiacal Light Particles, *Astron. Astrophys.*, 93, 35-42.

Grün, E., H.A. Zook, H. Fechtig, and R.H. Giese, 1985, Collisional Balance of the Meteoric Complex, *Icarus*, 62, 244-272.

Guess, A.W., 1962, Poynting-Robertson Effect for a Spherical Source of Radiation, *Ap. J.*, 135, 855-866.

Gustafson, B.Å.S., 1985, Planetary Perturbations: Effects on the Shape of a Cloud of Dust in Circular Heliocentric Orbit, *I.A.U. Coll. No.* 85, *Properties and Interactions of Interplanetary Dust* (R.H. Giese, Ph.L. Lamy, Eds.), D. Reidel, Dordrecht, 385-388.

Gustafson, B.Å.S., and N.Y. Misconi, 1979, Streaming of Interstellar Grains in the Solar System, *Nature*, 282, 276-278.

Hoeksema, J.T., 1984, Structure and Evolution of the Large Scale Solar and Heliospheric Magnetic Fields, Ph.D. thesis, Stanford University.

Lamy, Ph.L., 1974, The Dynamics of Circum-Solar Dust Grains, *Astron. Astrophys.*, 33, 191-194.

Lamy, Ph.L., 1976, Orbital Evolution of Circum-Solar Dust Grains, *Interplanetary Dust and Zodiacal Light* (H. Elsasser and H. Fechtig, Eds.), Springer-Verlag, Berlin, 473.

Leinert, C., H. Link, E. Pitz, and R.H. Giese, 1976, Interpretation of a Rocket Photometry of the Inner Zodiacal Light, *Astron. Astrophys.*, 47, 221-230.

Leinert, C., I. Richter, E. Pitz, and B. Planck, 1981, The Zodiacal Light from 1.0 to 0.3 A.U. as Observed by the Helios Space Probes, *Astron. Astrophys.*, 103, 177-188.

LeSargent, L.B., and Ph.L. Lamy, 1978, Interplanetary Dust: Are There Two Independent Populations? *Nature*, 276, 800-802.

MacQueen, R.M., 1968, Infrared Observations of the Outer Solar Corona, *Ap. J.*, 154, 1059-1076.

Maihara, T., K. Mizutani, H. Hiromoto, H. Takami, and H. Hasegawa, 1985, A Balloon Observation of the Thermal Radiation from the Circumsolar Dust Ring in the 1983 Total Eclipse, *I.A.U. Coll. No.* 85, *Properties and Interactions of Interplanetary Dust* (R.H. Giese, and Ph.L. Lamy, Eds.), D. Reidel, Dordrecht, 55-58.

Millet, J., J.P.L. Lafon, and Ph.L. Lamy, 1980, On the Electrostatic Potential of Interplanetary Grains: Influence of the Thermoionic Effect, *Astron. Astrophys.*, 92, 6-12.

Misconi, N.Y., 1975, Solar Flare Effects on the Zodiacal Light, Ph.D. thesis, State University of New York at Albany.

Moulton, F.R., 1914, *An Introduction to Celestial Mechanics*, The MacMillan Company, New York, 404.

Mukai, T., 1981. On the Charge Distribution of Interplanetary Grains, *Astron. Astrophys.*, 99, 1-6.

Mukai, T., 1983, Mass Loss Rate of the Zodiacal Dust Cloud, *The Moon and the Planets*, 28, 305-309.

Mukai, T., S. Mukai, G.H. Schwehm, and R.H. Giese, 1983, Supply of Interplanetary Grains from Comets, *The Proceedings of the International Conference on Cometary Exploration* (T.I. Gombosi, Ed.), Central Research Institute for Physics, Hungarian Academy of Sciences, Budapest, 135-142.

Mukai, T., and T. Yamamoto, 1979, A Model of the Circumsolar Dust Cloud, *Publ. Astron. Soc. Japan*, 31, 585-595.

Muaki, T., T. Yamamoto, H. Hasegawa, A. Fujiwara, and C. Koike, 1974, On the Circumsolar Grain Materials, *Publ. Astron. Soc. Japan*, 26, 445-458.

Öpik, E.J., 1951, Collision Probabilities with the Planets and the Distribution of Interplanetary Matter, *Proc. Royal Irish Acad.*, 54, 165-199.

Paddack, S.J., and J.W. Rhee, 1975, Rotational Bursting of Interplanetary Dust Particles, *Geophys. Res. Letters*, 2, 364-367.

Pailer, N., and E. Grün, 1980, Determination of Particle Densities by Penetration Studies, *I.A.U. Symp. No.* 90: *Solid Particles in the Solar System* (I. Halliday and B. McIntosh, Eds.), D. Reidel, Dordrecht, 365-370.

Parker, E.N., 1963, *Interplanetary Dynamical Processes*, John Wiley & Sons, Inc., New York.

Peterson, A.W., 1967, Experimental Detection of Thermal Radiation from Interplanetary Dust, *Ap. J. Letters*, 148, L37-L39.

Peterson, A.W., 1969, The Coronal Brightness at 2.23 Microns, *Ap. J.*, 155, 1009-1015.

Peterson, A.W., 1971, A Determination of the Vaporization Temperature of Circumsolar Dust at 4 R_0, paper presented at *AAS Meeting* #135, Amherst, Mass., Aug. 24-27.

Poynting, H.J., 1903, Radiation in the Solar System: Its Effect on Temperature and Its Pressure on Small Bodies, *Phil. Trans. Roy. Soc. A*, 202, 525.

Radzievskii, V.V., 1952, On the Influence of an Anisotropic Re-emission of Solar Radiation on the Orbital Motion of Asteroids and Comets, *Astron. Zh.*, 29, U.S. Dept. of Commerce translation 62-10653, 162-170.

Radzievskii, V.V., 1954, A Mechanism of the Disintegration of Asteroids and Meteoroids, *Dolk. Akad. Nauk. SSSR*, 97, 49-52.

Robertson, H.P., 1937, Dynamical Effects of Radiation in the Solar System, *Monthly Notices Roy. Astron. Soc.*, 97, 423.

Schuerman, D.W., 1980, The Restricted Three-Body Problem Including Radiation Pressure, *Ap. J.*, 238, 337-342.

Schulz, M., E.N. Frazier, and D.J. Bonchon, Jr., 1978, Coronal Magnetic Field Model with Non-Spherical Source Surface, *Solar Phys.*, 60, 83.

Shcheglov, P.V., L.I. Shestakova, and A.K. Ajmanov, 1985, Interferometric Observations of F-Corona Radial Velocity Field at the Distances (3-7) R/R, *I.A.U. Coll. No.* 85, *Properties and Interactions of Interplanetary Dust* (R.H. Giese and Ph.L. Lamy, Eds.), D. Reidel, Dordrecht, 77-80.

Tisserand, F., 1889, *Traite de Mechanique Celeste*, Gauthier-Villars et Fils, Paris.

Voshchinnikov, N.V., and V.B. Il'in, 1983, Radiation Pressure on Aspherical Grains, Compared with the Poynting-Robertson Effect, *Pis'ma Astron. Zh.*, 9, 188-192, translated in *Sov. Astron. Letters*, 9, 101-103.

Whipple, F.L., 1940, Photographic Meteor Studies. III. The Taurid Shower, *Proceedings of the American Philosophical Society*, 83, 711-745.

Wyatt, S.P., and F.L. Whipple, 1950, The Poynting-Robertson Effect on Meteor Orbits, *Ap. J.*, 111, 134-141.

APPENDIX A

MATHEMATICAL RELATIONS

I. TRIGONOMETRIC INTEGRALS

A. FIRST ORDER INTEGRALS

$$\oint \sin u \, du = \oint \cos u \, du = 0$$

B. SECOND ORDER INTEGRALS

$$\oint \sin^2 u \, du = \oint \cos^2 u \, du = \pi$$

$$\oint \sin u \cos u \, du = 0$$

C. THIRD ORDER INTEGRALS

$$\oint \sin^3 u \, du = \oint \cos^3 u \, du = 0$$

$$\oint \sin^2 u \cos u \, du = \oint \cos^2 u \sin u \, du = 0$$

D. FOURTH ORDER INTEGRALS

$$\oint \sin^4 u \, du = \oint \cos^4 u \, du = \frac{3\pi}{4}$$

$$\oint \sin^3 u \cos u \, du = \oint \cos^3 u \sin u \, du = 0$$

$$\oint \sin^2 u \cos^2 u \, du = \frac{\pi}{4}$$

II. LEGENDRE POLYNOMIALS

$P_0^0 = 1$

$P_1^0 = \cos\theta \qquad P_1^1 = \sin\theta$

$P_2^0 = \frac{1}{2}(3\cos^2\theta - 1) \qquad P_2^1 = -3\sin\theta\cos\theta \qquad P_2^2 = 3\sin^2\theta$

$P_3^0 = \frac{1}{2}\cos\theta(5\cos^2\theta - 3) \qquad P_3^1 = \frac{3}{2}\sin\theta(1 - 5\cos^2\theta) \qquad P_3^2 = 15\sin^2\theta\cos\theta$

$P_3^3 = -15\sin^3\theta$ A.9

$P_l^m = (-1)^m P_{lm}$ A.10

$P_l^0 = P_l$ A.11

$$P_l^m(\cos\theta) = (-1)^m \sin^m\theta \frac{d^m P_l(\cos\theta)}{d(\cos\theta)^m} \tag{A.12}$$

III. COORDINATE TRANSFORMATIONS

Note: The angle θ is the polar angle, the angle ϕ is the azimuthal angle as measured from the x-axis.

$x = \sin\theta\cos\phi = \cos\Omega \cos u - \sin\Omega \sin u \cos i$

$y = \sin\theta\sin\phi = \sin\Omega \cos u - \cos\Omega \sin u \cos i$

$z = \cos\theta = \sin u \sin i$ A.13

IV. GAUSSIAN PERTURBATION EQUATIONS

$$\frac{da}{dt} = \frac{Se \sin f + T(1 + e \cos f)}{n(1-e^2)^{1/2}} \tag{A.14}$$

$$\frac{de}{dt} = \frac{S\ \sin f + T(\cos E + \cos f)}{na(1-e^2)^{-1/2}} \qquad \text{A.15}$$

$$\frac{di}{dt} = \frac{Wr\cos u}{na^2(1-e^2)^{1/2}} \qquad \text{A.16}$$

$$\frac{d\omega}{dt} = \frac{r}{na^2e(1-e^2)^{1/2}}\left[-S\ \cos f(1+e\ \cos f) + T\ \sin f(2+e\ \cos f)\right] - \cos i\ \frac{d\Omega}{dt} \qquad \text{A.17}$$

$$\frac{d\Omega}{dt} = \frac{Wr\ \sin u}{na^2(1-e^2)^{1/2}\sin i} \qquad \text{A.18}$$

$$\frac{d\varepsilon}{dt} = \frac{-2rS}{na^2} - (1 - e^2)^{1/2}\ \cos i\ \frac{d\Omega}{dt} + \frac{e^2}{1 + (1 - e^2)^{1/2}}\ \frac{d\tilde{\omega}}{dt} \qquad \text{A.19}$$

APPENDIX B

GRAPHIC DATA OF PARTICLE SIMULATIONS

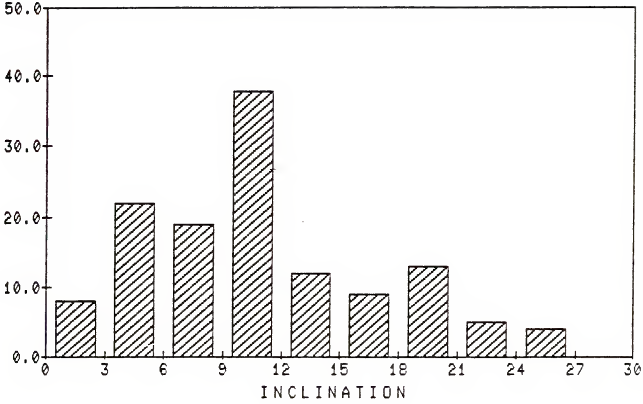

Figure B.1. Number density vs. inclination at 0.35 A.U.

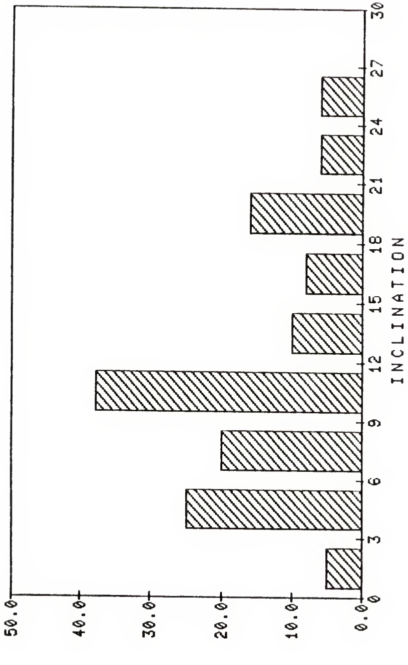

Figure B.2. Number density vs. inclination at 0.45 A.U.

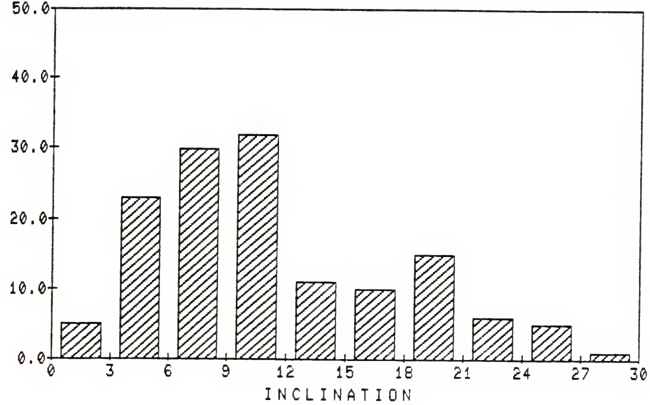

Figure B.3. Number density vs. inclination at 0.55 A.U.

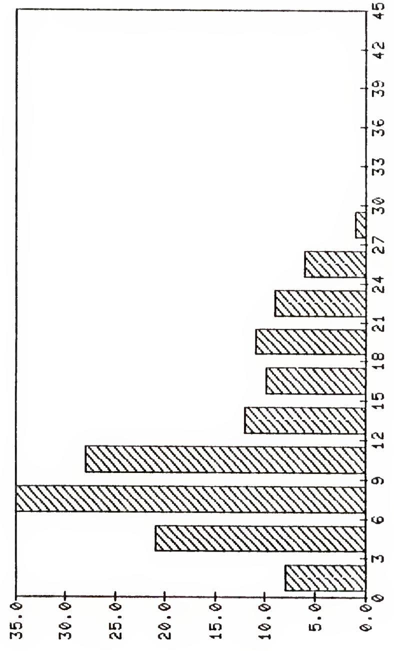

Figure B.4. Number density vs. inclination at 0.65 A.U.

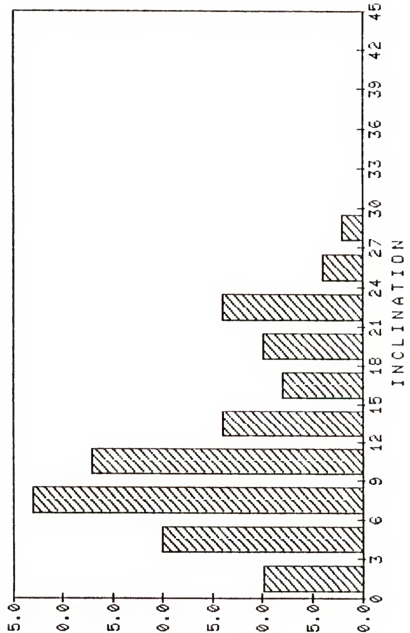

Figure B.5. Number density vs. inclination at 0.75 A.U.

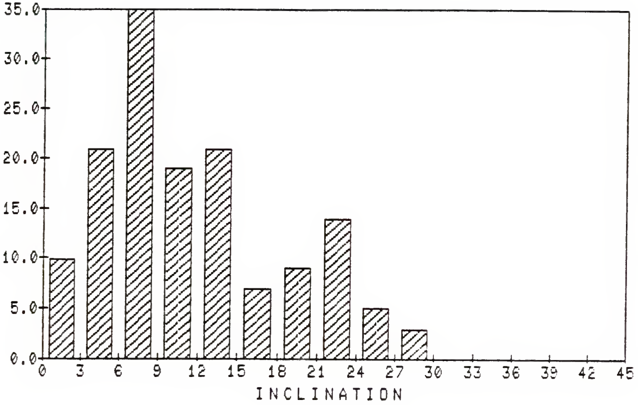

Figure B.6. Number density vs. inclination at 0.85 A.U.

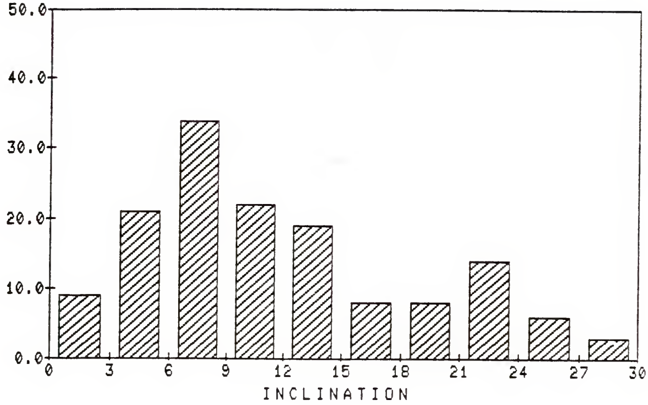

Figure B.7. Number density vs. inclination at 0.95 A.U.

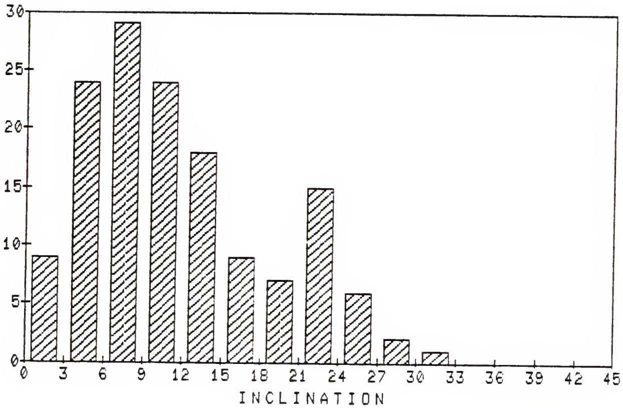

Figure B.8. Number density vs. inclination at 1.05 A.U.

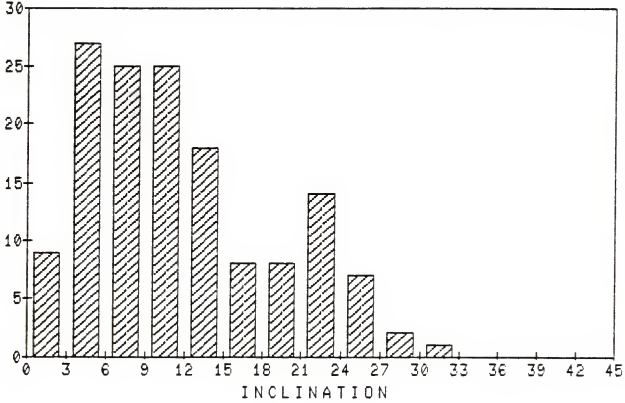

Figure B.9. Number density vs. inclination at 1.15 A.U.

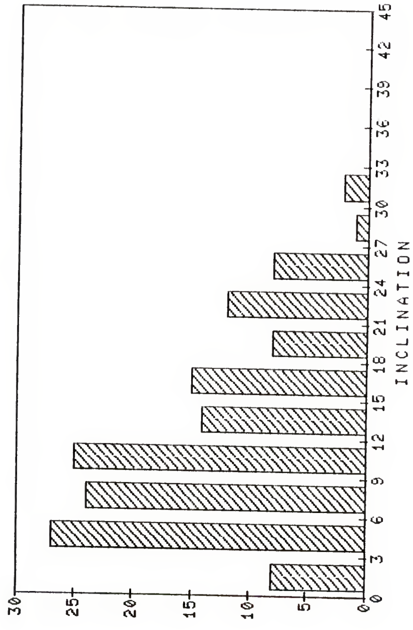

Figure B.10. Number density vs. inclination at 1.25 A.U.

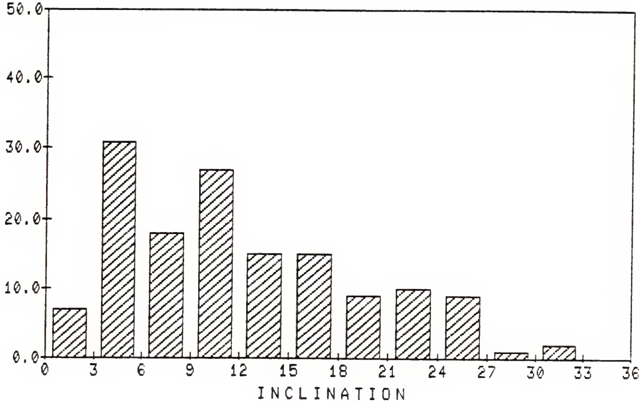

Figure B.11. Number density vs. inclination at 1.35 A.U.

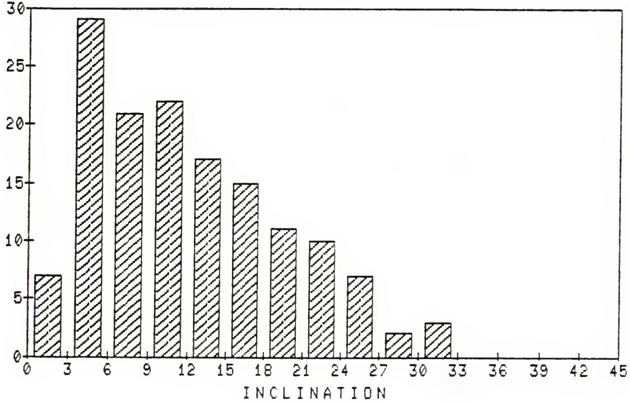

Figure B.12. Number density vs. inclination at 1.45 A.U.

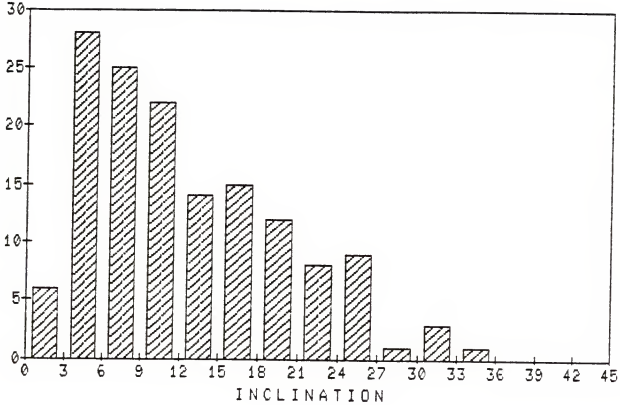

Figure B.13. Number density vs. inclination at 1.55 A.U.

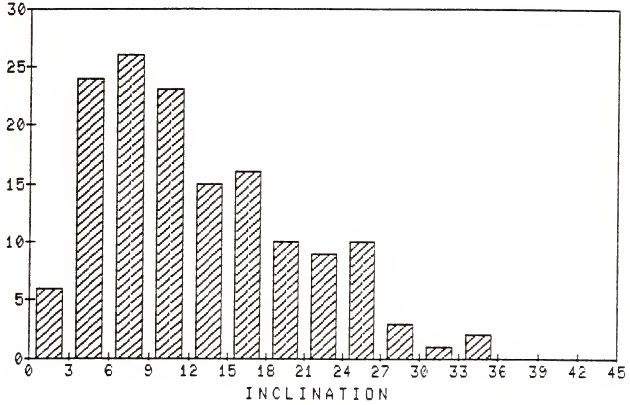

Figure B.14. Number density vs. inclination at 1.65 A.U.

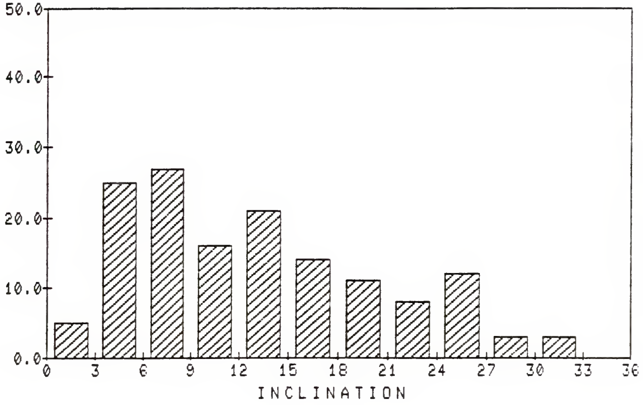

Figure B.15. Number density vs. inclination at 1.75 A.U.

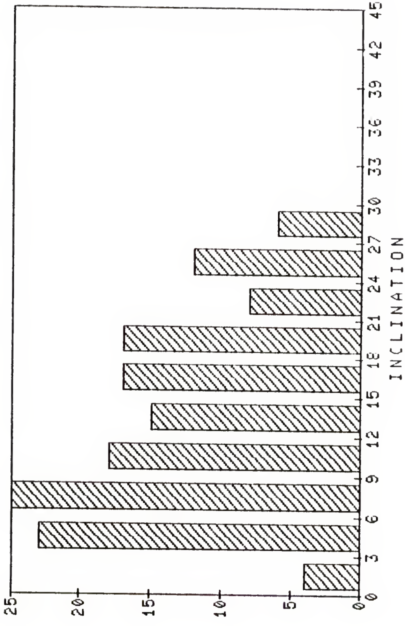

Figure B.16. Number density vs. inclination at 1.85 A.U.

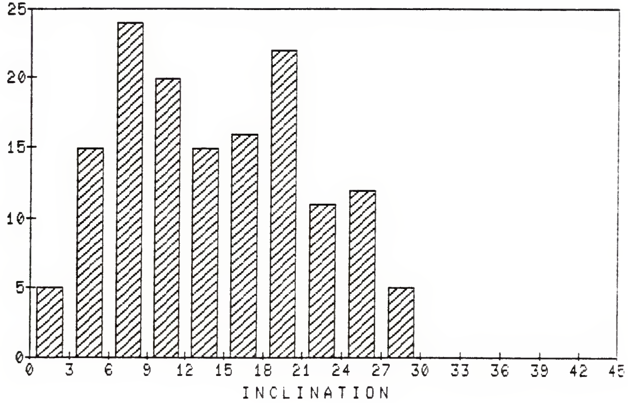

Figure B.17. Number density vs. inclination at 1.95 A.U.

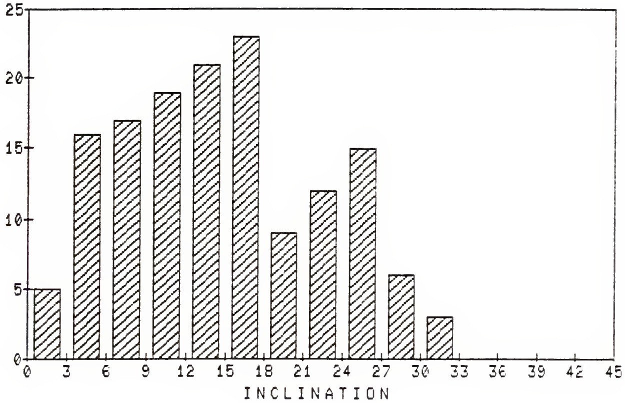

Figure B.18. Number density vs. inclination at 2.05 A.U.

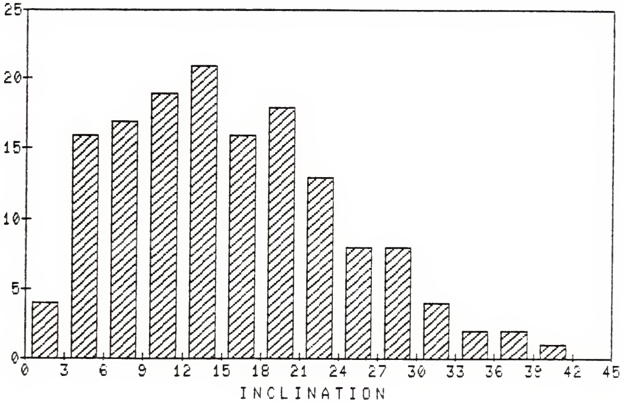

Figure B.19. Number density vs. inclination at 2.15 A.U.

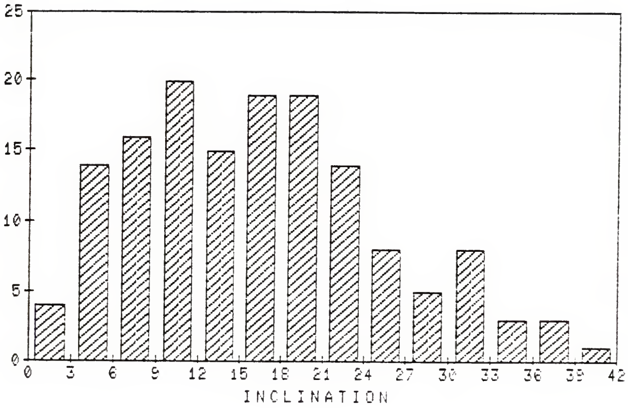

Figure B.20. Number density vs. inclination at 2.25 A.U.

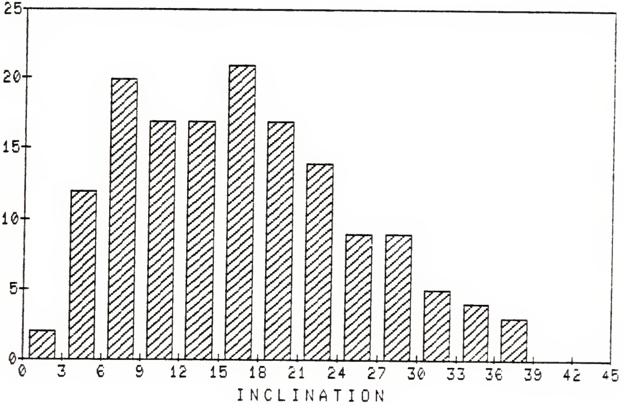

Figure B.21. Number density vs. inclination at 2.35 A.U.

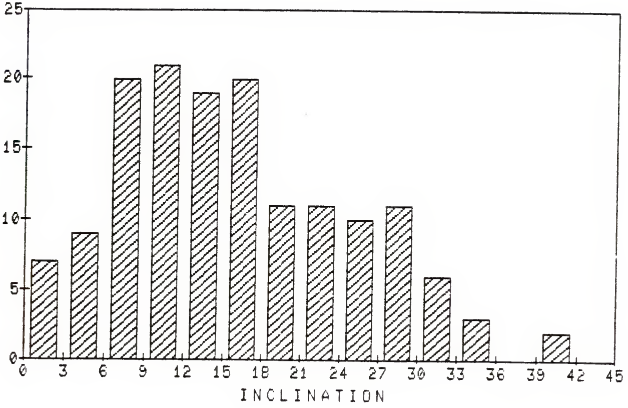

Figure B.22. Number density vs. inclination at 2.45 A.U.

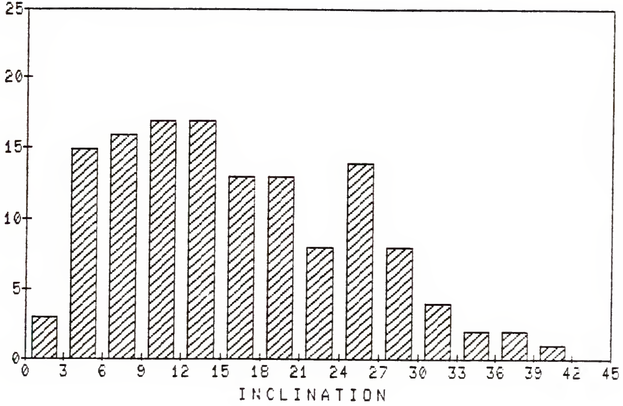

Figure B.23. Number density vs. inclination at 2.55 A.U.

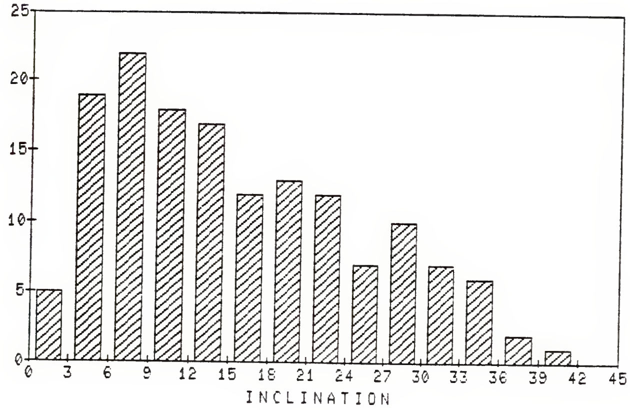

Figure B.24. Number density vs. inclination at 2.65 A.U.

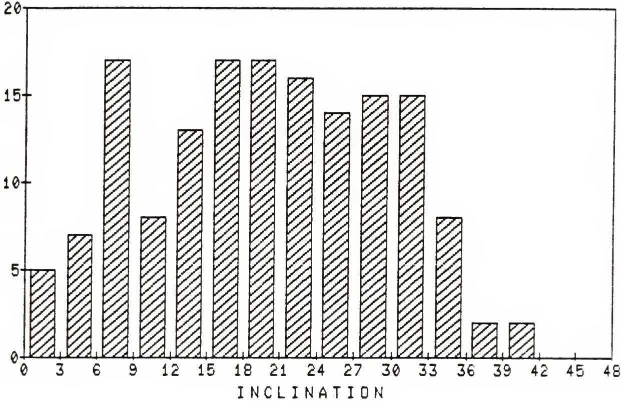

Figure B.25. Number density vs. inclination at 2.75 A.U.

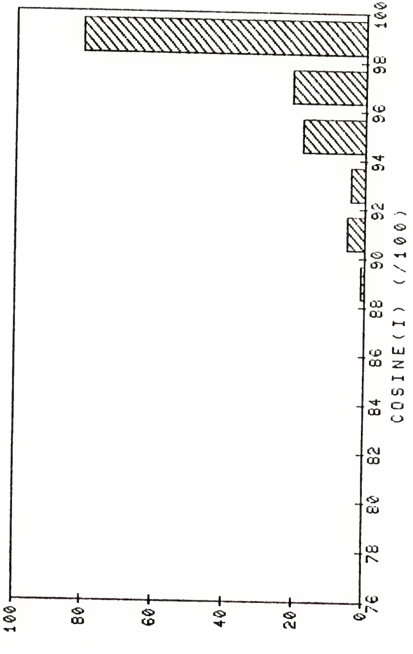

Figure B.26. Number density vs. cosine of inclination at 0.35 A.U.

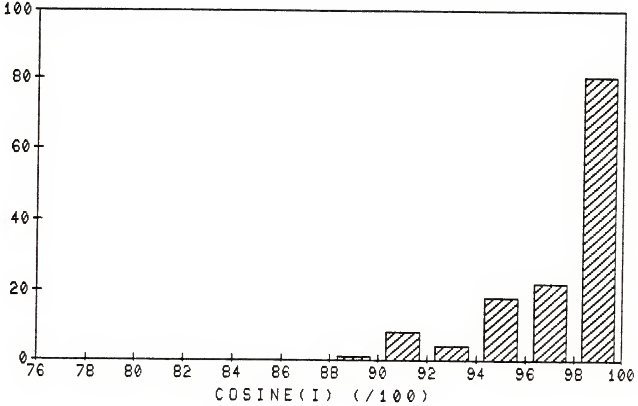

Figure B.27. Number density vs. cosine of inclination at 0.45 A.U.

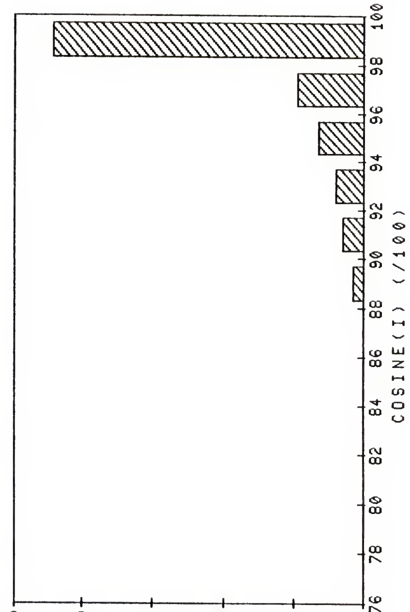

Figure B.28. Number density vs. cosine of inclination at 0.55 A.U.

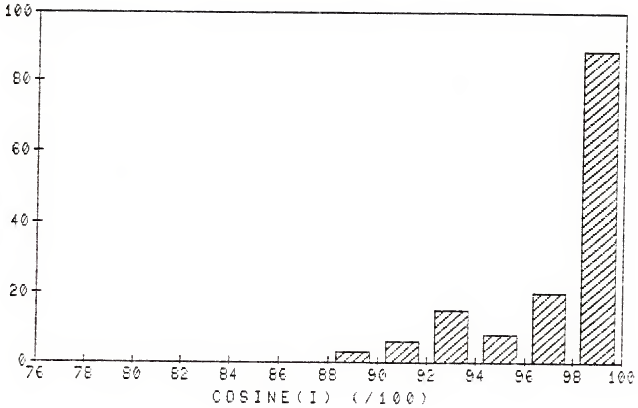

Figure B.29. Number density vs. cosine of inclination at 0.65 A.U.

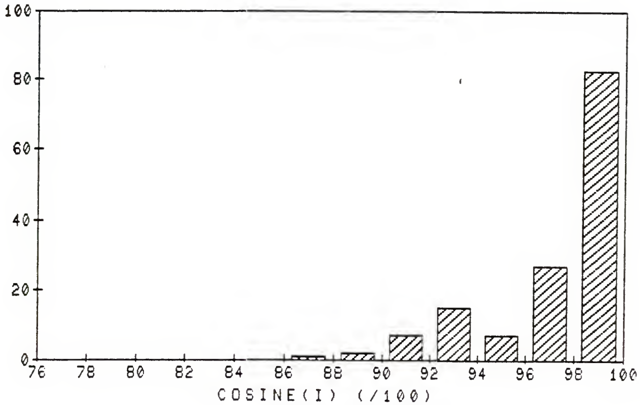

Figure B.30. Number density vs. cosine of inclination at 0.75 A.U.

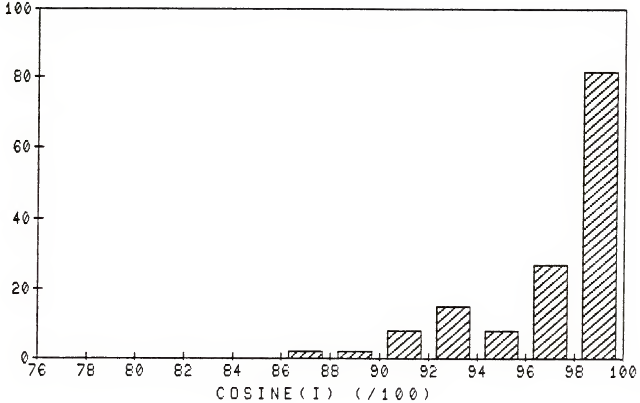

Figure B.31. Number density vs. cosine of inclination at 0.85 A.U.

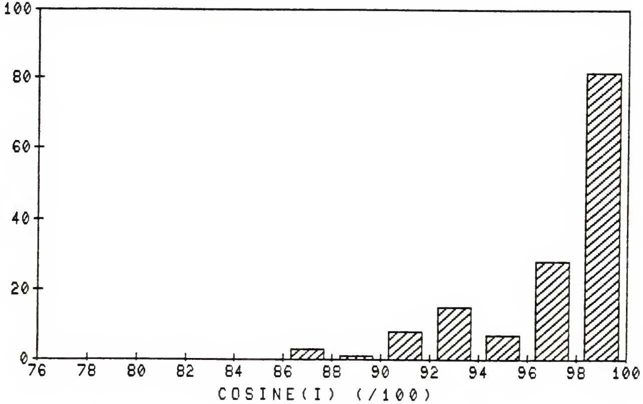

Figure B.32. Number density vs. cosine of inclination at 0.95 A.U.

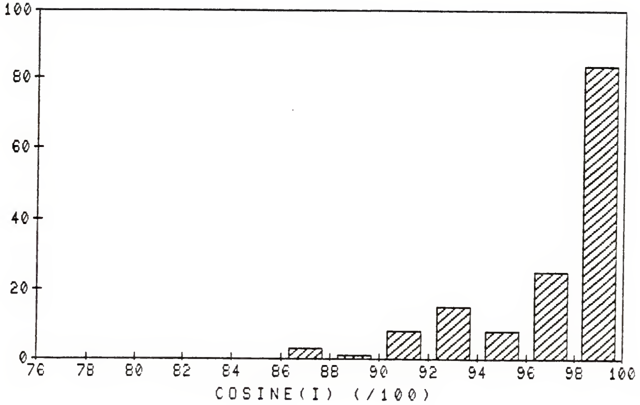

Figure B.33. Number density vs. cosine of inclination at 1.05 A.U.

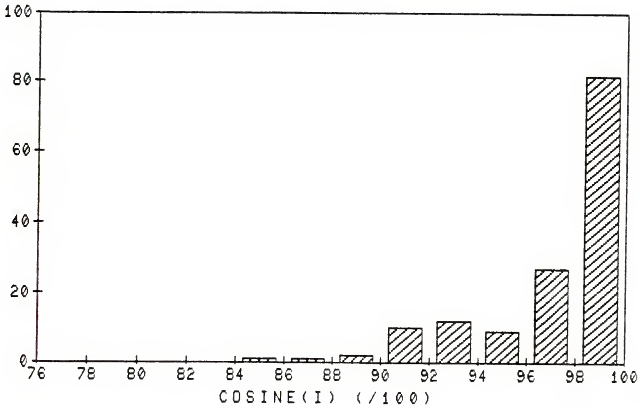

Figure B.34. Number density vs. cosine of inclination at 1.15 A.U.

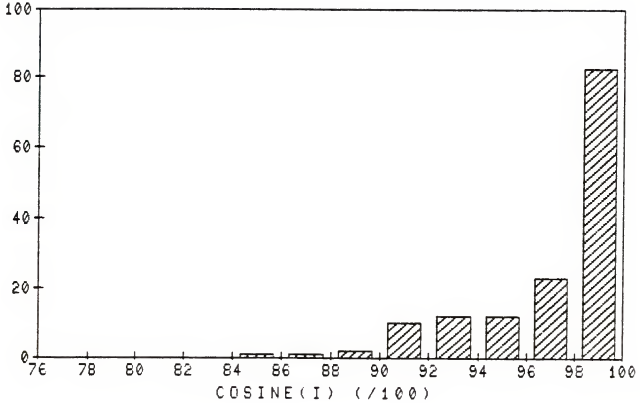

Figure B.35. Number density vs. cosine of inclination at 1.25 A.U.

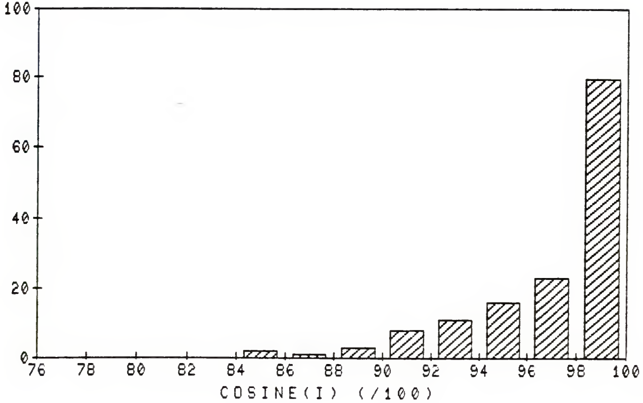

Figure B.36. Number density vs. cosine of inclination at 1.35 A.U.

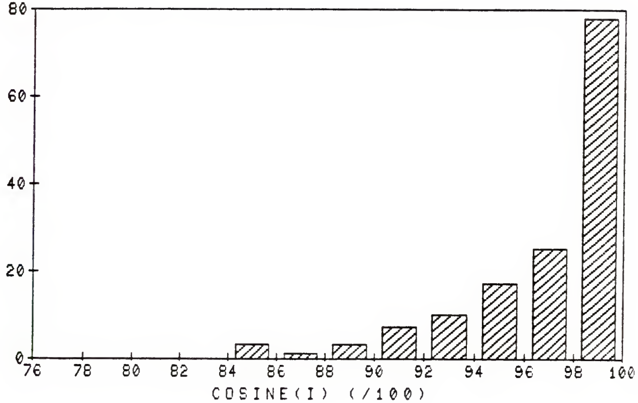

Figure B.37. Number density vs. cosine of inclination at 1.45 A.U.

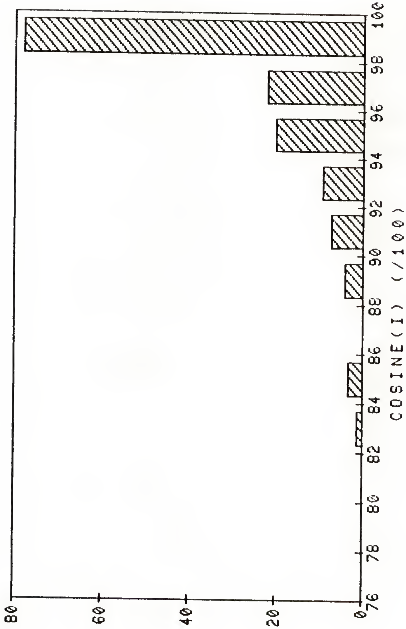

Figure B.38. Number density vs. cosine of inclination at 1.55 A.U.

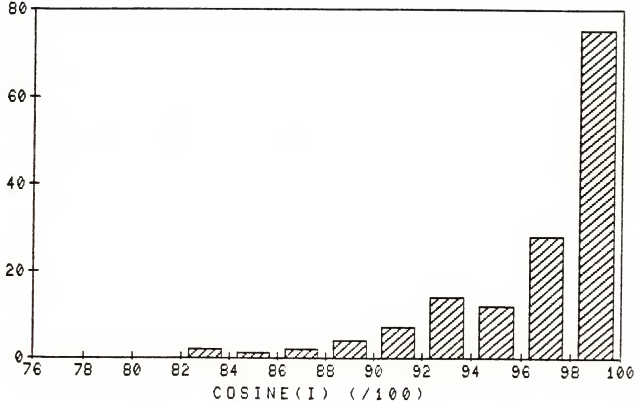

Figure B.39. Number density vs. cosine of inclination at 1.65 A.U.

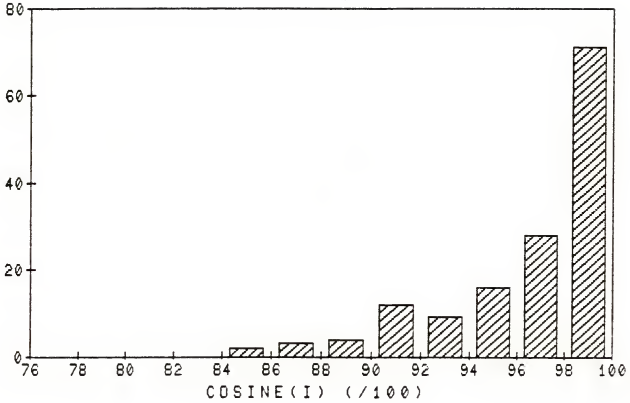

Figure B.40. Number density vs. cosine of inclination at 1.75 A.U.

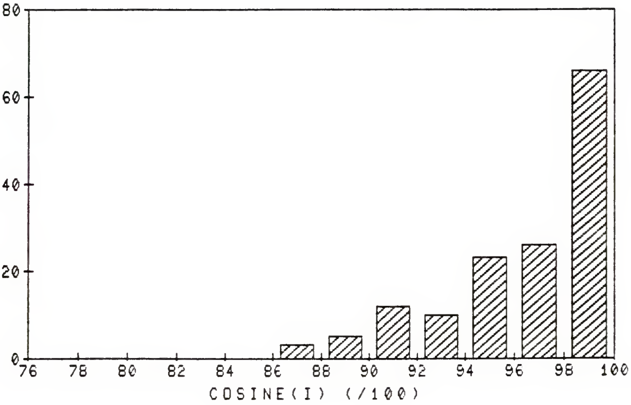

Figure B.41. Number density vs. cosine of inclination at 1.85 A.U.

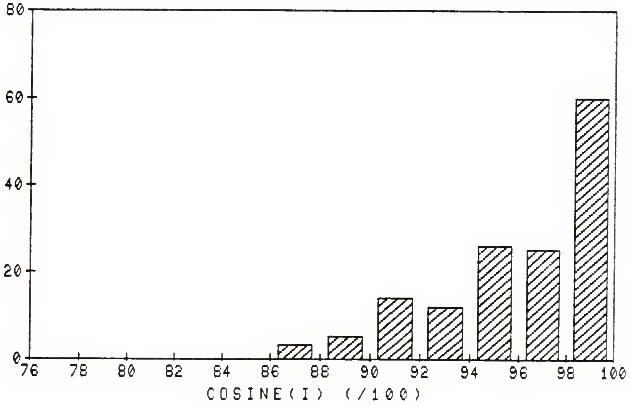

Figure B.42. Number density vs. cosine of inclination at 1.95 A.U.

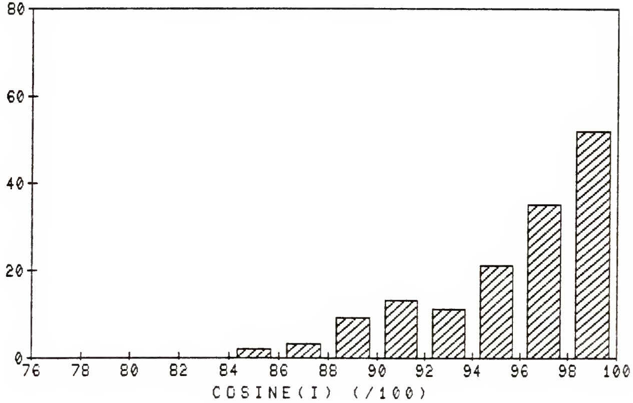

Figure B.43. Number density vs. cosine of inclination at 2.05 A.U.

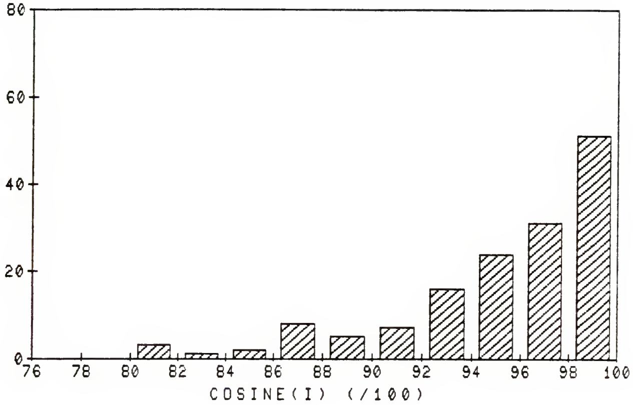

Figure B.44. Number density vs. cosine of inclination at 2.15 A.U.

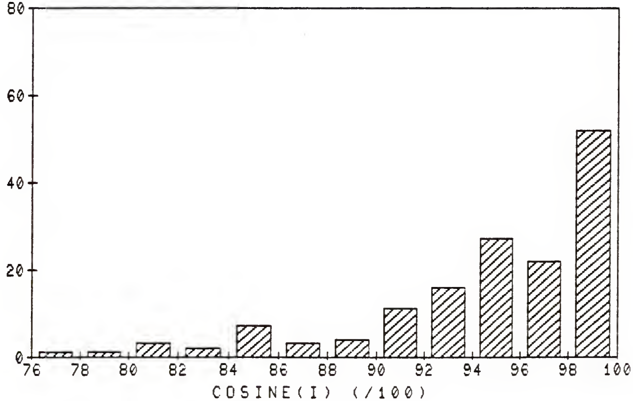

Figure B.45. Number density vs. cosine of inclination at 2.25 A.U.

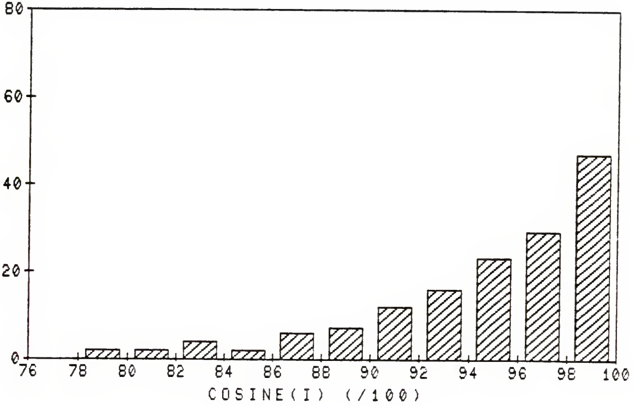

Figure B.46. Number density vs. cosine of inclination at 2.35 A.U.

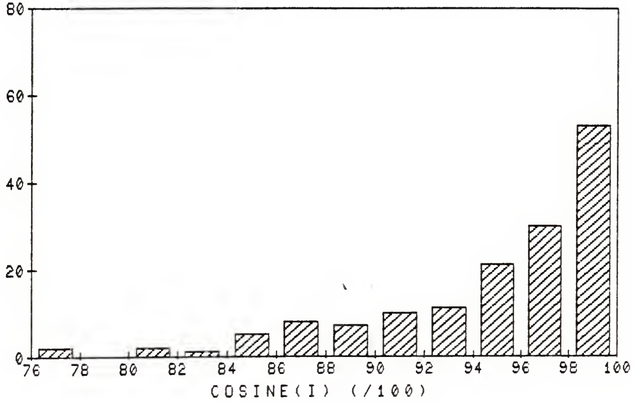

Figure B.47. Number density vs. cosine of inclination at 2.45 A.U.

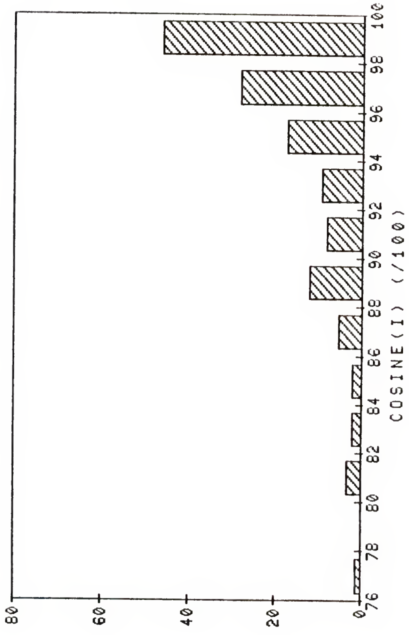

Figure B.48. Number density vs. cosine of inclination at 2.55 A.U.

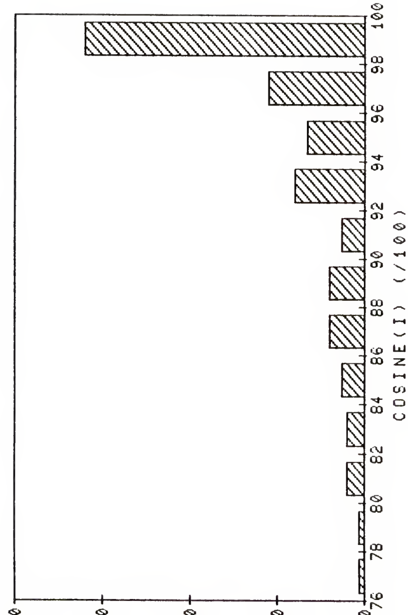

Figure B.49. Number density vs. cosine of inclination at 2.65 A.U.

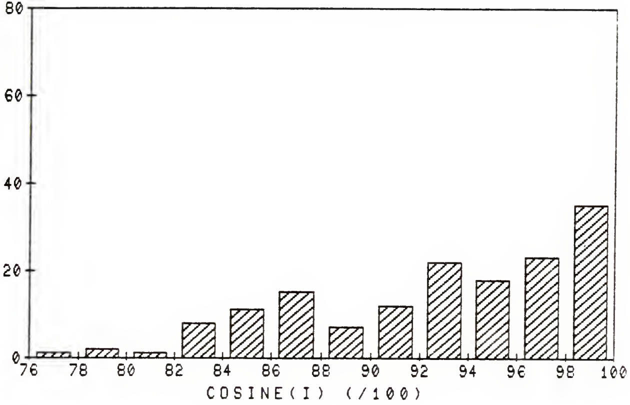

Figure B.50. Number density vs. cosine of inclination at 2.75 A.U.

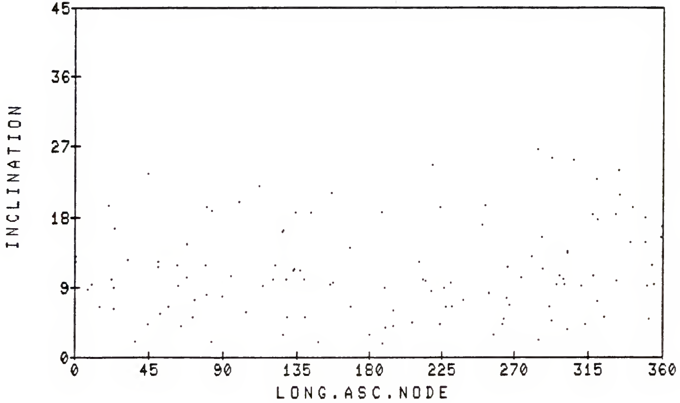

Figure B.51. Inclination vs. longitude of the ascending node at 0.35 A.U.

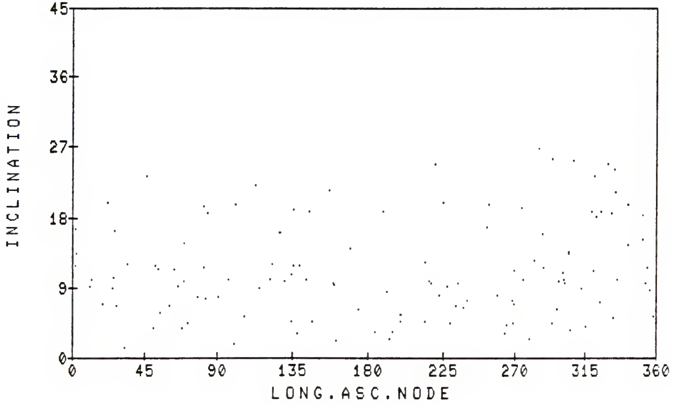

Figure B.52. Inclination vs. longitude of the ascending node at 0.45 A.U.

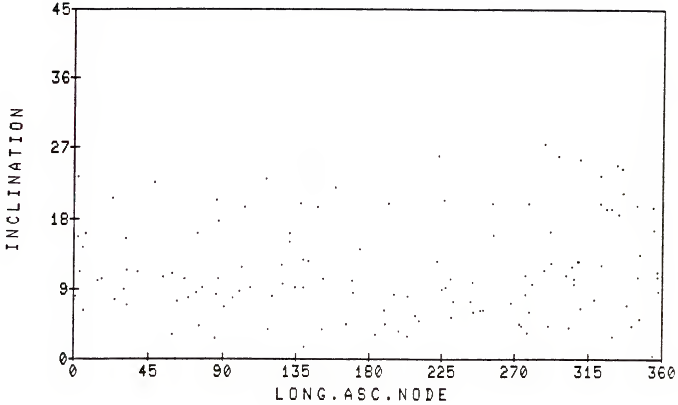

Figure B.53. Inclination vs. longitude of the ascending node at 0.55 A.U.

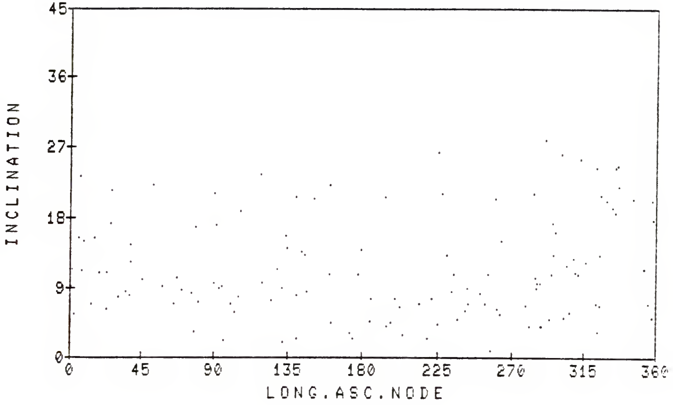

Figure B.54. Inclination vs. longitude of the ascending node at 0.65 A.U.

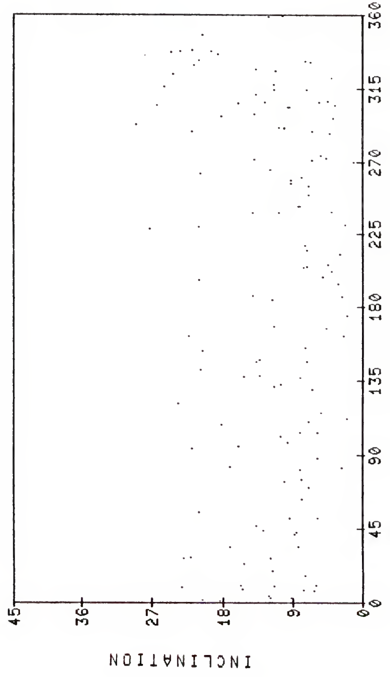

Figure B.55. Inclination vs. longitude of the ascending node at 0.75 A.U.

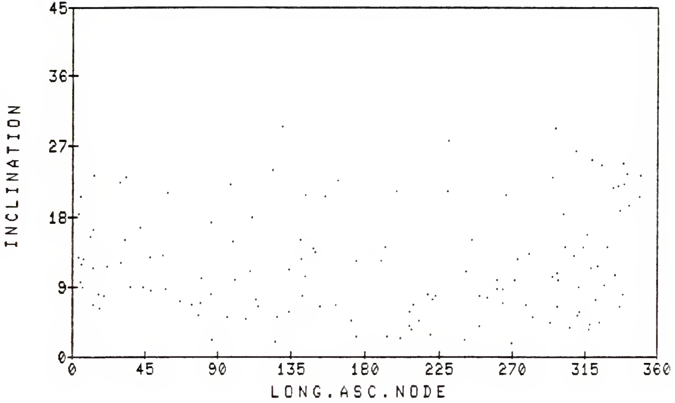

Figure B.56. Inclination vs. longitude of the ascending node at 0.85 A.U.

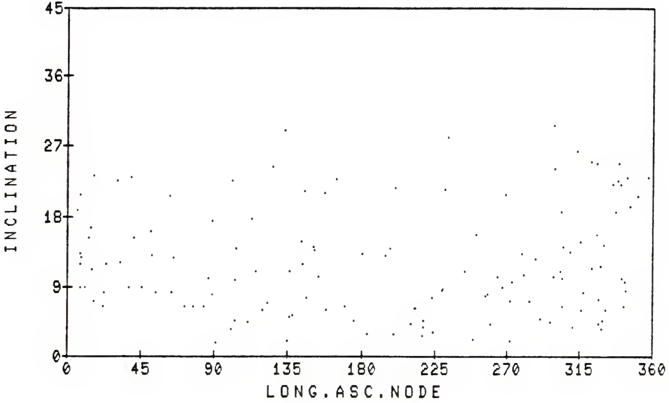

Figure B.57. Inclination vs. longitude of the ascending node at 0.95 A.U.

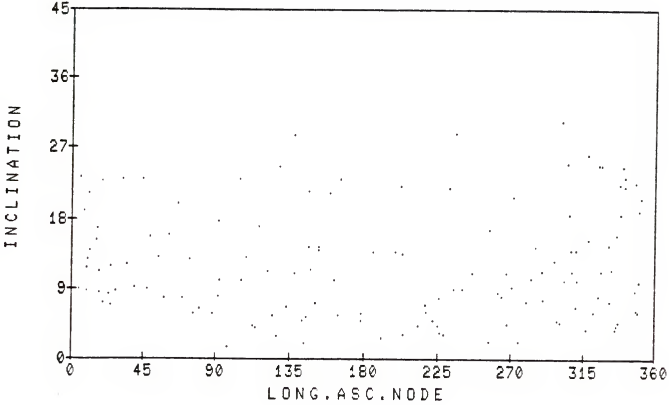

Figure B.58. Inclination vs. longitude of the ascending node at 1.05 A.U.

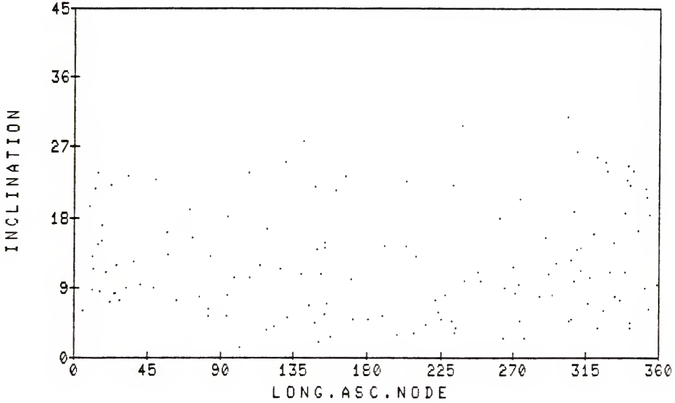

Figure B.59. Inclination vs. longitude of the ascending node at 1.15 A.U.

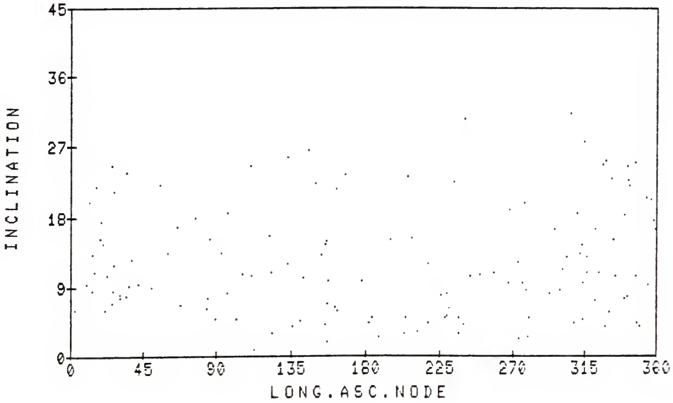

Figure B.60. Inclination vs. longitude of the ascending node at 1.25 A.U.

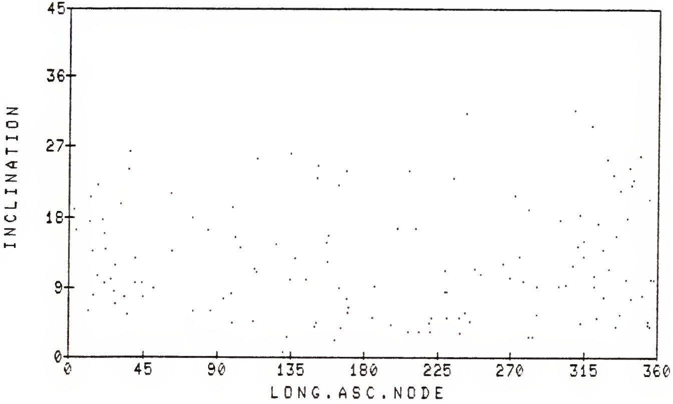

Figure B.61. Inclination vs. longitude of the ascending node at 1.35 A.U.

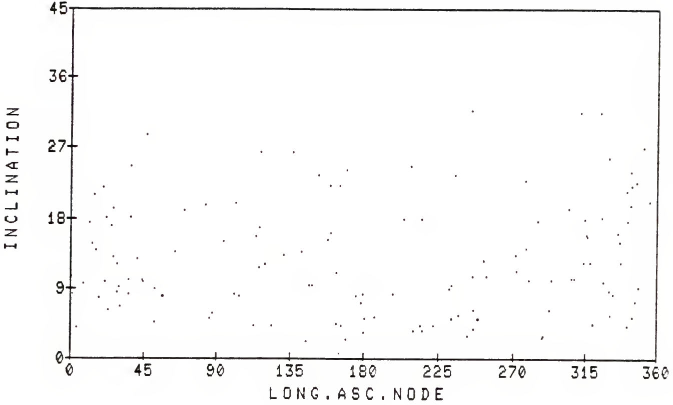

Figure B.62. Inclination vs. longitude of the ascending node at 1.45 A.U.

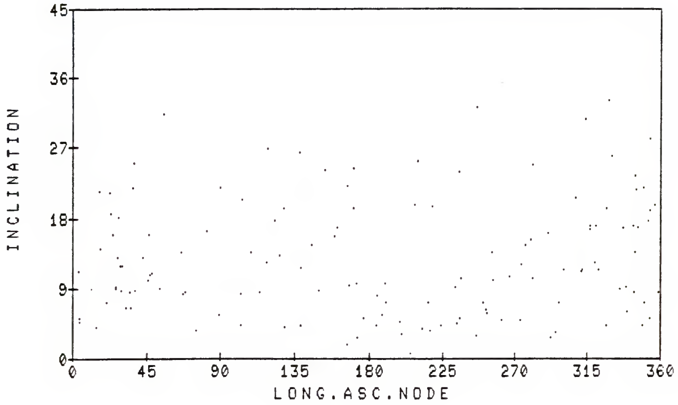

Figure B.63. Inclination vs. longitude of the ascending node at 1.55 A.U.

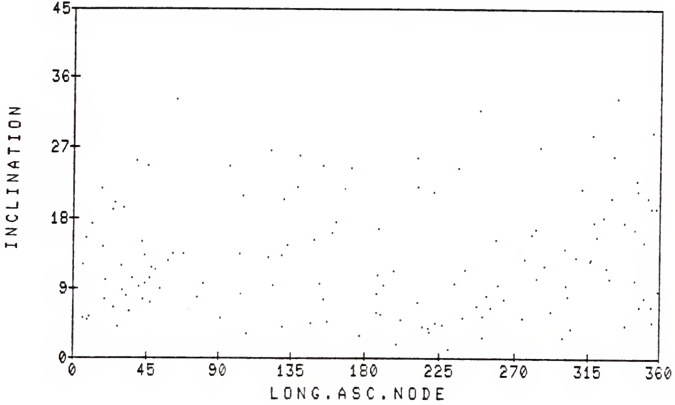

Figure B.64. Inclination vs. longitude of the ascending node at 1.65 A.U.

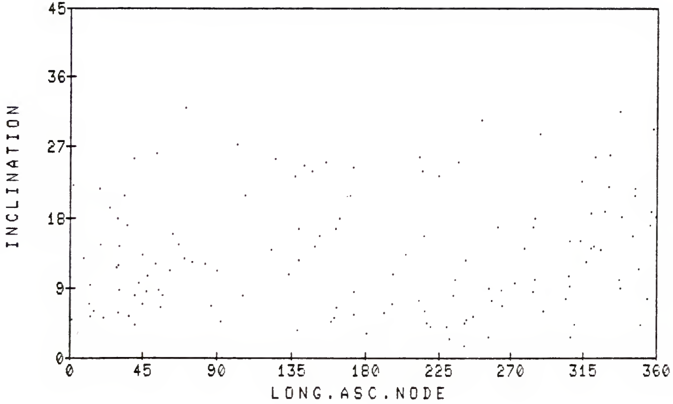

Figure B.65. Inclination vs. longitude of the ascending node at 1.75 A.U.

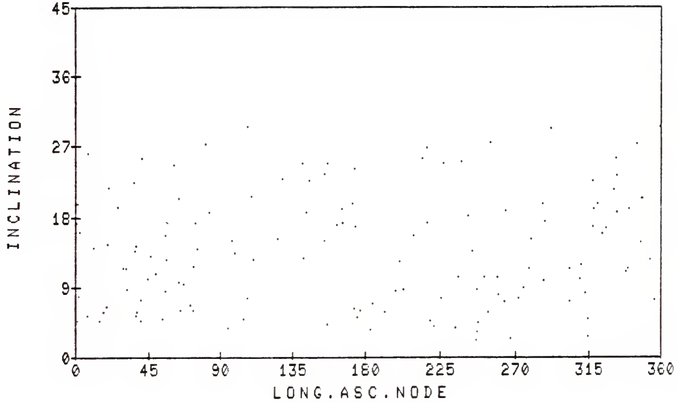

Figure B.66. Inclination vs. longitude of the ascending node at 1.85 A.U.

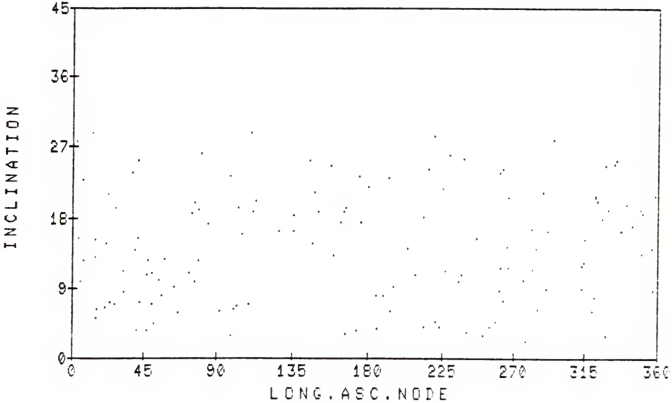

Figure B.67. Inclination vs. longitude of the ascending node at 1.95 A.U.

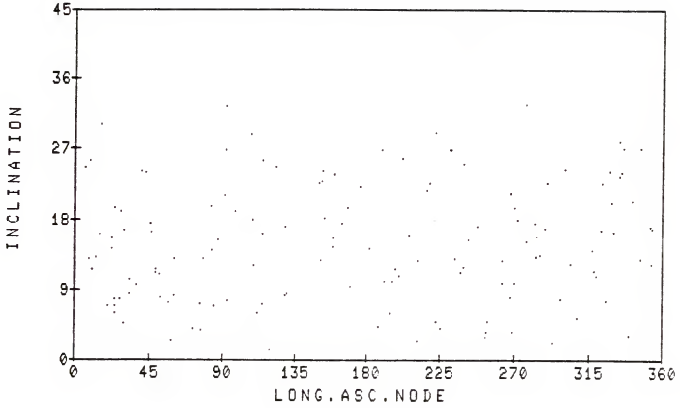

Figure B.68. Inclination vs. longitude of the ascending node at 2.05 A.U.

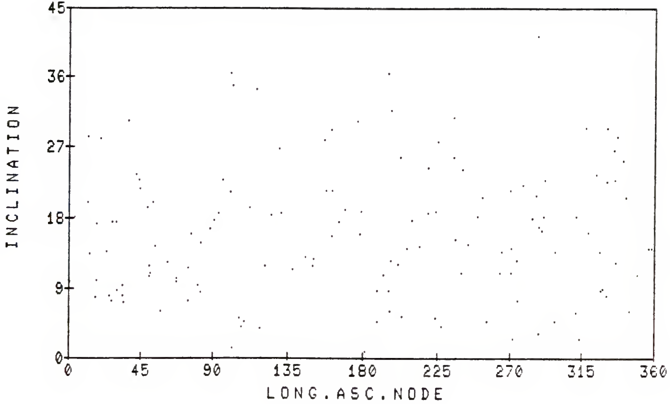

Figure B.69. Inclination vs. longitude of the ascending node at 2.15 A.U.

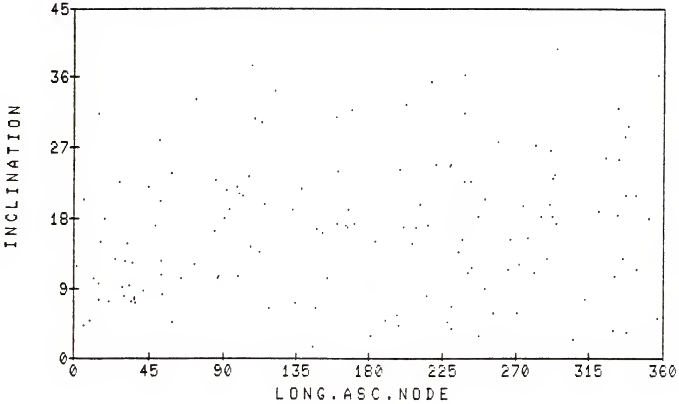

Figure B.70. Inclination vs. longitude of the ascending node at 2.25 A.U.

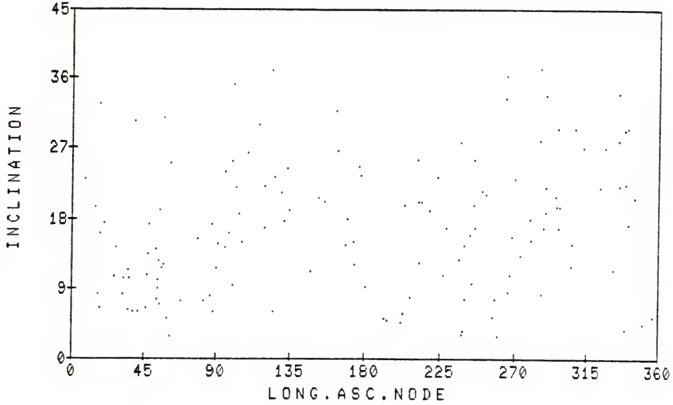

Figure B.71. Inclination vs. longitude of the ascending node at 2.35 A.U.

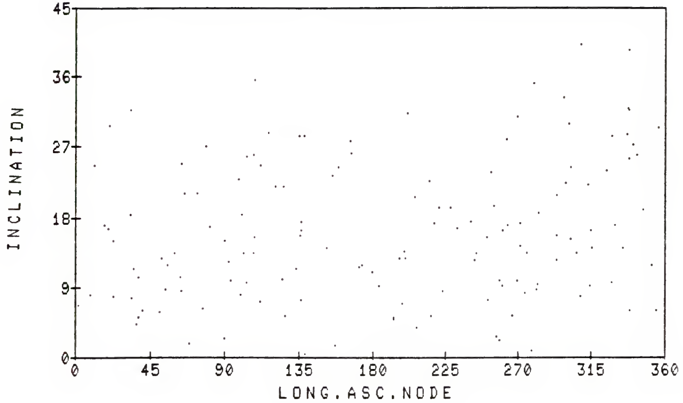

Figure B.72. Inclination vs. longitude of the ascending node at 2.45 A.U.

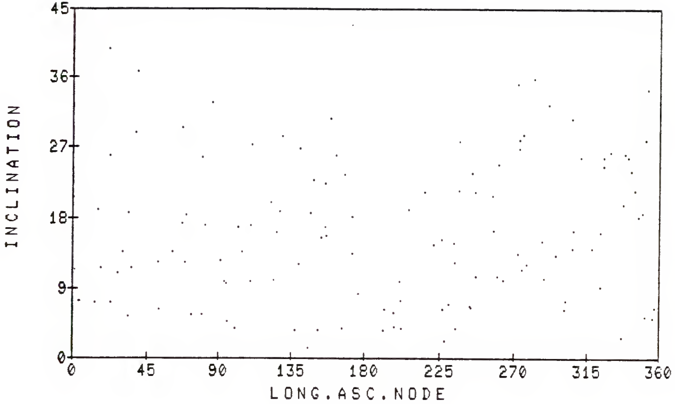

Figure B.73. Inclination vs. longitude of the ascending node at 2.55 A.U.

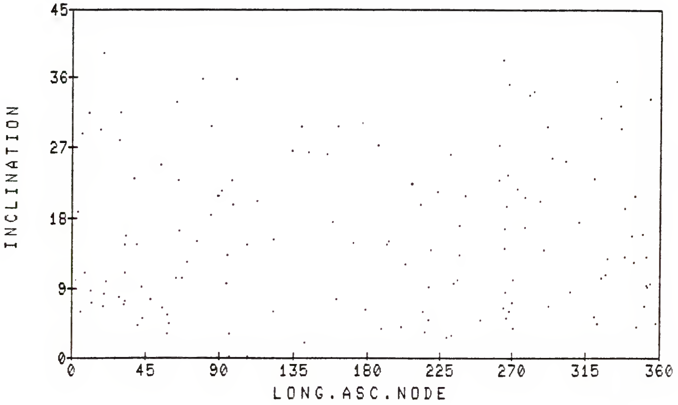

Figure B.74. Inclination vs. longitude of the ascending node at 2.65 A.U.

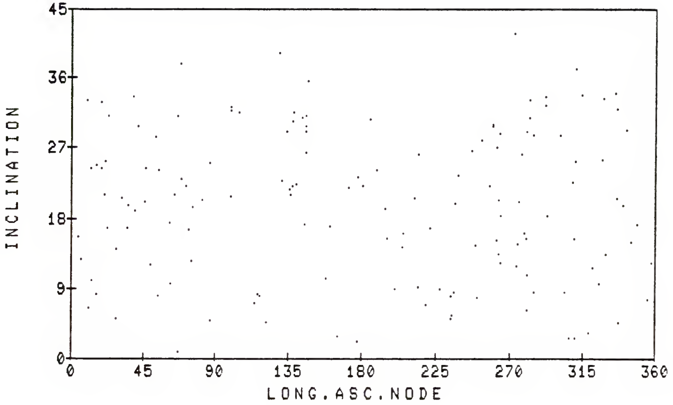

Figure B.75. Inclination vs. longitude of the ascending node at 2.75 A.U.

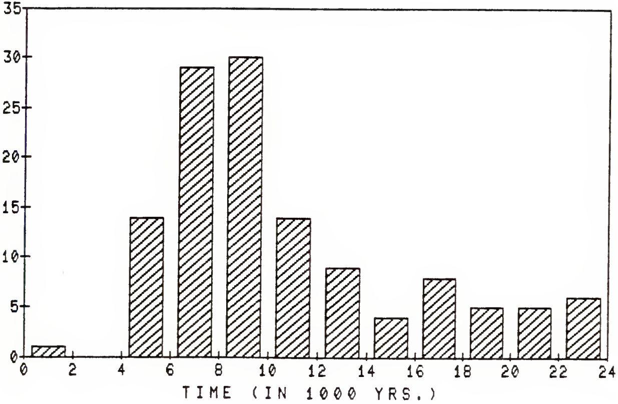

Figure B.76. Number density vs. time of infall at 0.35 A.U.

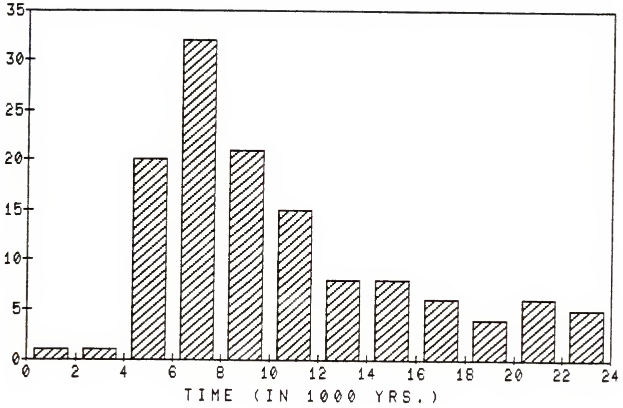

Figure B.77. Number density vs. time of infall at 0.45 A.U.

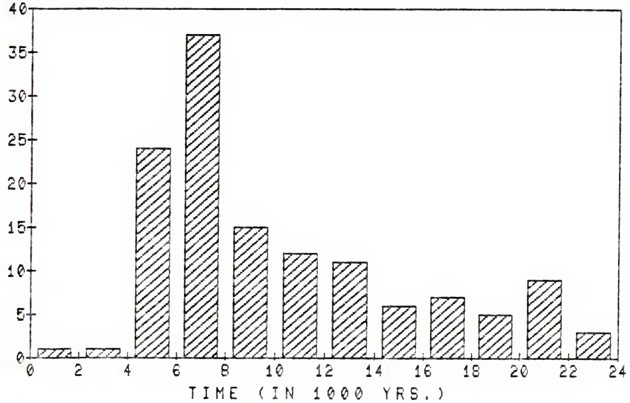

Figure B.78. Number density vs. time of infall at 0.55 A.U.

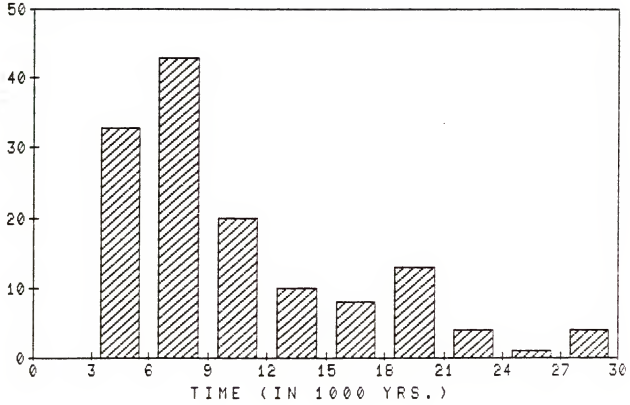

Figure B.79. Number density vs. time of infall at 0.65 A.U.

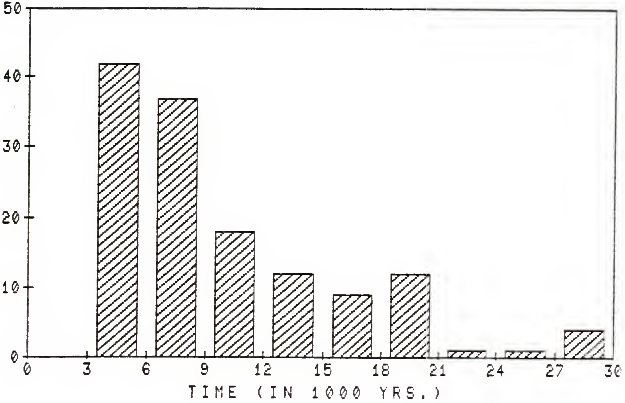

Figure B.80. Number density vs. time of infall at 0.75 A.U.

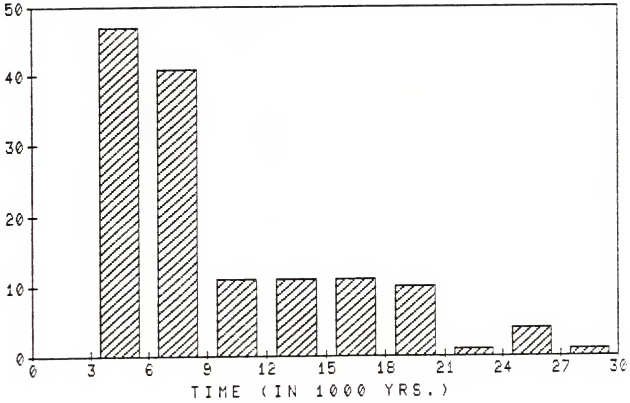

Figure B.81. Number density vs. time of infall at 0.85 A.U.

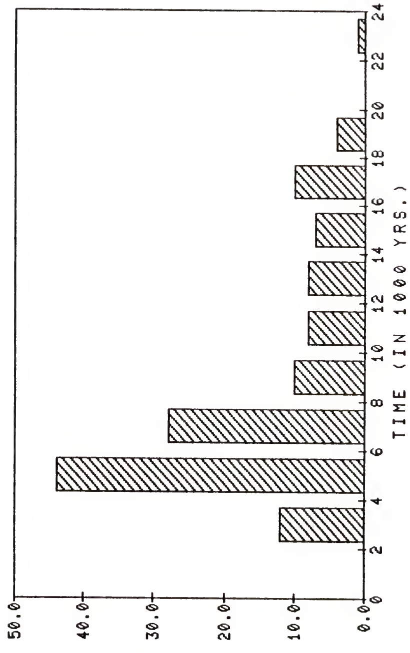

Figure B.82. Number density vs. time of infall at 0.95 A.U.

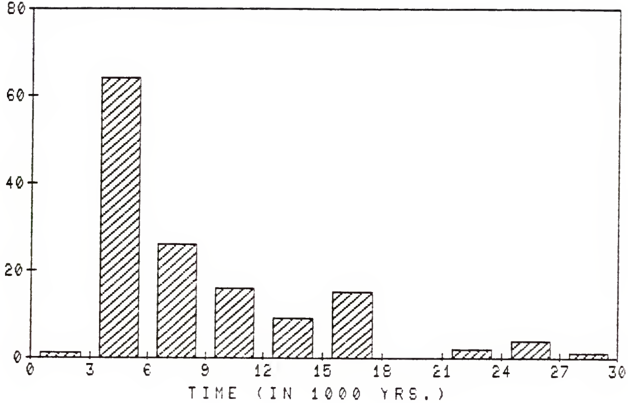

Figure B.83. Number density vs. time of infall at 1.05 A.U.

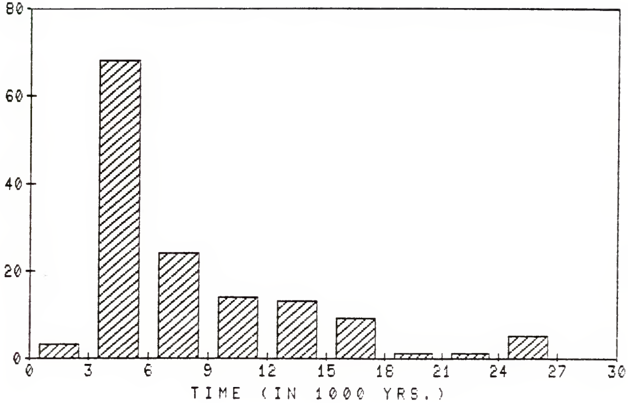

Figure B.84. Number density vs. time of infall at 1.15 A.U.

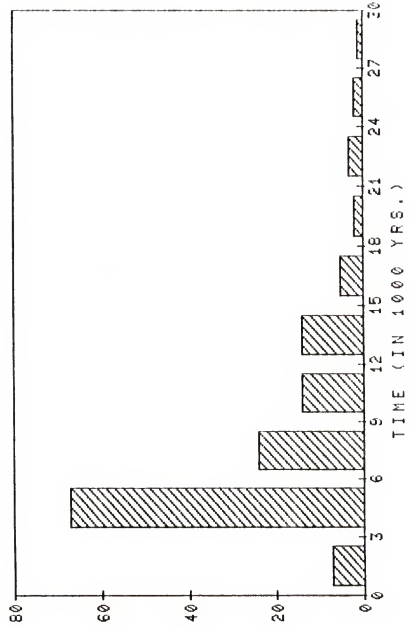

Figure B.85. Number density vs. time of infall at 1.25 A.U.

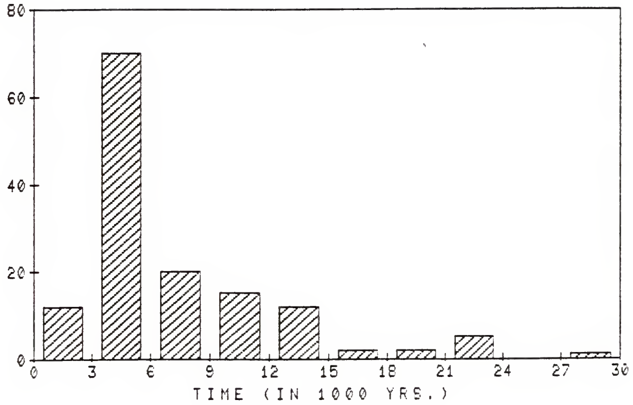

Figure B.86. Number density vs. time of infall at 1.35 A.U.

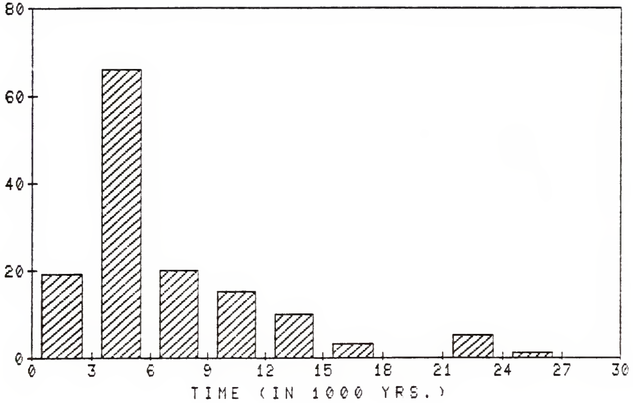

Figure B.87. Number density vs. time of infall at 1.45 A.U.

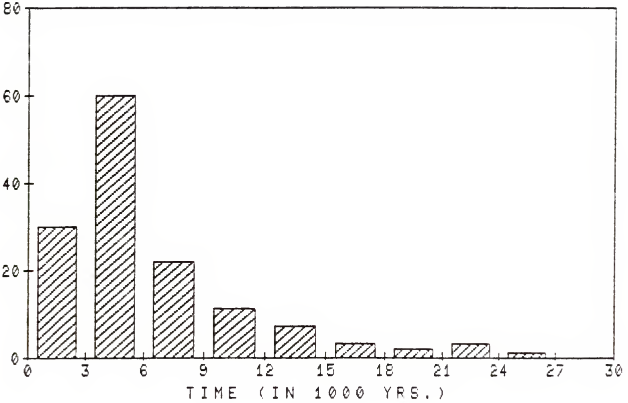

Figure B.88. Number density vs. time of infall at 1.55 A.U.

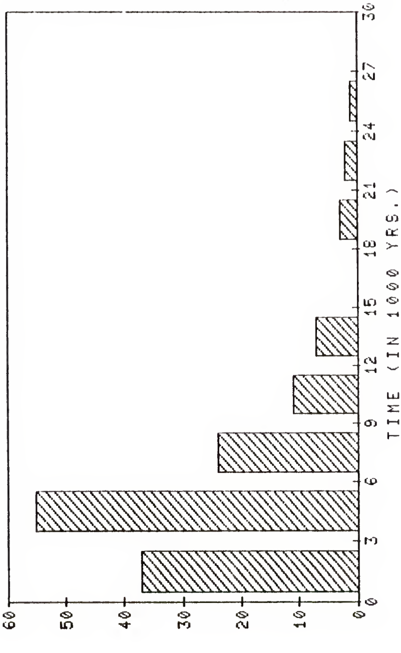

Figure B.89. Number density vs. time of infall at 1.65 A.U.

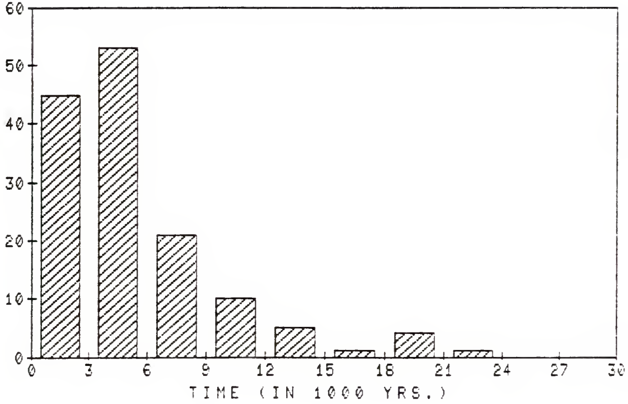

Figure B.90. Number density vs. time of infall at 1.75 A.U.

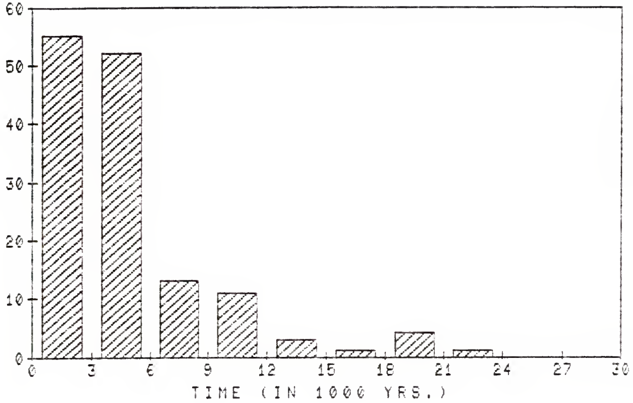

Figure B.91. Number density vs. time of infall at 1.85 A.U.

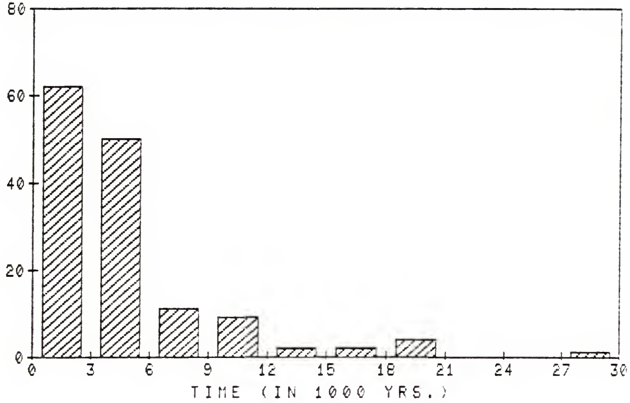

Figure B.92. Number density vs. time of infall at 1.95 A.U.

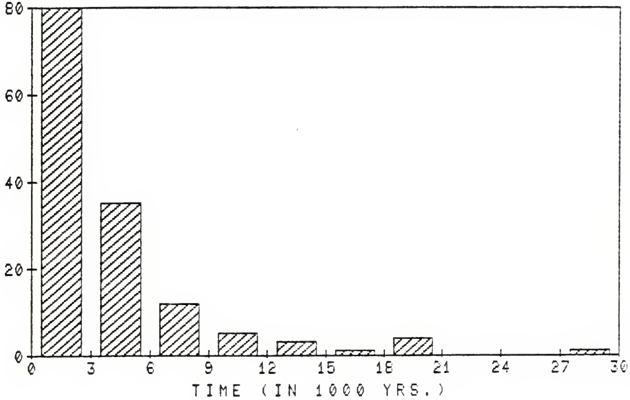

Figure B.93. Number density vs. time of infall at 2.05 A.U.

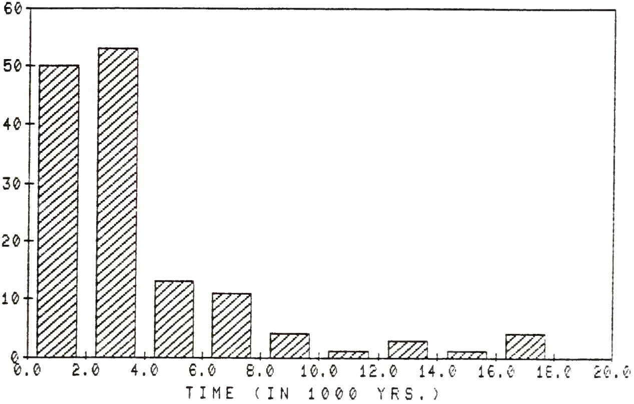

Figure B.94. Number density vs. time of infall at 2.15 A.U.

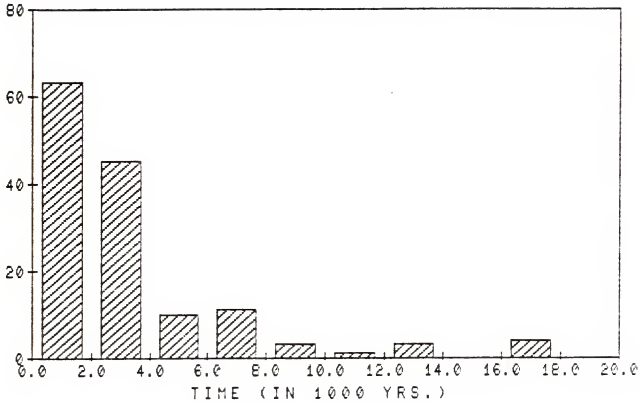

Figure B.95. Number density vs. time of infall at 2.25 A.U.

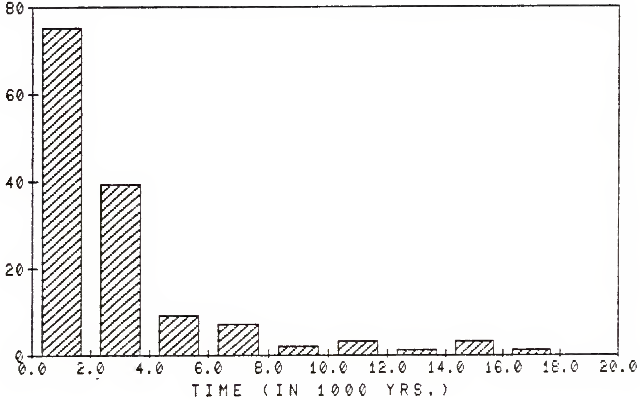

Figure B.96. Number density vs. time of infall at 2.35 A.U.

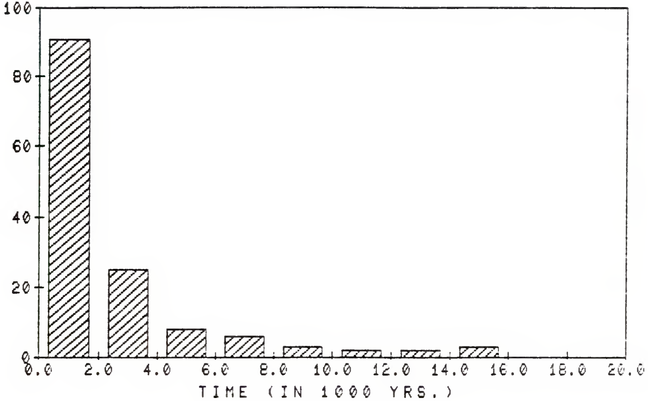

Figure B.97. Number density vs. time of infall at 2.45 A.U.

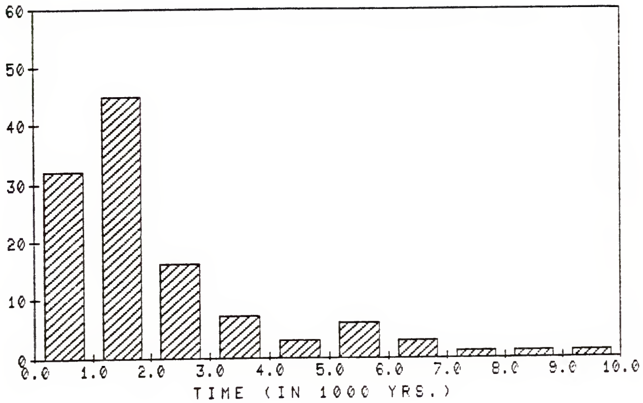

Figure B.98. Number density vs. time of infall at 2.55 A.U.

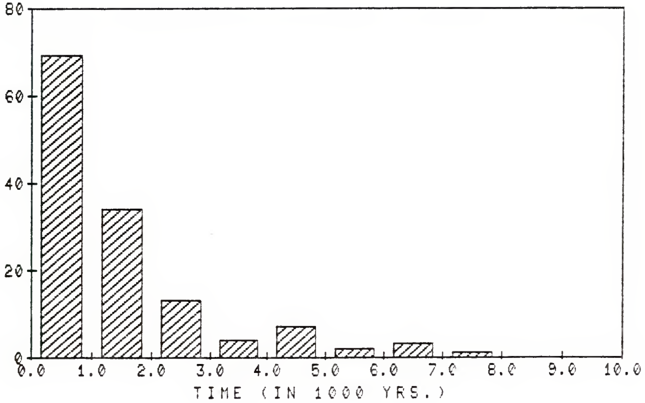

Figure B.99. Number density vs. time of infall at 2.65 A.U.

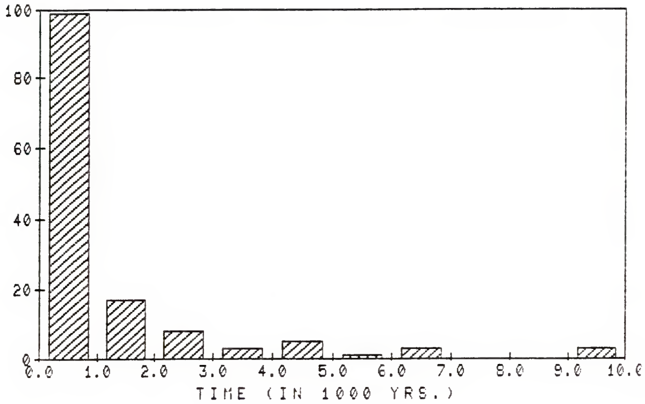

Figure B.100. Number density vs. time of infall at 2.75 A.U.

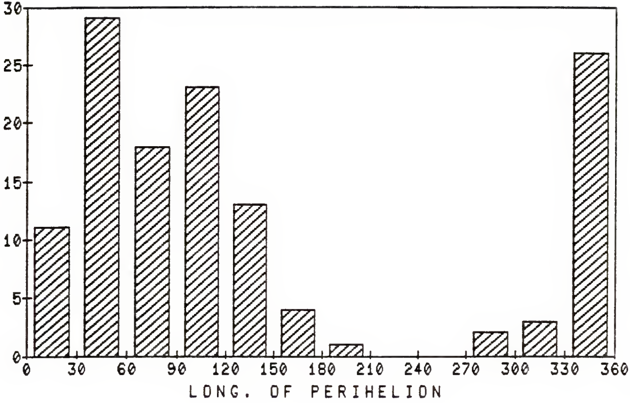

Figure 101. Number density vs. longitude of perihelion at 0.35 A.U.

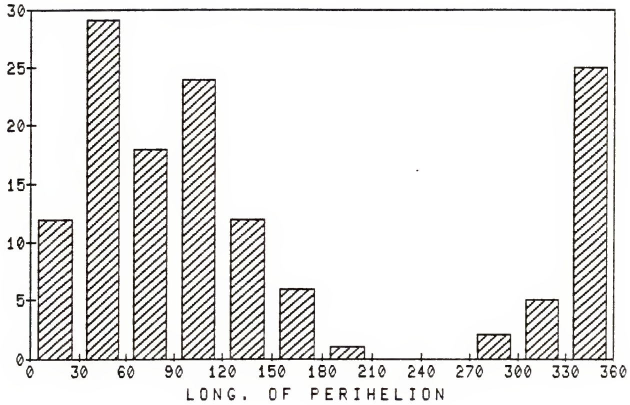

Figure 102. Number density vs. longitude of perihelion at 0.45 A.U.

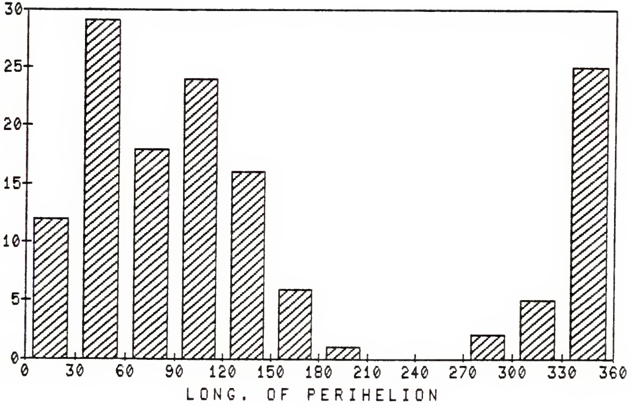

Figure 103. Number density vs. longitude of perihelion at 0.55 A.U.

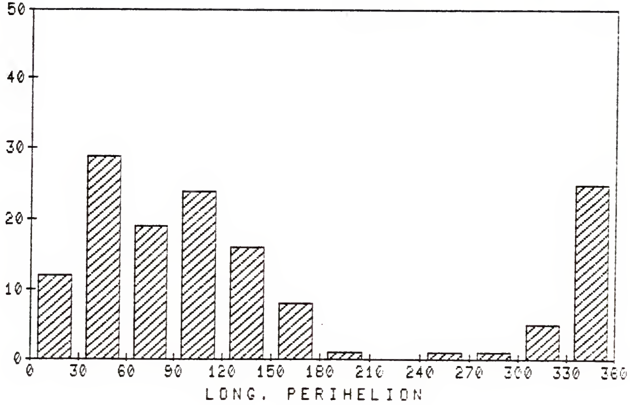

Figure 104. Number density vs. longitude of perihelion at 0.65 A.U.

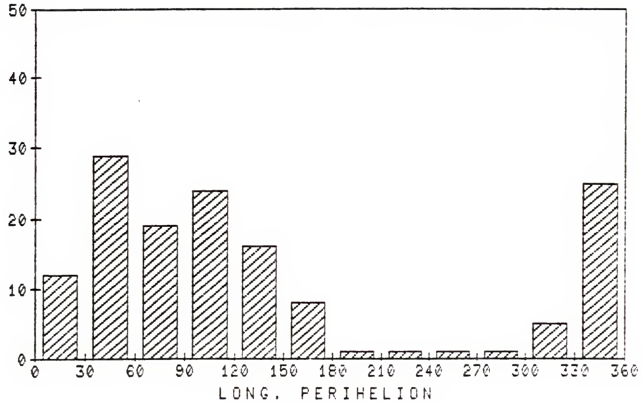

Figure 105. Number density vs. longitude of perihelion at 0.75 A.U.

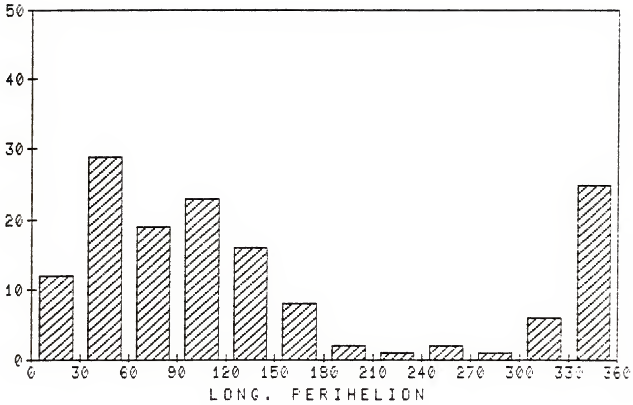

Figure 106. Number density vs. longitude of perihelion at 0.85 A.U.

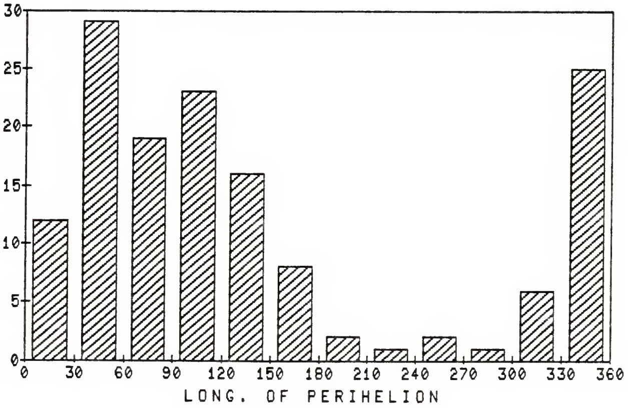

Figure 107. Number density vs. longitude of perihelion at 0.95 A.U.

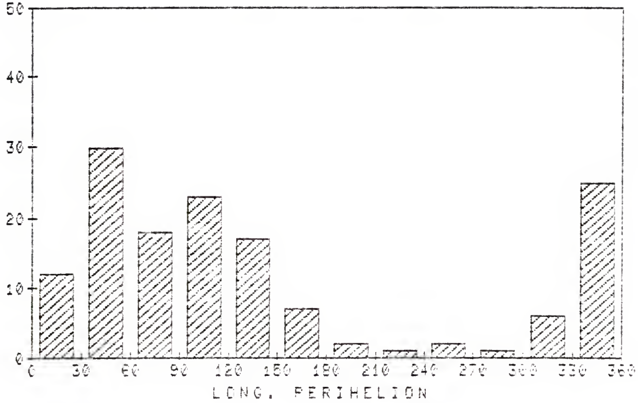

Figure 108. Number density vs. longitude of perihelion at 1.05 A.U.

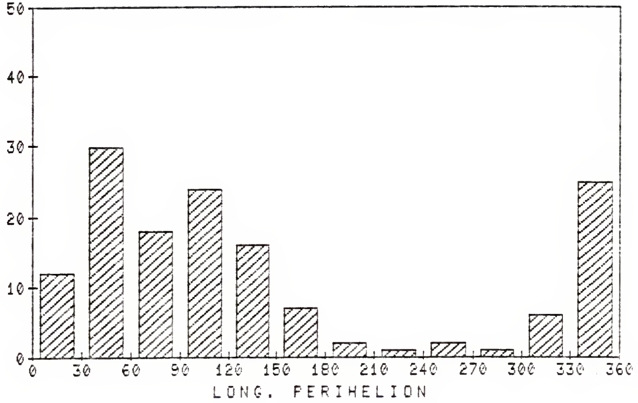

Figure 109. Number density vs. longitude of perihelion at 1.15 A.U.

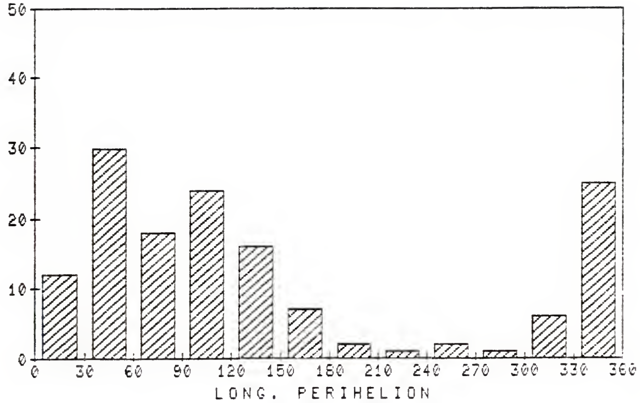

Figure 110. Number density vs. longitude of perihelion at 1.25 A.U.

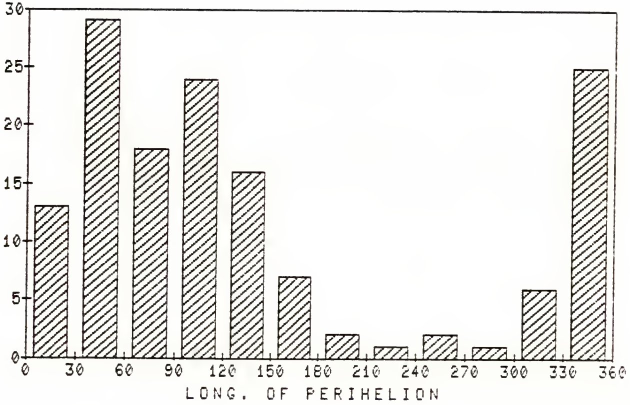

Figure 111. Number density vs. longitude of perihelion at 1.35 A.U.

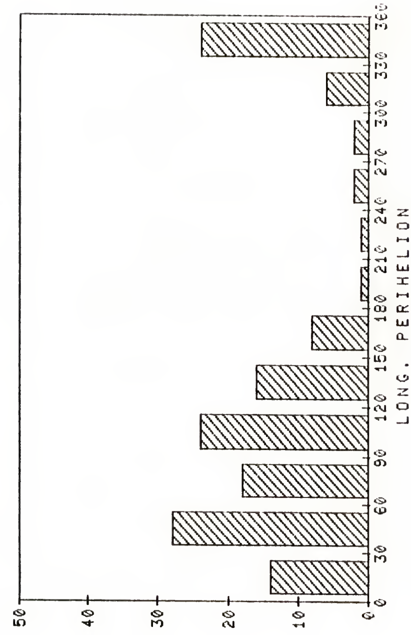

Figure 112. Number density vs. longitude of perihelion at 1.45 A.U.

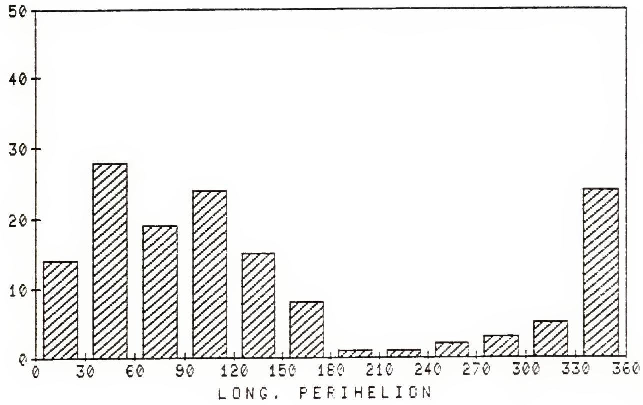

Figure 113. Number density vs. longitude of perihelion at 1.55 A.U.

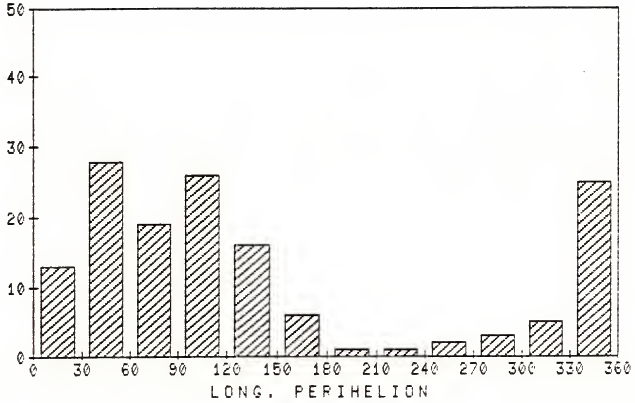

Figure 114. Number density vs. longitude of perihelion at 1.65 A.U.

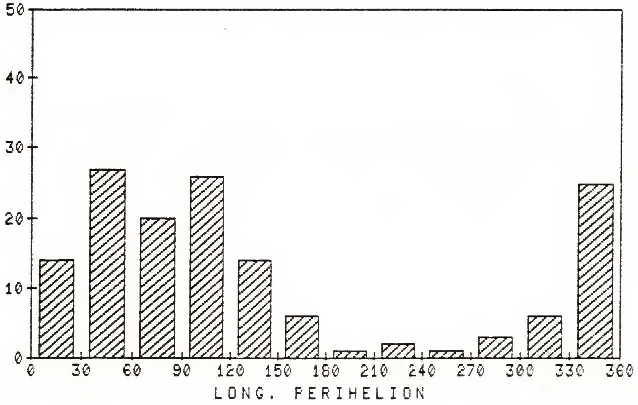

Figure 115. Number density vs. longitude of perihelion at 1.75 A.U.

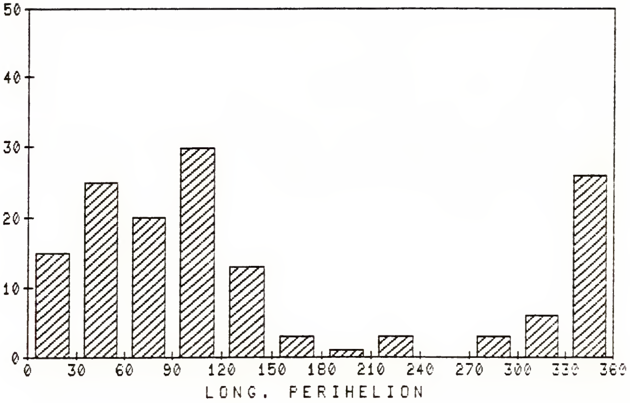

Figure 116. Number density vs. longitude of perihelion at 1.85 A.U.

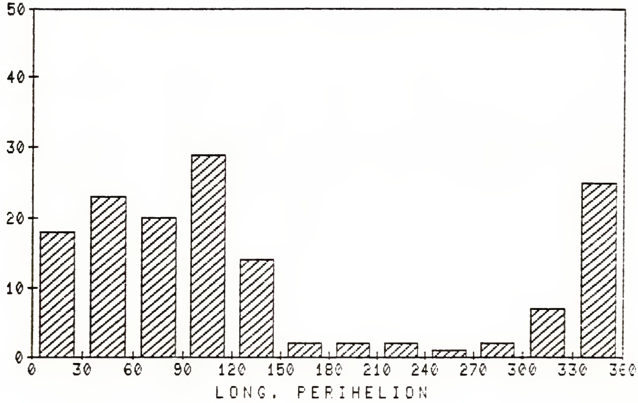

Figure 117. Number density vs. longitude of perihelion at 1.95 A.U.

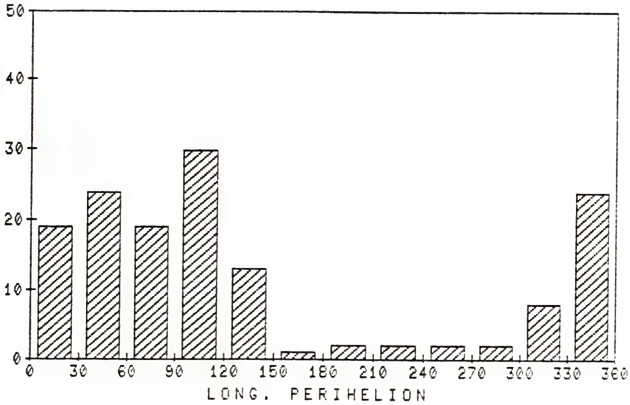

Figure 118. Number density vs. longitude of perihelion at 2.05 A.U.

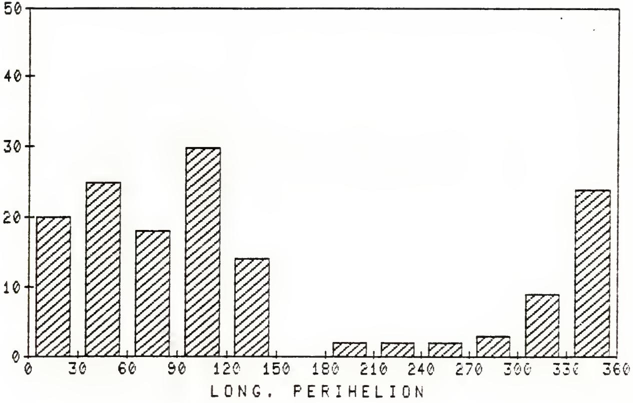

Figure 119. Number density vs. longitude of perihelion at 2.15 A.U.

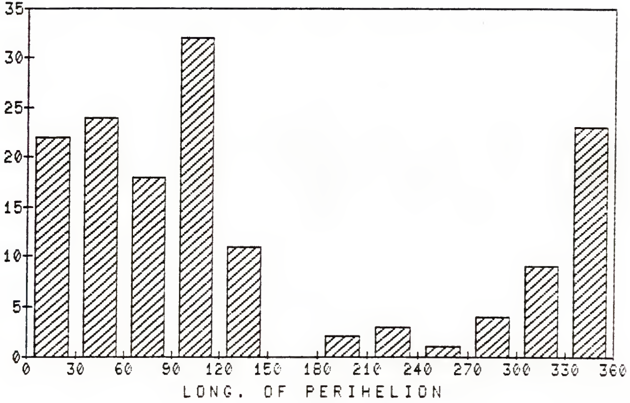

Figure 120. Number density vs. longitude of perihelion at 2.25 A.U.

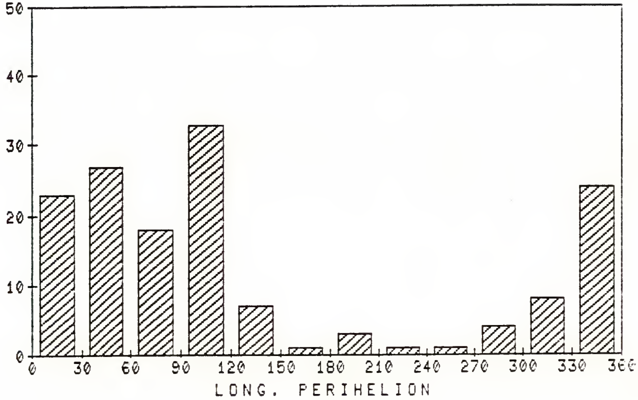

Figure 121. Number density vs. longitude of perihelion at 2.35 A.U.

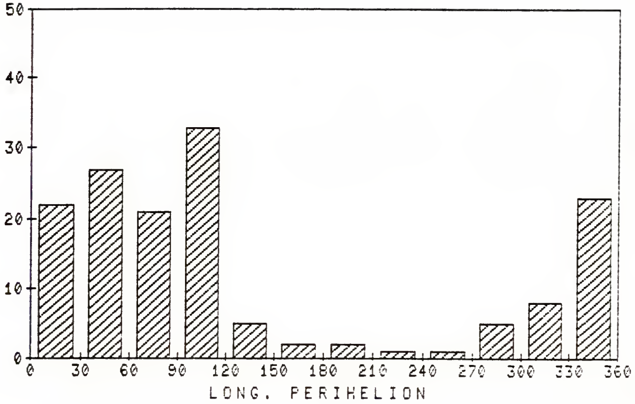

Figure 122. Number density vs. longitude of perihelion at 2.45 A.U.

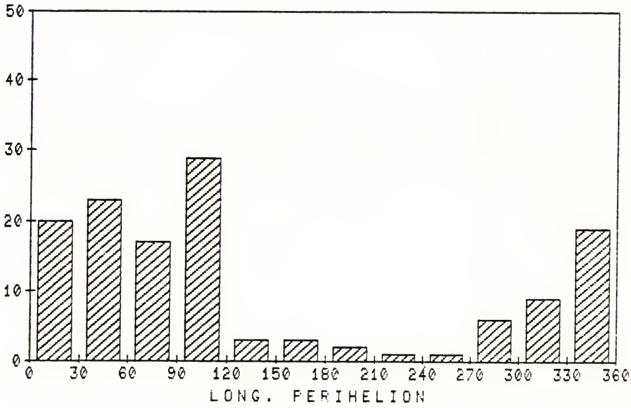

Figure 123. Number density vs. longitude of perihelion at 2.55 A.U.

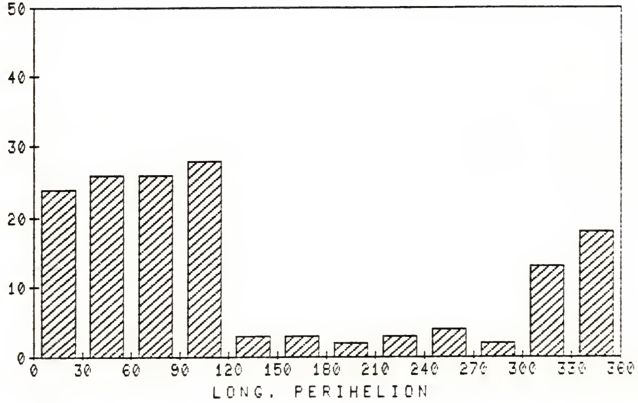

Figure 124. Number density vs. longitude of perihelion at 2.65 A.U.

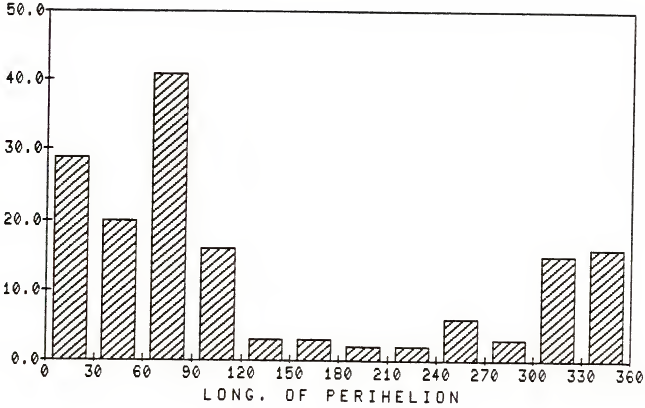

Figure 125. Number density vs. longitude of perihelion at 2.75 A.U.

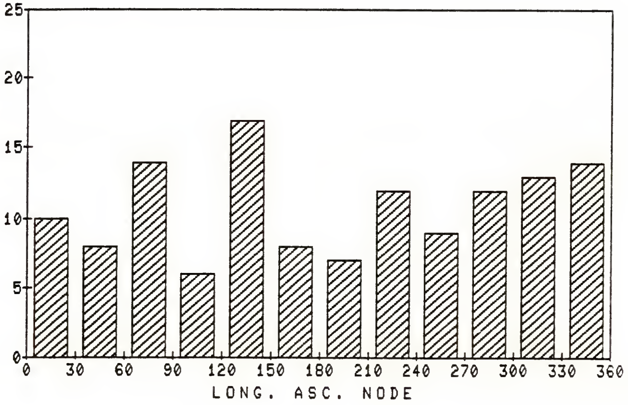

Figure 126. Number density vs. longitude of the ascending node at 0.35 A.U.

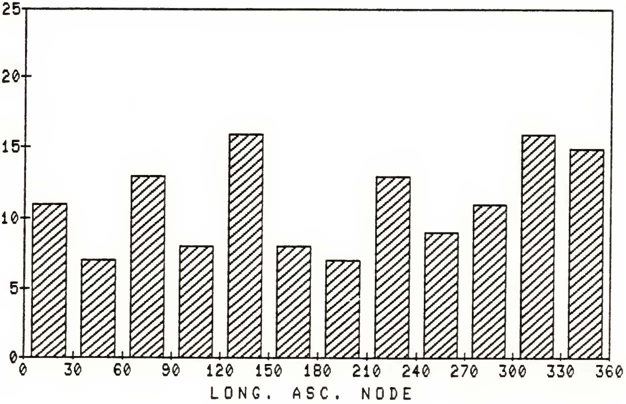

Figure 127. Number density vs. longitude of the ascending node at 0.45 A.U.

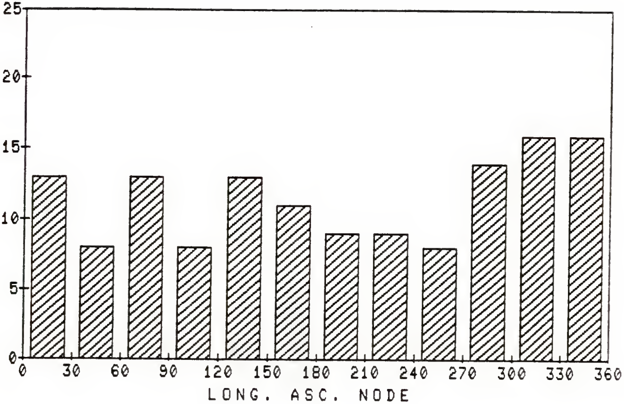

Figure 128. Number density vs. longitude of the ascending node at 0.55 A.U.

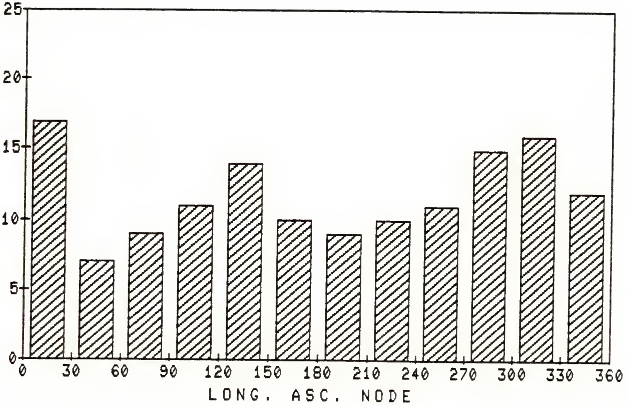

Figure 129. Number density vs. longitude of the ascending node at 0.65 A.U.

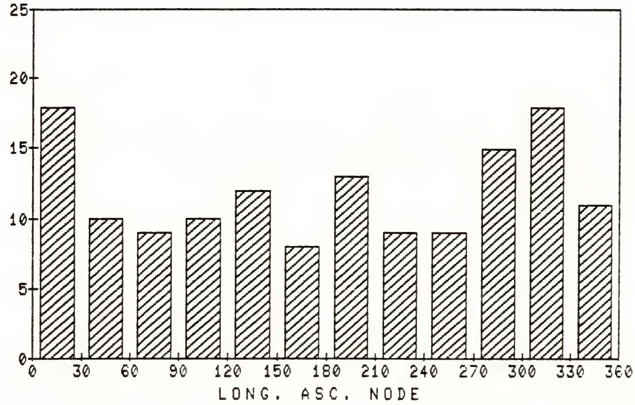

Figure 130. Number density vs. longitude of the ascending node at 0.75 A.U.

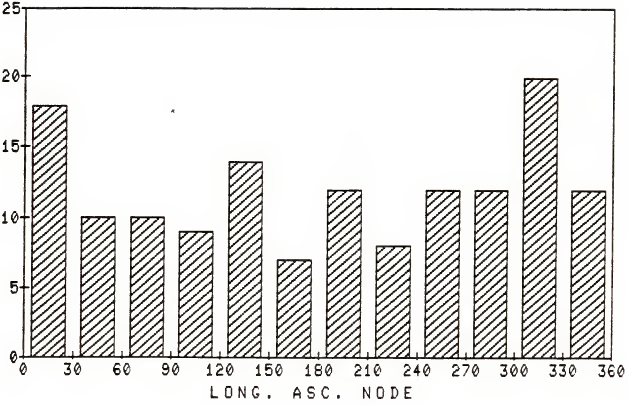

Figure 131. Number density vs. longitude of the ascending node at 0.85 A.U.

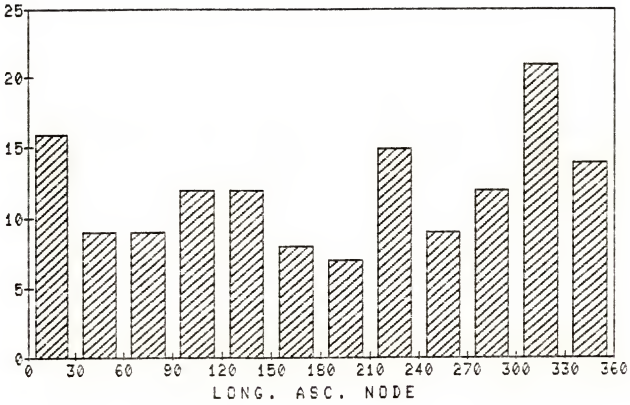

Figure 132. Number density vs. longitude of the ascending node at 0.95 A.U.

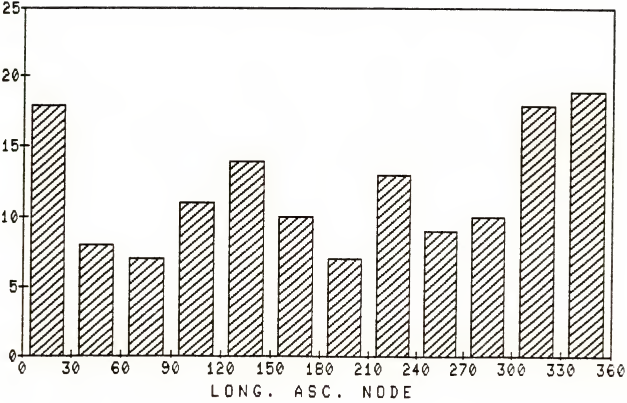

Figure 133. Number density vs. longitude of the ascending node at 1.05 A.U.

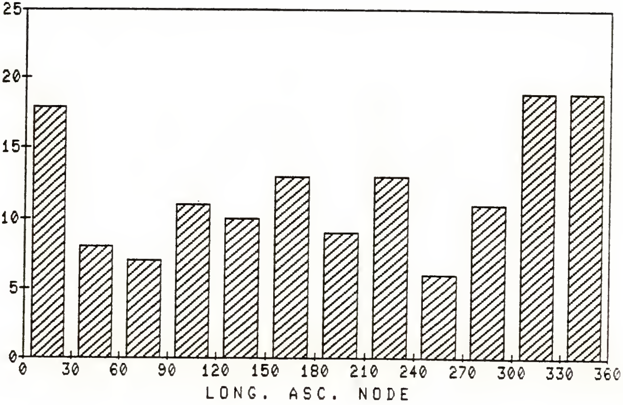

Figure 134. Number density vs. longitude of the ascending node at 1.15 A.U.

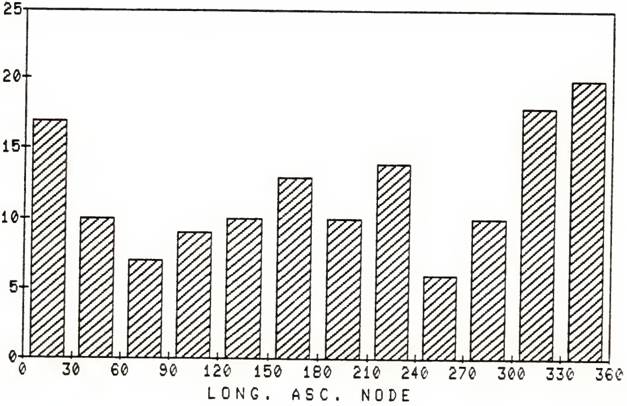

Figure 135. Number density vs. longitude of the ascending node at 1.25 A.U.

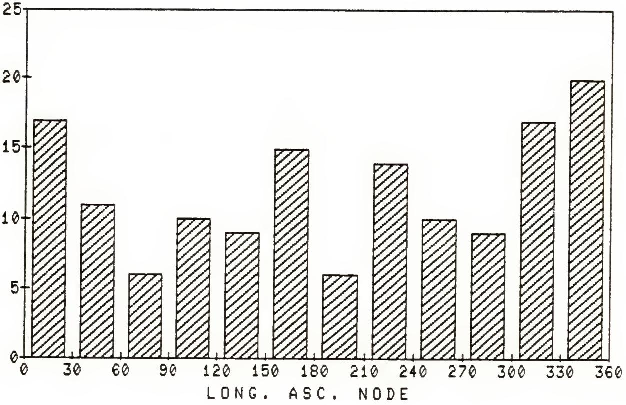

Figure 136. Number density vs. longitude of the ascending node at 1.35 A.U.

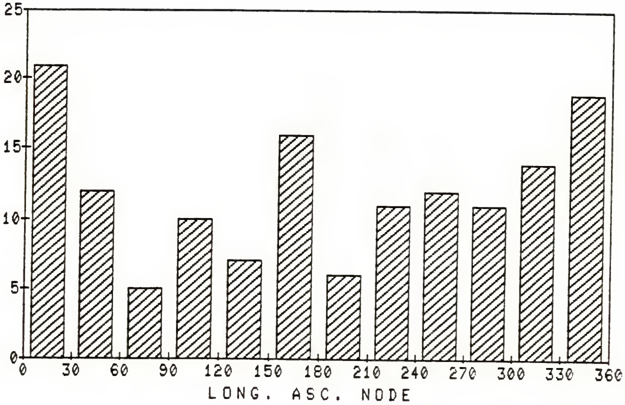

Figure 137. Number density vs. longitude of the ascending node at 1.45 A.U.

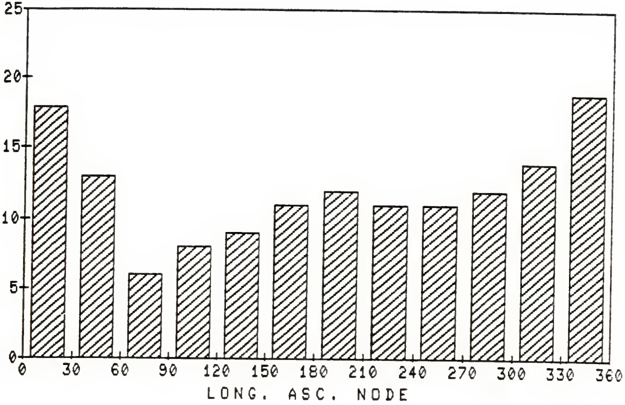

Figure 138. Number density vs. longitude of the ascending node at 1.55 A.U.

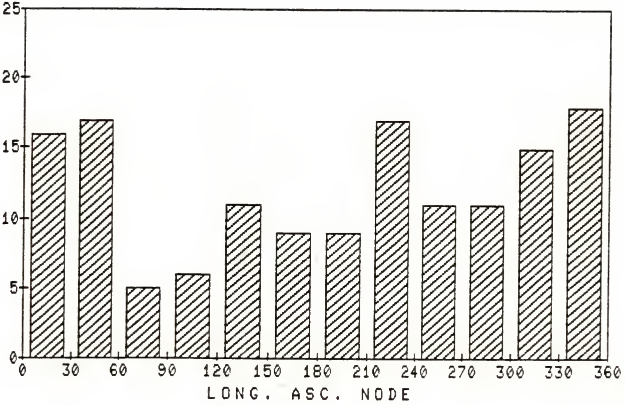

Figure 139. Number density vs. longitude of the ascending node at 1.65 A.U.

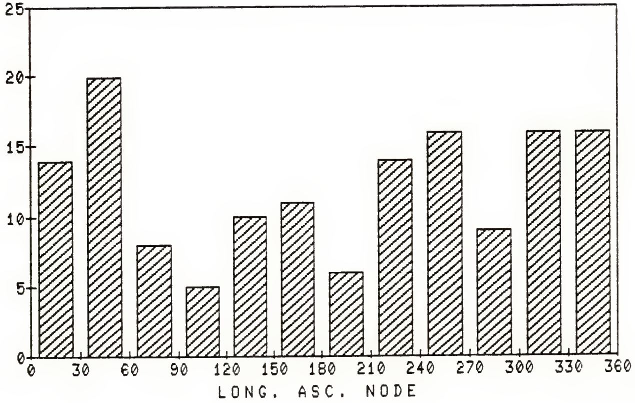

Figure 140. Number density vs. longitude of the ascending node at 1.75 A.U.

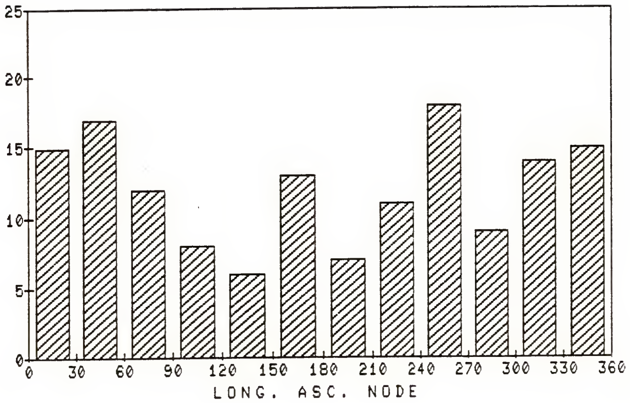

Figure 141. Number density vs. longitude of the ascending node at 1.85 A.U.

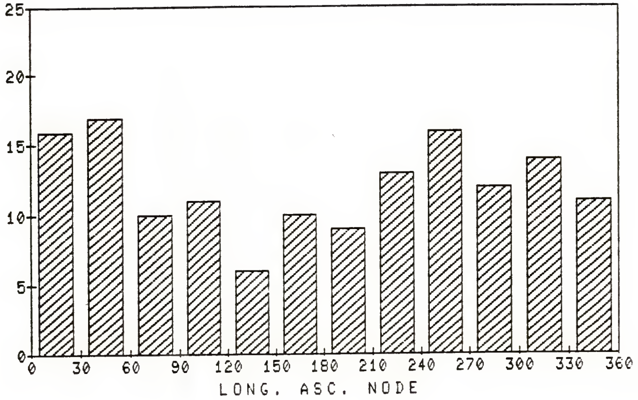

Figure 142. Number density vs. longitude of the ascending node at 1.95 A.U.

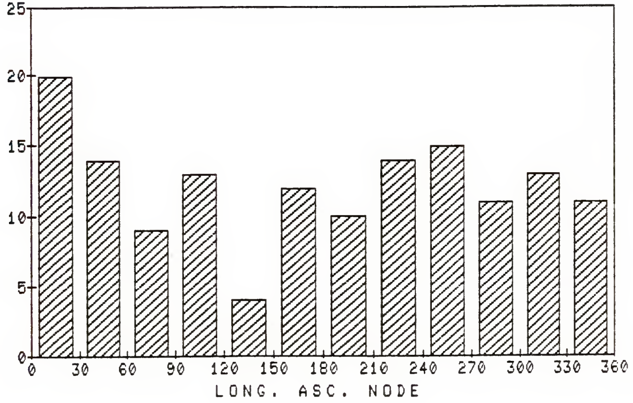

Figure 143. Number density vs. longitude of the ascending node at 2.05 A.U.

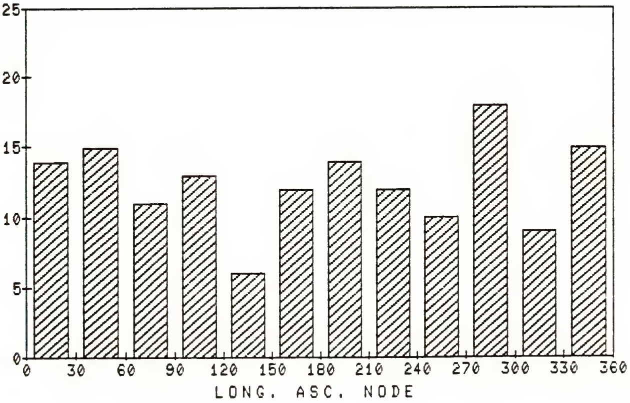

Figure 144. Number density vs. longitude of the ascending node at 2.15 A.U.

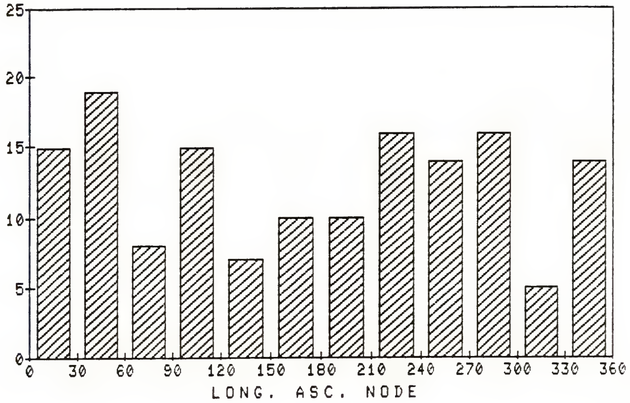

Figure 145. Number density vs. longitude of the ascending node at 2.25 A.U.

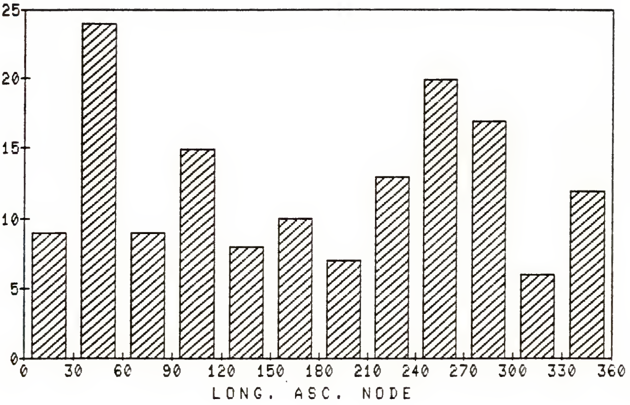

Figure 146. Number density vs. longitude of the ascending node at 2.35 A.U.

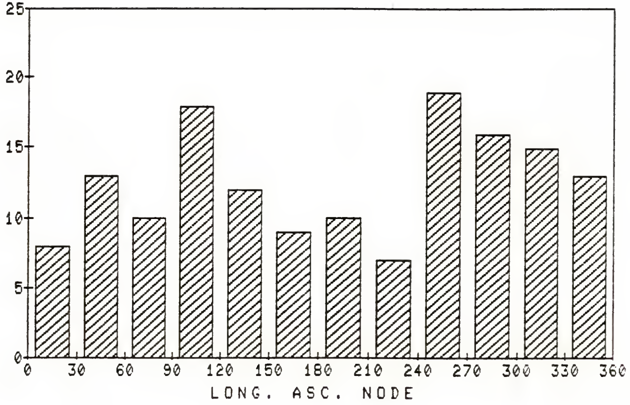

Figure 147. Number density vs. longitude of the ascending node at 2.45 A.U.

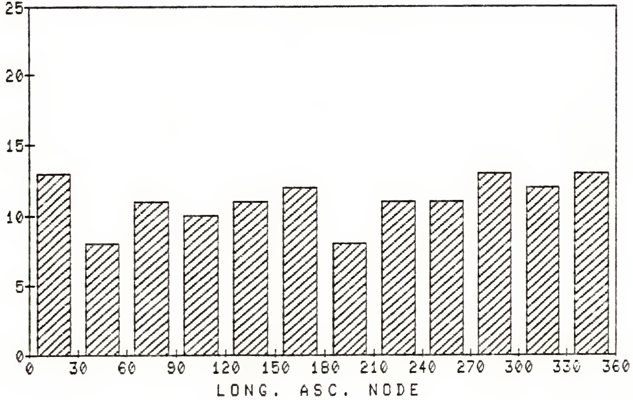

Figure 148. Number density vs. longitude of the ascending node at 2.55 A.U.

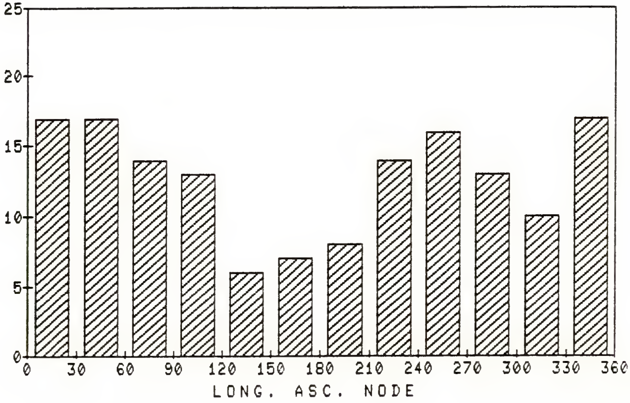

Figure 149. Number density vs. longitude of the ascending node at 2.65 A.U.

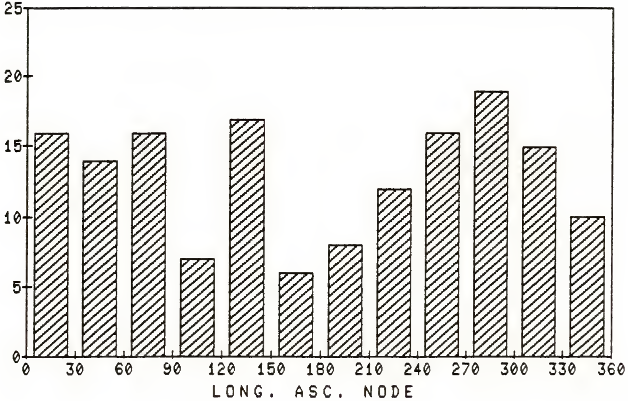

Figure 150. Number density vs. longitude of the ascending node at 2.75 A.U.

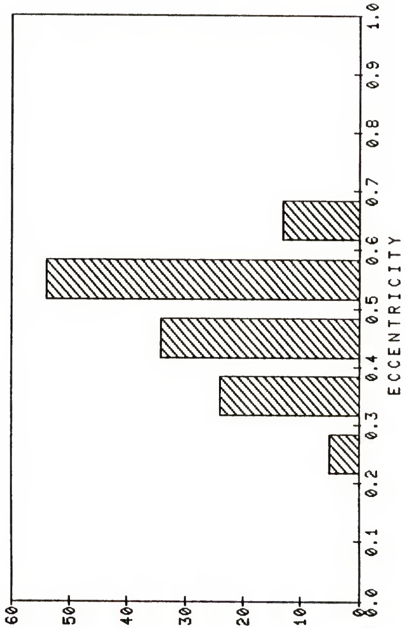

Figure 151. Number density vs. eccentricity at 0.35 A.U.

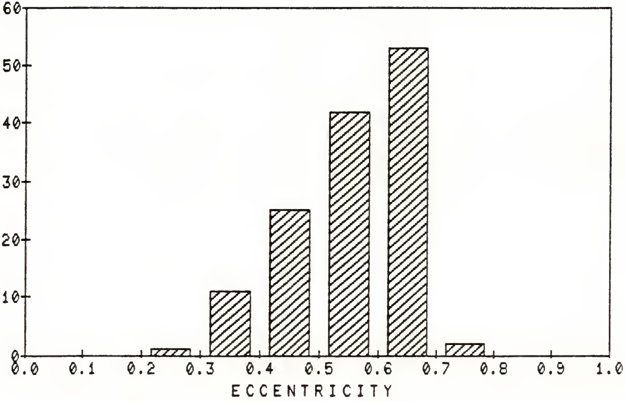

Figure 152. Number density vs. eccentricity at 0.45 A.U.

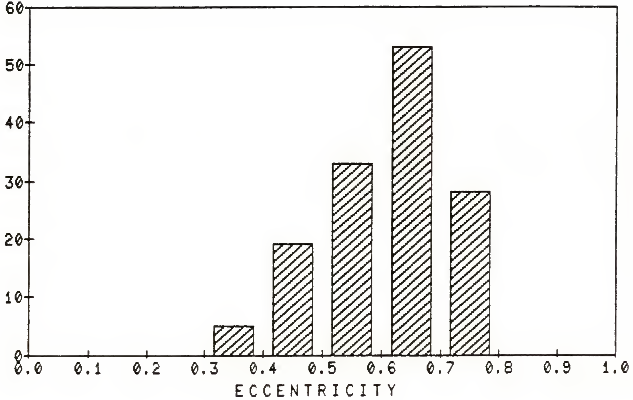

Figure 153. Number density vs. eccentricity at 0.55 A.U.

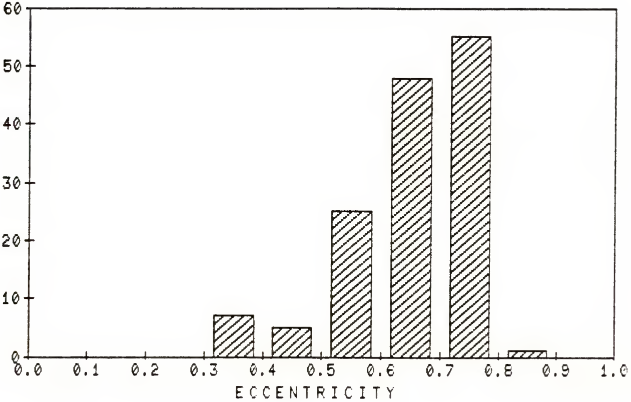

Figure 154. Number density vs. eccentricity at 0.65 A.U.

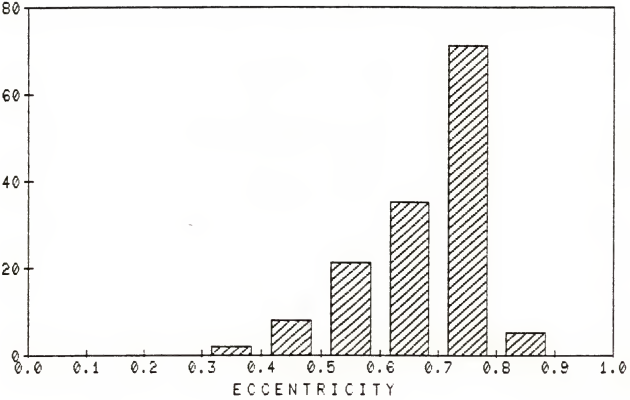

Figure 155. Number density vs. eccentricity at 0.75 A.U.

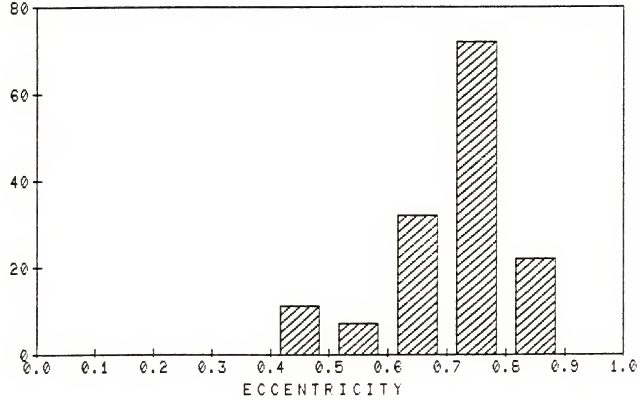

Figure 156. Number density vs. eccentricity at 0.85 A.U.

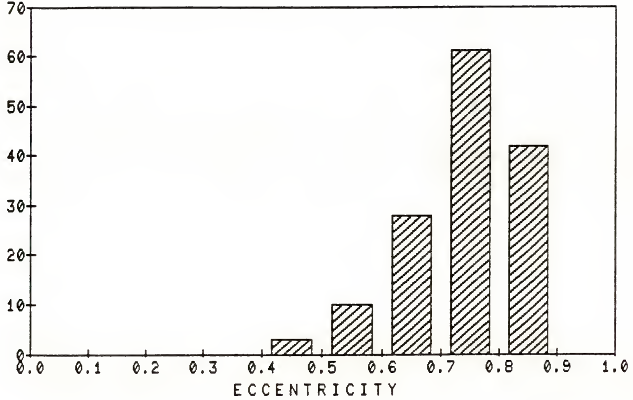

Figure 157. Number density vs. eccentricity at 0.95 A.U.

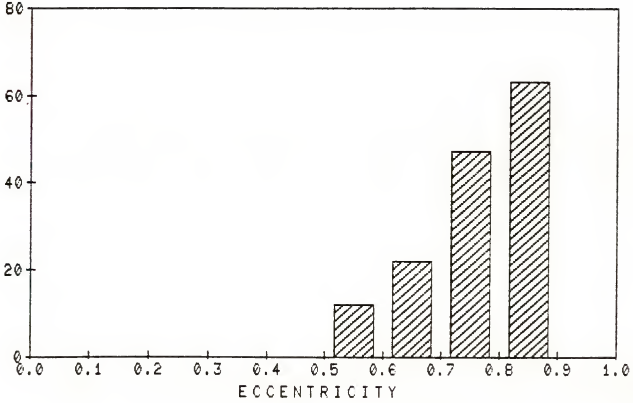

Figure 158. Number density vs. eccentricity at 1.05 A.U.

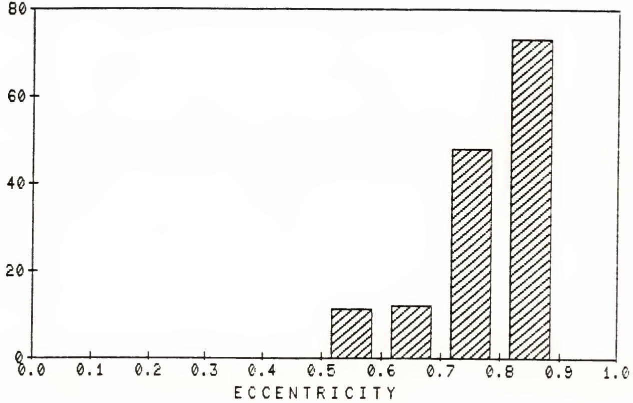

Figure 159. Number density vs. eccentricity at 1.15 A.U.

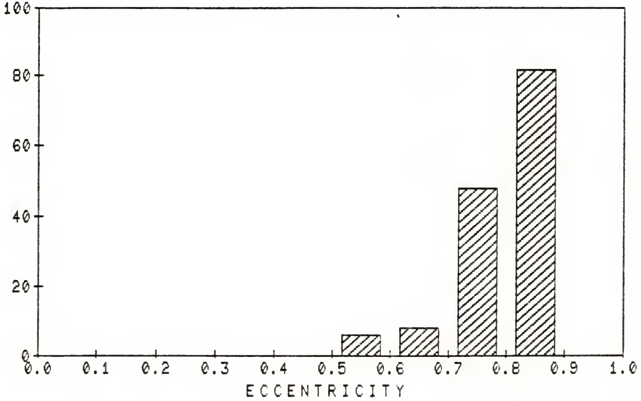

Figure 160. Number density vs. eccentricity at 1.25 A.U.

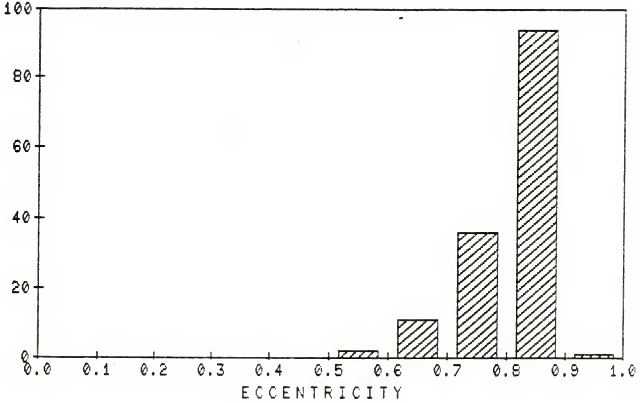

Figure 161. Number density vs. eccentricity at 1.35 A.U.

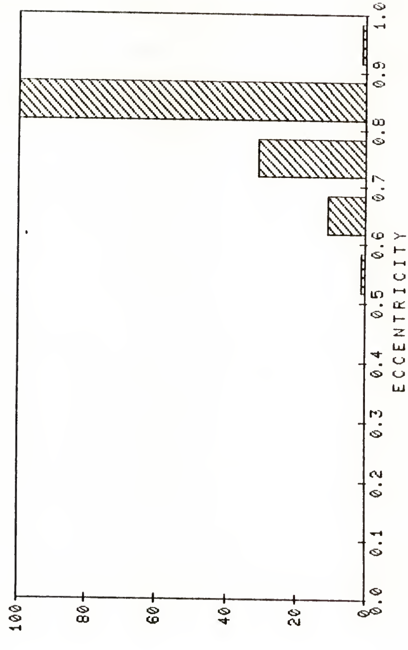

Figure 162. Number density vs. eccentricity at 1.45 A.U.

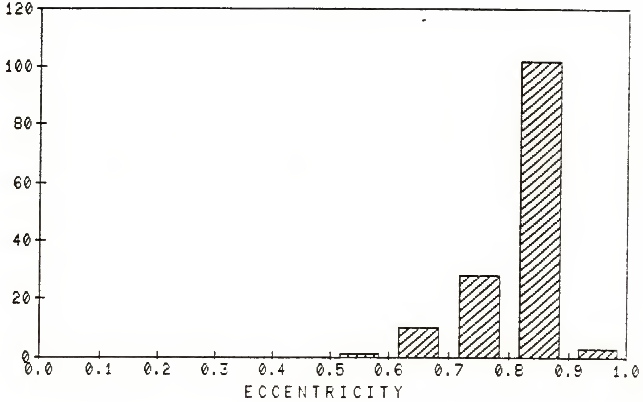

Figure 163. Number density vs. eccentricity at 1.55 A.U.

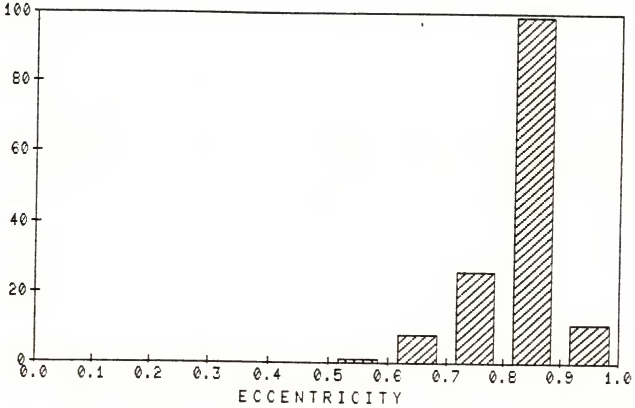

Figure 164. Number density vs. eccentricity at 1.65 A.U.

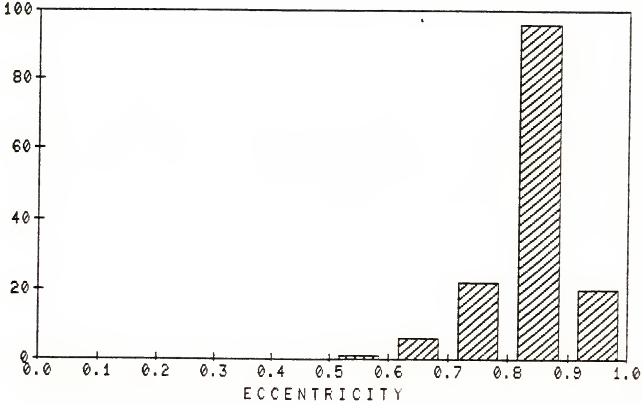

Figure 165. Number density vs. eccentricity at 1.75 A.U.

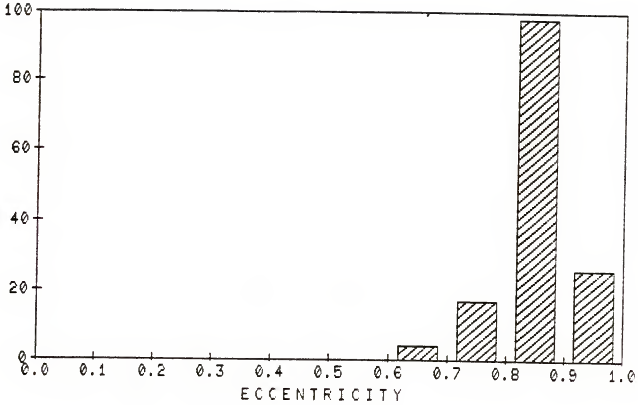

Figure 166. Number density vs. eccentricity at 1.85 A.U.

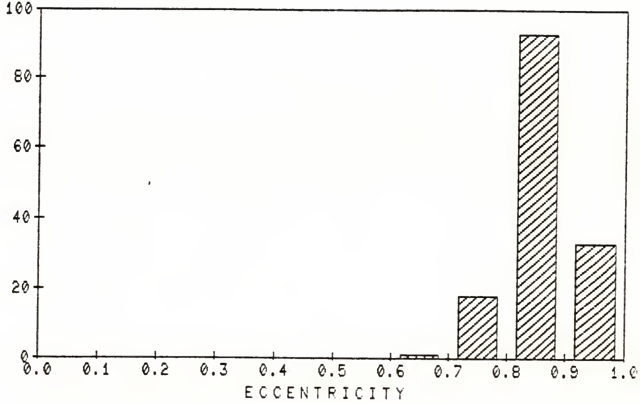

Figure 167. Number density vs. eccentricity at 1.95 A.U.

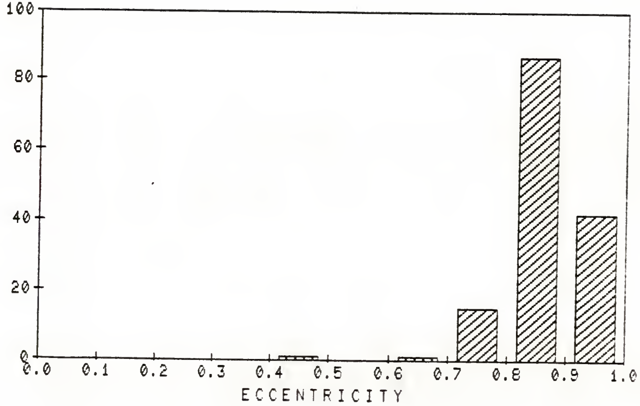

Figure 168. Number density vs. eccentricity at 2.05 A.U.

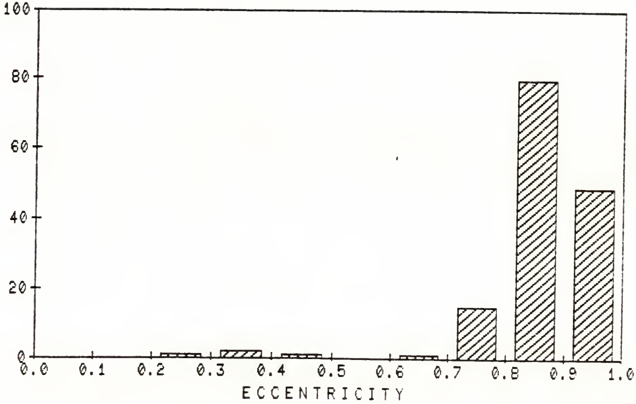

Figure 169. Number density vs. eccentricity at 2.15 A.U.

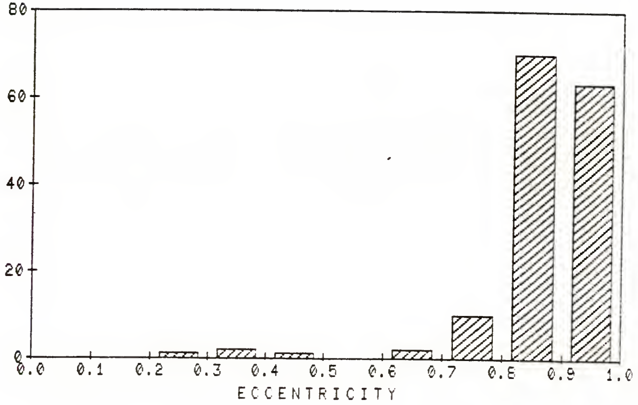

Figure 170. Number density vs. eccentricity at 2.25 A.U.

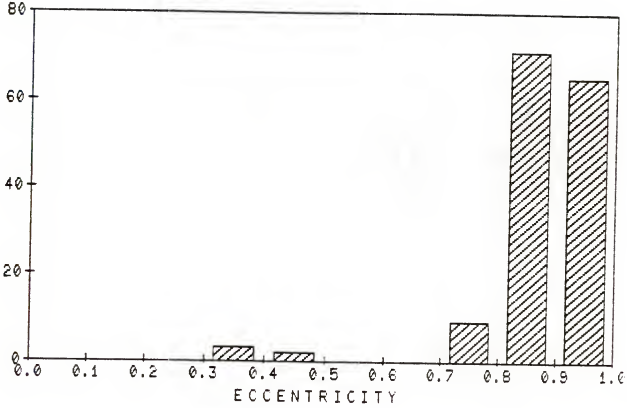

Figure 171. Number density vs. eccentricity at 2.35 A.U.

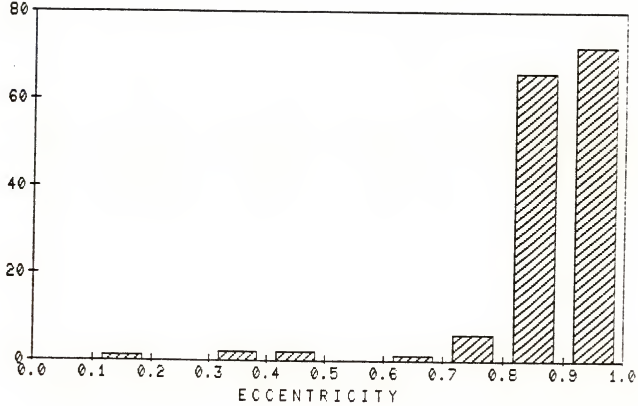

Figure 172. Number density vs. eccentricity at 2.45 A.U.

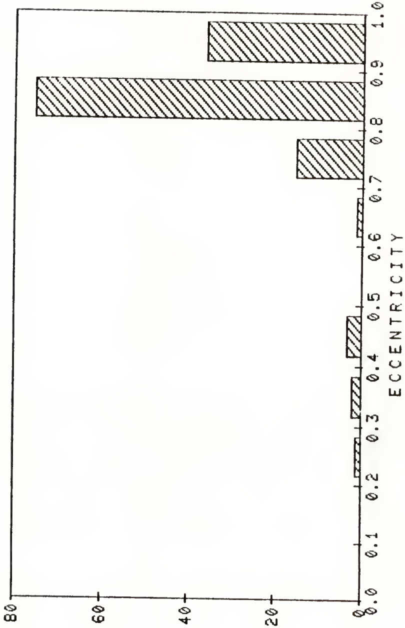

Figure 173. Number density vs. eccentricity at 2.55 A.U.

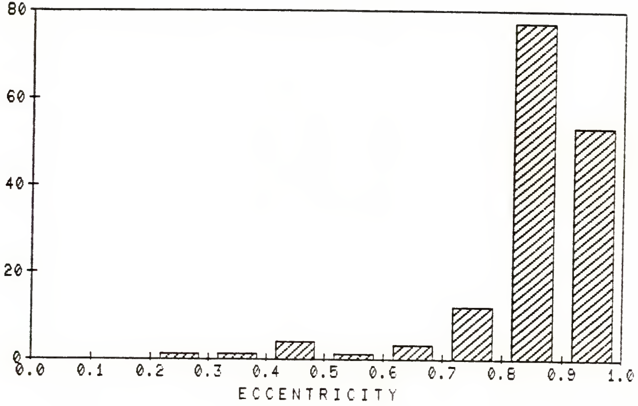

Figure 174. Number density vs. eccentricity at 2.65 A.U.

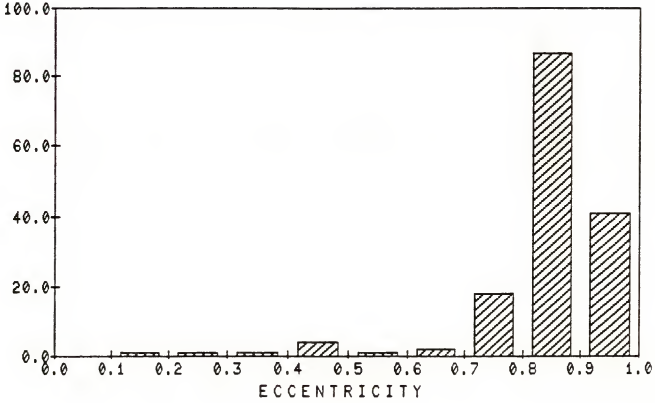

Figure 175. Number density vs. eccentricity at 2.75 A.U.

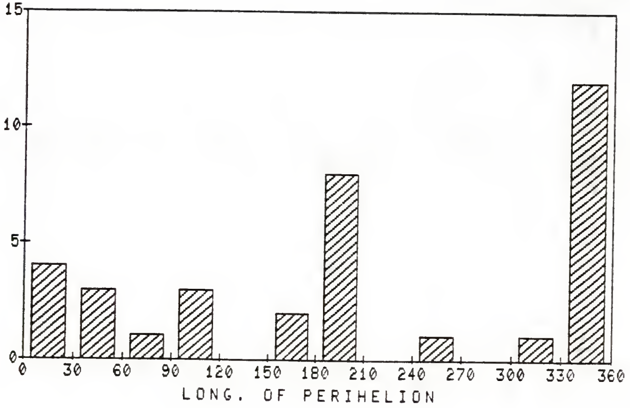

Figure 176. Number density vs. longitude of perihelion, 23,500 years ago.

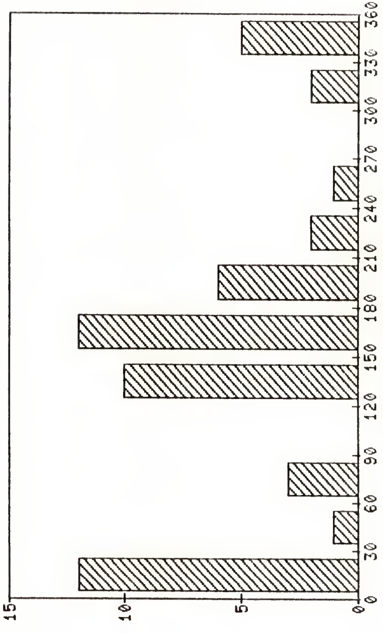

Figure 177. Number density vs. longitude of perihelion, 22,000 years ago.

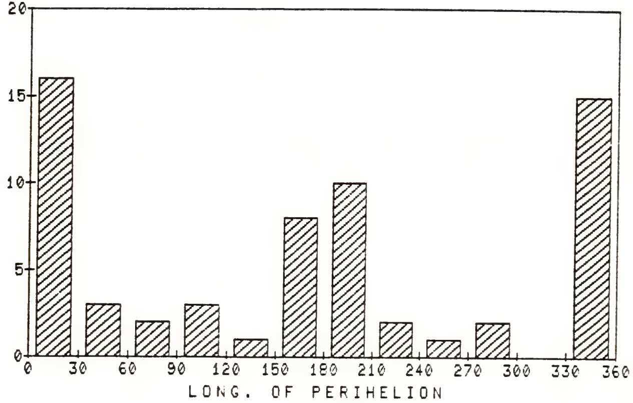

Figure 178. Number density vs. longitude of perihelion, 20,500 years ago.

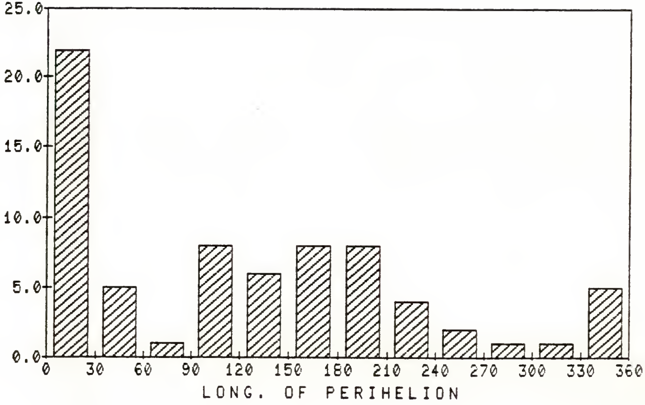

Figure 179. Number density vs. longitude of perihelion, 19,000 years ago.

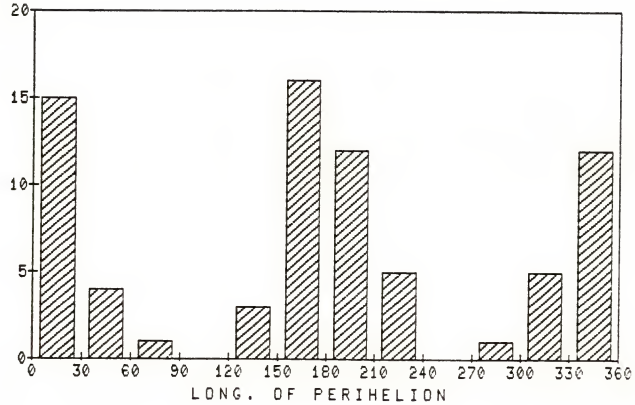

Figure 180. Number density vs. longitude of perihelion, 17,500 years ago.

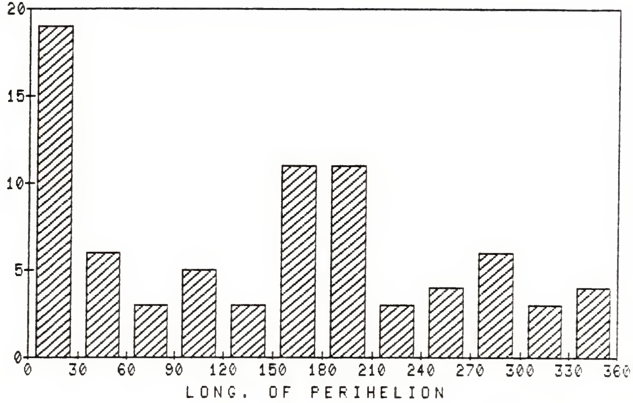

Figure 181. Number density vs. longitude of perihelion, 16,000 years ago.

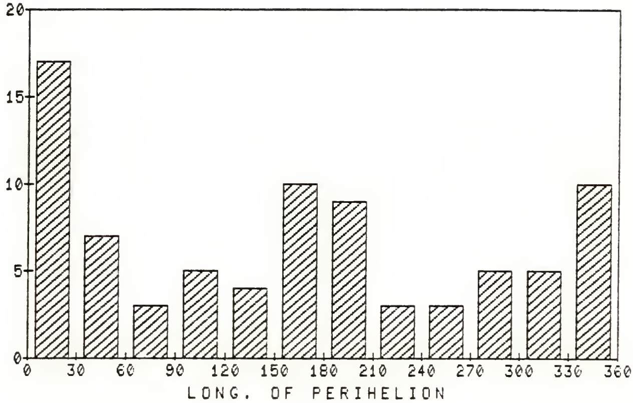

Figure 182. Number density vs. longitude of perihelion, 14,500 years ago.

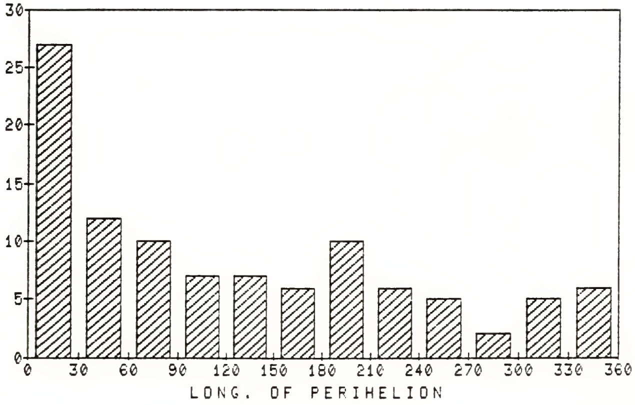

Figure 183. Number density vs. longitude of perihelion, 13,000 years ago.

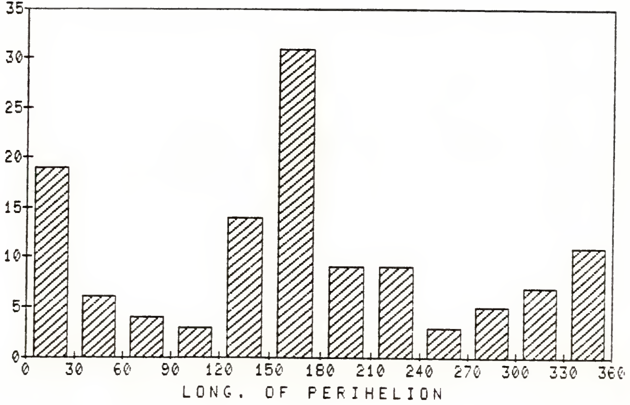

Figure 184. Number density vs. longitude of perihelion, 11,500 years ago.

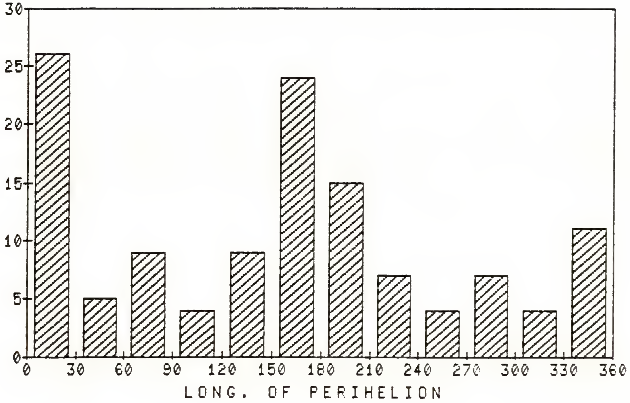

Figure 185. Number density vs. longitude of perihelion, 10,000 years ago.

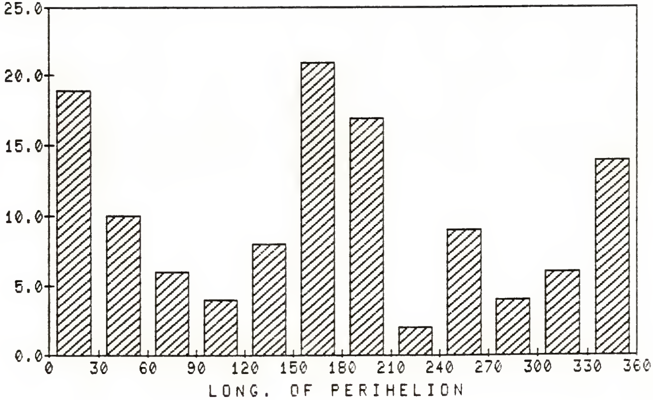

Figure 186. Number density vs. longitude of perihelion, 8,500 years ago.

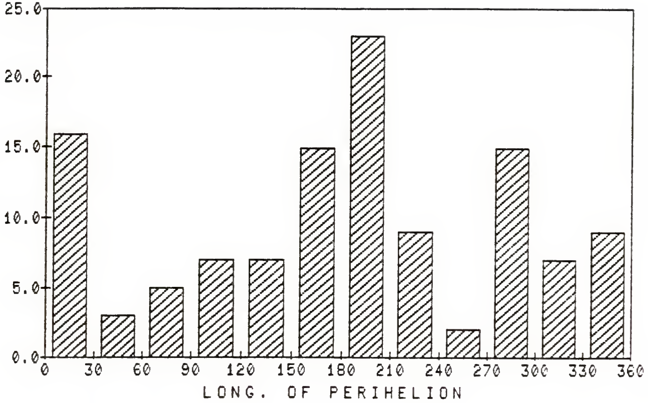

Figure 187. Number density vs. longitude of perihelion, 7,000 years ago.

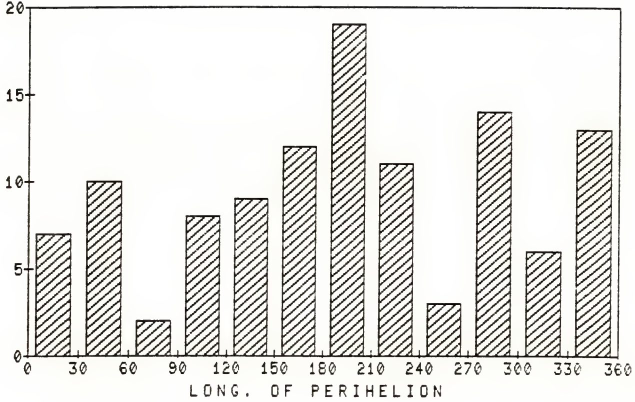

Figure 188. Number density vs. longitude of perihelion, 5,500 years ago.

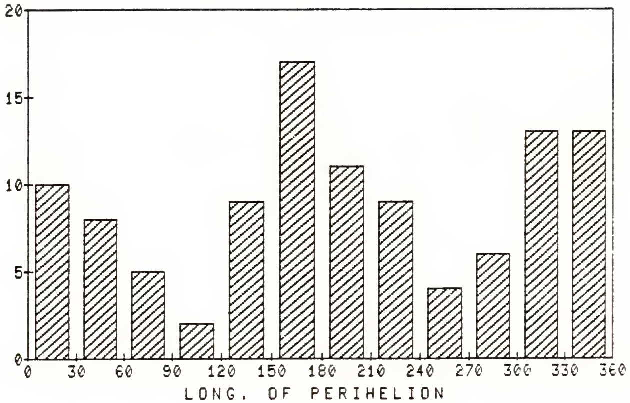

Figure 189. Number density vs. longitude of perihelion, 4,000 years ago.

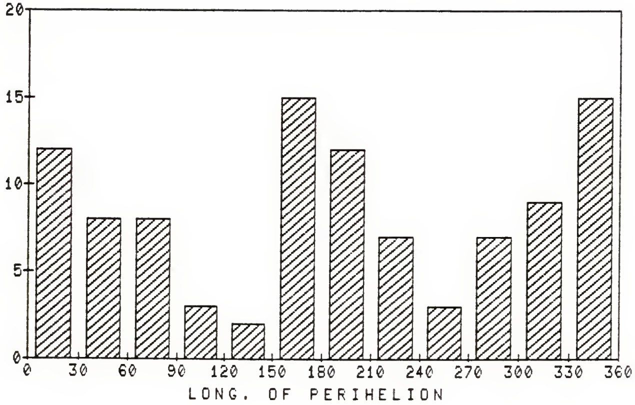

Figure 190. Number density vs. longitude of perihelion, 2,500 years ago.

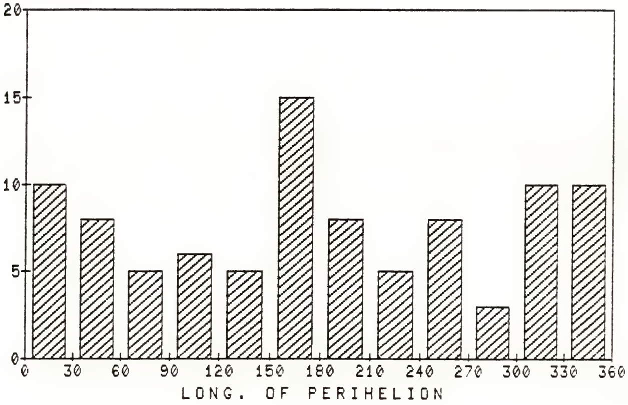

Figure 191. Number density vs. longitude of perihelion, 1,000 years ago.

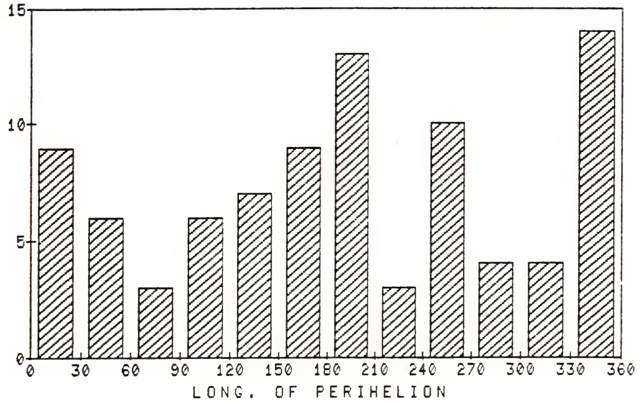

Figure 192. Number density vs. longitude of perihelion, 500 years from now.

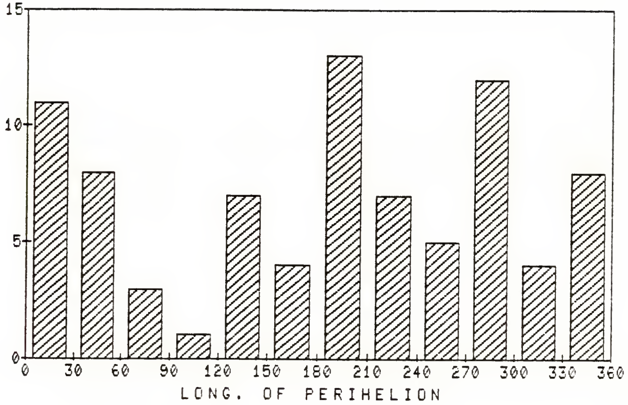

Figure 193. Number density vs. longitude of perihelion, 2,000 years from now.

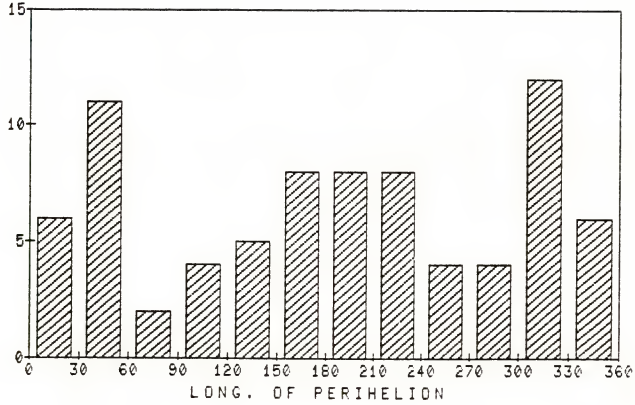

Figure 194. Number density vs. longitude of perihelion, 3,500 years from now.

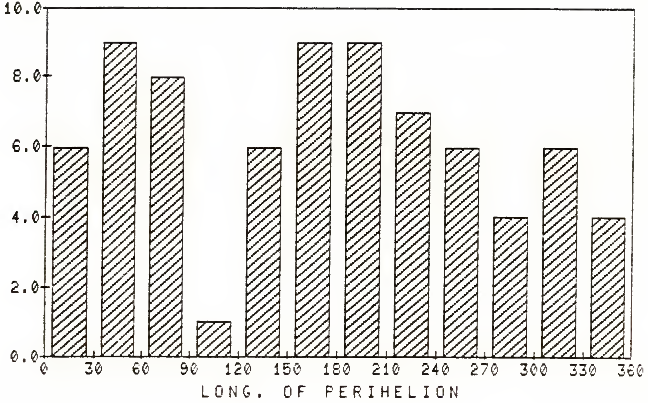

Figure 195. Number density vs. longitude of perihelion, 5,000 years from now.

BIOGRAPHICAL SKETCH

Edwin T. Rusk was born on the 25th of August 1950, in Baltimore, Maryland, the only child of Edwin V. and Ethel E. Rusk.

After four years of undergraduate study in astronomy at Case Institute of Technology, he received his Bachelor of Science in astronomy in 1972. He worked for a chemical manufacturing firm before entering graduate school at the University of Florida.

Initially he intended to study cosmology under the direction of G.C. Omer. Toward this end, he became acquainted with the general theory of relativity and the mathematics of tensor calculus.

In 1979 he took a one-year teaching position as an Assistant Professor at the University of Southern Mississippi. There he taught Introductory Astronomy, Mechanics, and several laboratory courses.

After an additional year off, he returned to the University of Florida in 1981. In August of 1983 he was strongly encouraged to enter the field of interplanetary dust and zodiacal light by Dr. N.Y. Misconi.

On July 5th, 1985, he married the former Miss Nancy L. McElrath. They are presently residing in Gainesville, Florida.

I certify that I have read this study and that in my opinion it conforms to acceptable standards of scholarly presentation and is fully adequate, in scope and quality, as a dissertation for the degree of Doctor of Philosophy.

Nebil Y. Misconi

N.Y. Misconi, Chairman
Associate Research Scientist of Astronomy

I certify that I have read this study and that in my opinion it conforms to acceptable standards of scholarly presentation and is fully adequate, in scope and quality, as a dissertation for the degree of Doctor of Philosophy.

J. H. Hunter

J.H. Hunter
Professor of Astronomy

I certify that I have read this study and that in my opinion it conforms to acceptable standards of scholarly presentation and is fully adequate, in scope and quality, as a dissertation for the degree of Doctor of Philosophy.

Alex G. Smith

A.G. Smith
Distinguished Service Professor of Astronomy

I certify that I have read this study and that in my opinion it conforms to acceptable standards of scholarly presentation and is fully adequate, in scope and quality, as a dissertation for the degree of Doctor of Philosophy.

Haywood C. Smith Jr.

H.C. Smith
Associate Professor of Astronomy

I certify that I have read this study and that in my opinion it conforms to acceptable standards of scholarly presentation and is fully adequate, in scope and quality, as a dissertation for the degree of Doctor of Philosophy.

C.A. Williams
Associate Professor of Astronomy

I certify that I have read this study and that in my opinion it conforms to acceptable standards of scholarly presentation and is fully adequate, in scope and quality, as a dissertation for the degree of Doctor of Philosophy.

Bo Gustaf

B.Å.S. Gustafson
Assistant Research Scientist, Astronomy

I certify that I have read this study and that in my opinion it conforms to acceptable standards of scholarly presentation and is fully adequate, in scope and quality, as a dissertation for the degree of Doctor of Philosophy.

J. E. Keesling

J.E. Keesling
Professor of Mathematics

This dissertation was submitted to the Graduate Faculty of the Department of Astronomy in the College of Liberal Arts and Sciences and to the Graduate School and was accepted as partial fulfillment of the requirements for the degree of Doctor of Philosophy.

May 1986

Dean, Graduate School